Femtosecond relaxation dynamics in collective-electronic-state materials: cuprate and iron-pnictide superconductors and charge-density wave systems

Ljupka Stojčevska

Doctoral Dissertation
Jožef Stefan International Postgraduate School
Ljubljana, Slovenia, June 2013

Evaluation Board:

Prof. Dr. Denis Arčon, Chairman, Jožef Stefan Institute, Jamova cesta 39, Ljubljana Slovenia

Asst. Prof. Christoph Gadermaier, Member, Jožef Stefan Institute, Jamova cesta 39, Ljubljana, Slovenia

Prof. Dr. Uwe Bovensiepen, Member, Universität Duisburg-Essen, Lothrarst.1, Duisburg, Germany

MEDNARODNA PODIPLOMSKA ŠOLA JOŽEFA STEFANA
JOŽEF STEFAN INTERNATIONAL POSTGRADUATE SCHOOL



Ljupka Stojčevska

Femtosecond relaxation dynamics in collective-electronic-state materials: cuprate and iron-pnictide superconductors and charge-density wave systems

Doctoral Dissertation

Femtosekundna relaksacijska dinamika v snoveh s kolektivnimi elektronskimi stanji: kupratni in železo-pniktidni superprevodniki ter sistemi z valom gostote naboja

Doktorska disertacija

Supervisor: Asst. Prof. Tomaž Mertelj

Co-Supervisor: Prof. Dr. Dragan D. Mihailović

Ljubljana, Slovenia, June 2013

Посветено на моите родители
Devoted to my parents

Index

Abstract **IX**

Povzetek **X**

Abbreviations **XI**

1 Introduction **1**
1.1 Cuprate superconductors . . . 3
1.2 Iron-based superconductors . . . 4
1.3 Charge-density wave systems . . . 6
1.4 Physics of charge- and spin-density wave systems . . . 8
1.5 Dynamics of broken symmetry states . . . 9
1.5.1 Fundamentals of the Ginzburg-Landau and Bardeen-Cooper-Schrieffer theory . . . 9
1.6 Kinetics in the superconducting state . . . 13
1.6.1 Photoexcitation, initial carrier relaxation and probe process . . . 15
1.7 Kinetics in the metallic state . . . 17
1.8 Introducing the term of condensation energy . . . 19
1.9 Experimental measurement of the superconducting destruction energy . . . 20
1.10 Heating effects . . . 21

2 Experimental **23**
2.1 Sample preparation and characterization . . . 23
2.1.1 $YBa_2Cu_3O_{7-\delta}$ superconductor . . . 23
2.1.2 $SmFeAsO_{1-x}F_x$, $SrFe_2As_2$ and $Ba(Fe,Co)_2As_2$ iron-pnictides . . . 24
2.1.3 $1T$-TaS_2 charge-density wave system . . . 25
2.2 Femtosecond optical spectroscopy . . . 26
2.2.1 The pump-probe technique . . . 28
2.3 Beam size determination . . . 30

3 Study of the femtosecond relaxation dynamics in iron-based pnictides **31**
3.1 Femtosecond spectroscopy in $SmFeAsO_{1-x}F_x$ iron-pnictide superconductor . . . 31
3.1.1 The undoped Sm-1111 sample . . . 32
3.1.1.1 Gap in the SDW state . . . 35
3.1.1.2 Relaxation dynamics at the room temperature . . . 35
3.1.2 The superconducting Sm-1111 sample . . . 35
3.1.2.1 Decomposition of the $\Delta R/R$ transients in superconducting $SmFeAsO_{0.8}F_{0.2}$ into components . . . 36

3.1.2.2 Experimental determination of the superconducting destruction energy . . . 40
3.1.2.3 Response in the normal state . . . 41
3.2 Femtosecond spectroscopy in X-122 (X=Sr,Ba) iron-based pnictides . . . 43
3.2.1 Temperature dependence of $\Delta R/R$ transients in undoped $SrFe_2As_2$ single crystals . . . 43
3.2.2 Fluence dependence of $\Delta R/R$ transients in undoped $SrFe_2As_2$ single crystals . . . 45
3.2.3 Relaxation dynamics in underdoped $Ba(Fe_{1-x}Co_x)_2As_2$ single crystals 47
3.2.3.1 Determination of the gap in the SDW state . . . 51
3.2.4 Response in the superconducting $Ba(Fe_{1-x}Co_x)_2As_2$ samples . . . 53
3.2.4.1 Temperature dependence and comparison with SmFeAs(O,F) 55
3.2.5 Normal state . . . 56
3.2.5.1 Anisotropy . . . 58
3.2.5.2 Determination of the electron-phonon coupling constant . . . 59
3.3 Summary and conclusions . . . 61

4 Nonthermal destruction of the superconducting state 63
4.1 Previous studies and motivation . . . 63
4.2 Fluence dependence of $\Delta R/R$ transients in $YBa_2Cu_3O_{7-\delta}$ . . . 64
4.3 Comparison of the optically measured SC destruction energy by femtosecond laser spectroscopy and condensation energy determined by specific heat measurements in high-T_c superconductors . . . 67
4.3.1 Summary and conclussions . . . 69

5 Bistable switching to a new hidden state of matter by femtosecond laser pulse in 1T-TaS_2 dichalcogenide 71
5.1 Write-pump-probe technique . . . 71
5.2 Observation of a new state in 1T-TaS_2 . . . 73
5.3 Theoretical consideration for p-TaS_2 state formation . . . 81
5.4 Possible application as ultrafast memory elements . . . 84
5.5 Summary and conclusions . . . 84

6 Conclusions 85

7 Acknowledgements 87

8 References 89

Index of Figures 99

Index of Tables 103

Appendix 105
A Appendix 1 . . . 105
A.1 Original Scientific Articles . . . 105
A.2 Published Scientific Conference Contributions (Invited lecture) . . . 105
A.3 Published Scientific Conference Contributions . . . 106
A.4 Monographs . . . 108
A.4.1 Patent application . . . 108
B Appendix 2 . . . 109
B.1 Destruction of the superconducting state in $YBa_2Cu_3O_{7-\delta}$ superconductor . . . 109
B.2 Switching to a new hidden state in 1T-TaS_2 . . . 112

C Appendix 3 114
C.1 Maxwell's equations in a vacuum 114
C.2 Maxwell's equations in the presence of matter 114

Abstract

This thesis covers a study of the photoexcited relaxation dynamics in superconducting iron-based pnictides, cuprates and charge-density wave systems by means of femtosecond laser spectroscopy. To examine the temperature and fluence dependence of photoinduced reflectivity transients $\Delta R/R$ in iron-based pnictides and cuprates, we apply a standard double pump-probe technique, while for the charge-density wave systems, we introduce a new write-pump-probe pulse technique.

Temperature dependence study of $\Delta R/R$ in a low-perturbation pump regime in undoped iron-based pnictides has revealed a critical slowing down of the relaxation at spin-density wave/structural transition temperature $T_{\mathrm{SDW}}/T_{\mathrm{s}}$. At temperatures below $T_{\mathrm{SDW}}/T_{\mathrm{s}}$, a bottleneck appears in the single particle relaxation dynamics, associated with opening of a BCS-like temperature dependent gap. We estimate the magnitude of the gap and find that it decreases with increasing doping which is in accordance with a stability decrease of the orthorombic/SDW state. From the relaxation time in the normal state, we determined the electron phonon coupling constant $\lambda \approx 0.2$ from the second moment of the Eliashberg function. In all three studied iron-based pnictides, λ has a similar values referring to a moderate electron phonon coupling.

In the superconducting pnictides and cuprates, we observe a saturation of the SC component with increasing pump fluence. From the threshold pump fluence, we estimate the SC state destruction energy density U_d and find that it exhibits an approximate square power-law dependence on T_{c}. This systematic behavior is discussed in the framework of a model based on phonon-mediated quasiparticle bottleneck mechanism.

The T-dependence of the transient reflectivity amplitude in the normal state is consistent with the presence of a temperature-independent gap (pseudogap) in the QP density of states. Estimated magnitudes of the pseudogap decrease with increasing doping and they are consistent with the pseudogap values obtained from the T-dependence of the Knight shift.

In Co-doped Ba-122 samples, we observe in nominally tetragonal phase a twofold rotational anisotropy with respect to the probe polarization up to ~ 200 K. The anisotropy is assigned to electronic nematic fluctuations or ordering of the Fe d orbitals.

We introduce a new write-pump-probe technique to study the symmetry breaking transition in $1T$-TaS_2 single crystals. In these experiments, we quench the system with a single intense 50 fs pulse into a high symmetry state and then monitor the temporal recovery with a standard pump-probe sequence. A switching to a new hidden photoinduced p-TaS_2 state (ON state) was achieved after certain quench pulse threshold energy. It was shown that a new state can be reached only via optical path and it is stable up to ~ 100 K. To return back the system from the p-TaS_2 state to the CCDW state (OFF state), we apply a train of long 50 ps pulses. The switching ON/OFF is repeatable and accompanied with a change in reflectivity and DC resistance, opening a new possibility for ultrafast non-volatile memory devices.

Povzetek

Doktorsko delo obravnava fotovzbujeno relaksacijsko dinamiko v superprevodnih železovih pniktidih, kupratih in sistemih z valom gostote naboja s femtosekundno lasersko spektroskopijo. Za raziskovanje temperaturne in fluenčne odvisnosti fotovzbujenih tranzientnih reflektivnosti $\Delta R/R$ v železovih pniktidih in kupratih smo uporabili standardno dvojno črpalno-testno tehniko. Za sisteme vala gostote naboja pa vpeljujemo novo vpisovalno-črpalno-testno sunkovno tehniko.

Študije temperaturne odvisnosti $\Delta R/R$ v nizko perturbacijskem vzbujevalnem režimu v nedopiranih železovih pniktidih so pokazale kritično upočasnjevanje relaksacije pri tranzicijski temperaturi sistema vala gostote spina/strukturne $T_{\mathrm{SDW}}/T_{\mathrm{s}}$. Pri temperaturah pod $T_{\mathrm{SDW}}/T_{\mathrm{s}}$ se v relaksacijski dinamiki kvazidelcev pojavi ozko grlo, ki ga povezujemo z odpiranjem BCS-podobni temperaturno odvisni reži. Ugotovili smo, da se velikost reže zmanjšuje s povečanim dopiranjem, kar je v skladu z zmanjšanjem stabilnosti ortorombičnega/SDW stanja. Iz relaksacijskega časa v normalnem stanju določamo konstanto sklopitve elektronov in fotonov λ kot drugi moment Eliashbergove funkcije. V vseh treh preučevanih železovih pniktidih ima λ podobno vrednost, kar nakazuje zmerno sklopitev elektronov in fotonov.

Pri superprevodnih pniktidih in kupratih smo s povečano vzbujevalno fluenco opazili saturacijo superprevodne (SC) komponente. Iz fluenčne odvisnosti smo ocenili gostote uničevalne energije, U_d, SC stanja in ugotovili, da ima približno kvadratno odvisnost od T_{c}. To obnašanje smo obravnavali v okviru modela na osnovi fononsko posredovanega kvazidelčnega mehanizma ozkega grla.

Relaksacijsko dinamiko v normalnem stanju smo analizirali prek temperaturno neodvisne reže (psevdoreže). Ocenjene velikosti psevdoreže se zmanjšujejo s povečanim dopiranjem in so tako konsistentne z vrednostmi psevdoreže , ki so jih dobili iz T-odvisnosti Knightovega premika.

V vzorcih Ba-122, dopiranih s kobaltom, smo opazili dvoštevno rotacijsko anizotropijo glede na polarizacijo testnega sunka v nominalno tetragonalnem stanju do temperature $\sim$200 K. Anizotropija je posledica elektronskih nematičnih fluktuacij ali ureditve Fe d orbital.

Za preučevanje prehoda z zlomom simetrije v 1T-TaS_2 monokristalih smo vpeljali novo vpisovalno-črpalno-testno sunkovno tehniko. Pri teh eksperimentih sistem preklopimo z enim intenzivnim 50 fs sunkom v stanje z visoko simetrijo, nato pa opazujemo časovni razvoj s standardno črpalno-testno sekvenco. Prehod v novo skrito fotovzbujeno p-TaS_2 stanje (ON stanje) je bil dosežen na določenem energijskem pragu vpisovalnega pulza. Dokazano je bilo, da je novo stanje moč doseči samo po optični poti in da je stabilno do ~ 100 K. Da bi se vrnili nazaj v sistem iz stanja p-TaS_2 v CCDW-stanje (OFF stanje), uporabimo niz 50 ps dolgih sunkov. Prehod iz stanja ON/OFF je ponovljiv, spremlja pa ga sprememba odbojnosti in električne upornosti, kar odpira nove možnosti za generacijo ultrahitrih spominskih elementov.

Abbreviations

BCS	=	Bardeen-Cooper-Schrieffer
LBCO	=	$La_{2-x}Ba_xCuO_{4+\delta}$
LSCO	=	$La_{2-x}Sr_xCuO_{4+\delta}$
YBCO	=	$YBa_2Cu_3O_{7-\delta}$
BiSCO	=	$Bi_2Sr_2CuO_6$
Hg-123	=	$Hg_2Ba_2Ca_2Cu_3O_{10-\delta}$
CDW	=	charge-density-wave
AFM	=	atomic force microscopy
PM	=	paramagnetic
SP	=	single-particle
GL	=	Ginzburg-Landau
RT	=	Rothwarf-Taylor
QP	=	quasi-particle
HFP	=	high-frequency-phonon
TTM	=	two-temperature model
AC	=	alternating current
SDW	=	spin-density-wave
ICCDW	=	incommensurate CDW
NCCDW	=	near commensurate CDW
CCDW	=	commensurate CDW
BRF	=	birefringent
RR	=	retroreflector
P	=	polarizer
BS	=	beamsplitter
M	=	mirror
L	=	lens
AT	=	attenuator
AOM	=	acousto-optical modulator
PD	=	photo-diode
PE	=	pulse expander
DC	=	dispersion compensator
NMR	=	nuclear magnetic resonance
IBS	=	interband scattering
SC	=	superconducting
PG	=	pseudogap
ARPES	=	angle-resolved photoemission spectroscopy
FIR	=	far-infra-red
FS	=	Fermi surface
PE	=	photoexcited
SBPT	=	symmetry-breaking-phase-transition
FFT	=	fast Fourier transform
AM	=	amplitude mode

1 Introduction

> "Do not *follow* where the *path* may lead. Go *instead* where there is no path and leave a *trail*."
>
> Ralph Waldo Emerson

What is a superconductor? From its name, we can easily say that it is a material that conducts perfectly, *i.e.* has a zero resistance. This first condition which has to be fulfilled was discovered by Heike Kamerlingh Onnes [1] in 1911. While he was measuring the temperature dependence of the resistivity in a solid mercury wire, he noticed a sudden drop in the resistance, a new phenomenon which was named superconductivity. The second important property of the superconducting materials arises from their response in the external magnetic field. When a superconductor is cooled down below its critical temperature T_c and placed in a magnetic field, it behaves as a diamagnet, *i.e.* the total magnetic field is very close to zero deep inside the superconductor. The observed phenomenon of perfect diamagnetism in the superconductors is also known as Meissner-Ochsenfeld effect.

The pioneering work of H. K. Onnes has initiated enormous interest in the research of superconducting materials among scientists. As a result, plenty of new materials exhibiting superconductivity with T_c up to 23 K (Nb_3Ge) were discovered. All these superconductors belong to the group of the so-called conventional superconductors which are explained very well in the frame of the Bardeen-Cooper-Schrieffer (BCS) theory [2].

However, the picture of the physics behind the phenomenon of the superconductivity has changed dramatically in 1986, when K. A. Mueller and J. G. Bednorz [3] managed to synthesize a $La_{2-x}Ba_xCuO_{4+\delta}$ (LBCO) superconductor with $T_c = 35$ K. Soon afterwards, in the layered Cu-oxides (also called the cuprate supercoductors) such as $YBa_2Cu_3O_{7-\delta}$ (YBCO) [4], $Bi_2Sr_2CuO_6$ (BISCO) [5] and $Hg_2Ba_2Ca_2Cu_3O_{10-\delta}$ (Hg-123) [6] superconductity with T_c above liquid nitrogen temperature was observed, introducing the phenomenon of the high-temperature superconductivity. In 2008, another group of layered iron-based materials (pnictide superconductors) with critical temperatures up to 55 K has joined the family of high-temperature superconductors [7].

In contrast to the conventional superconductors, the origin of the superconductivity in high-T_c superconductors cannot be explained very well in the framework of the BCS theory. Detailed study of the interactions among electrons and other excitations is crucial for revealing the puzzle of the origin of the superconductivity in all strongly coupled systems. Elucidating the pairing mechanism might lead not only to new insights into the novel physics of correlated materials, but also to possible application of high-temperature superconductors. Once we solve the pairing mechanism puzzle, we might be holding the keys for achievement of the room-temperature superconductivity.

Related to the superconductors are those low-dimensional materials where the electron-phonon interactions lead to structural instabilities. Upon cooling down their translational symmetry is broken followed by appearance of the gap in the single particle excitation

spectrum. Since the charge density displays a periodic spatial variation, these systems are named charge-density wave (CDW) systems [8]. They show very astonishing features, since we can controllably change their state under the influence of light, current or electric field. From the applied point of view, similarly to chalcogenides, (As-Te-Ge films [9–11], for example) CDW systems are very promising materials as non-volatile ultrafast phase change memory elements.

Regarding the experimental technique to study the above mentioned materials, femtosecond laser spectroscopy has been shown to be a powerful tool in the investigation of quasiparticle recombination dynamics, giving complementary information on the electronic structure to more conventional spectroscopy techniques. Previous systematic experiments focused on measurement of the photoinduced changes of reflectivity (or transmissivity) as a function of different parameters, such as temperature, polarization or laser fluence have provided valuable information about superconducting and pseudogap states in different complex systems [12–28]. In other words, femtosecond laser spectroscopy can qualitatively improve and upgrade understanding not only of the dynamics of excitations on ultrafast time scale, but also static properties, which might lead to new insights in the physics of correlated materials and consecutively towards development of new materials with new functional properties.

Motivated by previous studies, we have performed systematic pump-probe experiments in iron-based pnictides and cuprates with the aim of elucidating the electronic structure and to obtain detailed information about the quasiparticle (QP) dynamics. In addition, recent results on symmetry breaking transitions in $TbTe_3$ [25] were a strong motivation to extend the study of time evolution of single particle and collective excitation to the CDW systems.

This thesis is organized as follows. In Chapter 1, we briefly introduce the main physical properties of the high-temperature superconductors and charge-density wave systems. In the first part of Chapter 1, some important structural and electronic properties of the cuprates, pnictides and CDW systems will be presented, followed by introduction to the dynamics of broken symmetry states. Here, we give some basic theoretical expressions related to the Ginzburg-Landau and Bardeen-Cooper-Schrieffer theory and some theoretical models which have been employed in the data analysis. We introduce the terms of destruction and condensation energy and discuss the heating effects.

Chapter 2 starts with some peculiarities of the samples and detailed description of the preparation of the samples. We present the experimental setup used in our laboratory and briefly describe the generation of ultra short laser pulses. At the end, we describe the characterization of the laser beams employed in our experiments.

Chapter 3 is dedicated to the extensive study of the relaxation dynamics in $SmFeAsO_{1-x}F_x$, $SrFe_2As_2$ and $Ba(Fe_{1-x}Co_x)_2As_2$ iron-based pnictides. Detailed temperature and fluence dependencies study on the reflectivity transients is presented. Relaxation dynamics in the spin-density-wave (SDW), superconducting (SC) and normal state of the phase diagram is discussed with the emphasis on the estimation of the gaps, SC state destruction and the electron-phonon coupling.

In Chapter 4, we continue with fluence dependence study in $YBa_2Cu_3O_{7-\delta}$. From comparison between the destruction and condensation energy, we introduce a model based on the phonon-mediated quasiparticle bottleneck mechanism. At the end, we propose a mechanism for a nonthermal destruction of the SC state in both systems: pnictides and cuprates.

Chapter 5 covers an extensive study of the $\Delta R/R$ transients in the high-fluence regime in the commensurate phase of 1 T-TaS_2. We observe for the first time a bistable switching from the thermodynamical ground state to a new hidden state of matter by a single ultrashort laser pulse. Some further applications will be proposed.

In Chapter 6, we summarize the thesis and present the conclusions.

In the following sections, we review some general physical properties of the cuprate and iron-based pnictide superconductors as well as of charge-density wave systems. Their crystal structure, phase diagram and electron and normal state properties will be discussed in more

detail. At the end, we introduce the theoretical background of destruction and condensation energy and discuss the heating effects.

1.1 Cuprate superconductors

High-T_c superconducting cuprates are anisotropic layered structures similar to perovskites (Fig. 1). The anisotropic crystal structure of the cuprates is reflected by anisotropy in various physical quantities (for example, the electrical conductivity, the magnetic penetration depth λ and the coherence length ξ are strongly anisotropic). The degree of both electronic and optical anisotropy varies strongly from one family of the cuprates to another. In the most anisotropic single-layered $Bi_2Sr_2CuO_6$ (Bi-2201) the ratio between the in-plane and out-of-plane electrical conductivity is 10^4, whereas in $YBa_2Cu_3O_7$ this factor is only $\simeq 10$.

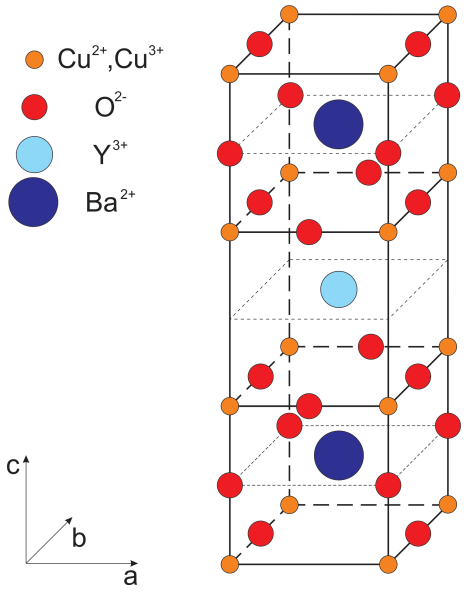


Figure 1: Representation of $YBa_2Cu_3O_{7-\delta}$ unit cell. It consists of two CuO_2 planes with Y ion in between. It is believed that CuO_2 planes are responsible for the superconductivity. Above and below CuO_2 planes are the charge reservoirs.

The common structural element in cuprates is the set of n (n=1,2,3) CuO_2 planes which is thought to be responsible for the superconductivity. Moreover, it was found that the critical temperature T_c is increasing with the number of CuO_2 planes up to $n = 3$. Above and below the CuO_2 planes there are charge reservoirs layers that can accept or donate electrons from/to the CuO_2 planes. This can be done either by a chemical substitution ($La_2CuO_4 \rightarrow La_{2-x}Sr_xCuO_4$), by changing oxygen stoichiometry in charge reservoir layers ($YBa_2Cu_3O_{7-\delta}$) or by combination of both.

A schematic phase diagram for electron and hole doped cuprates is given in Fig. 2. Most of the high-T_c superconductors are hole doped and therefore we will discuss only hole doped cuprates. When hole concentration p (measured in holes per Cu ion in CuO_2 plane) is low, cuprates behave as antiferromagnetic insulators. The underdoped parent compounds of high-T_c cuprates are Mott-Hubbard insulators. By increasing the hole concentration, antiferromagnetic properties disappear and for $p = 0.05$ the superconducting properties appear at low temperatures. When the doping is ~ 0.15, the critical temperature reaches maximum value and therefore this hole concentration is referred as the optimum doping. Further increasing of p results in decrease of T_c and for $p > 0.25$ (overdoped region) the superconductivity vanishes and materials behave more or less as an ordinary metal.

One region of the phase diagram that has attracted a great deal of attention is the so-called pseudogap state. The term pseudogap refers to the decrease in the density of

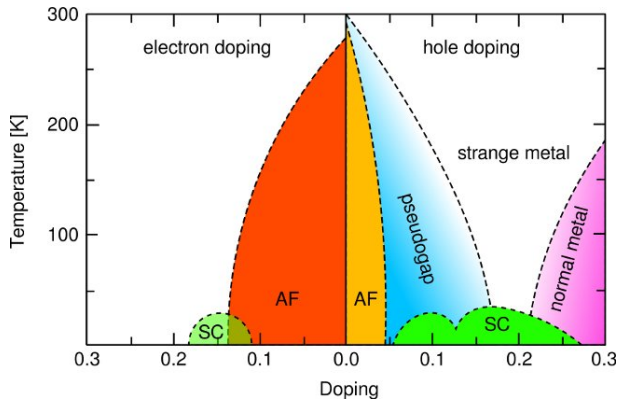


Figure 2: Schematic phase diagram of the electron and hole doped cuprates.

states near the Fermi level E_F observed at temperatures above T_c. An example of such a partial gap (pseudogap) would be a situation where, within the band-theory approximation, some regions of the Fermi surface become gapped while other parts retain their conducting properties and with increased doping the gapped portion diminishes and the materials become more metallic. The pseudogap was firstly discovered in underdoped $YBa_2Cu_3O_{7-\delta}$ by nuclear magnetic resonance (NMR) [29], where instead of temperature independent Pauli susceptibility a decrease in the Knight shift was observed. Since NMR is sensitive to various momentum averages of the spin excitations it was used to support the hypothesis of a spin gap. However, various experimental techniques [30, 31] confirmed the existence of the pseudogap in both the spin and the charge channels. Therefore it appears to be a common feature of the cuprates. Clarifying the nature of the phenomenon of the pseudogap might lead to revealing the origin of the high-temperature superconductivity. However, the presence of the pseudogap still evokes plenty of discussions among scientists.

As we have mentioned before, by introducing a moderate density of charge carriers (electrons or holes) into a parent Mott-Hubbard insulators, its physical properties are radically modified and the material becomes underdoped, overdoped or optimally doped superconductor. It is important to mention that doping of a parent compound does not necessarily result in a spatially homogenous distribution of charge carries, *i.e.* the stripe phase might occur [32]. The stripe phase is consisted of charge-rich regions separated by regions with strongly depleted carrier density. A number of experiments and theoretical studies have been involved into clarification of the existence of the striped phase, since its relevance to the phenomenon of high-temperature superconductivity is still debated.

1.2 Iron-based superconductors

Iron-based superconductors belong to the recently discovered new family of high-temperature superconductors [7]. Similarly to cuprates, all five different structural classes of iron-based superconductors have a common layered structure (see Fig. 3). It is based on a planar layer of iron atoms joined by tetrahedrally coordinated pnictogen (P, As) or chalcogen (S, Se, Te) anions arranged in a stacked sequence separated by alkali, alkaline-earth or rare-earth and oxygen/fluorine "blocking layers". It is believed that Fe-As layers play the main role in the origin of the high-temperature superconductivity.

Besides many similarities to cuprates, there are several key differences which should be highlighted [33]. Firstly, the parent compounds have a multiband metallic nature (rather than insulating), the substitution or doping can happen directly into the active SC layer and finally there is a significant difference in the arrangement of pnictogen/chalcogen anions above and below the almost planar iron layer as opposed to the planar copper-oxygen structure of the cuprates. Switching to the superconducting phase in the phase diagram can

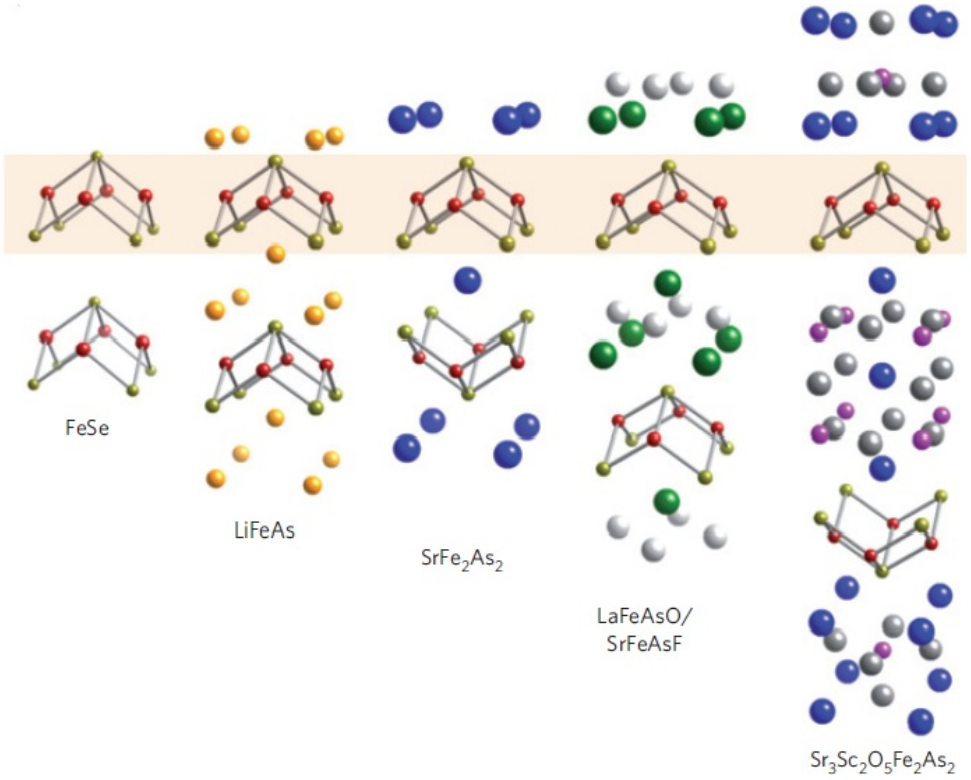


Figure 3: Schematic of five known structures of iron-based pnictides. The iron layer responsible for the superconductivity consists of iron ions shown in red and pnictogen/chalcogen ion shown in gold. Adopted from Ref. [33].

be achieved either by chemical doping/substitution or by application of external pressure to suppress the antiferromagnetic, non-superconducting phase. In addition, the theoretical calculations favour the s± gap symmetry [34, 35] which is different but related to the previously observed $d_{x^2-y^2}$ gap symmetry in the cuprates.

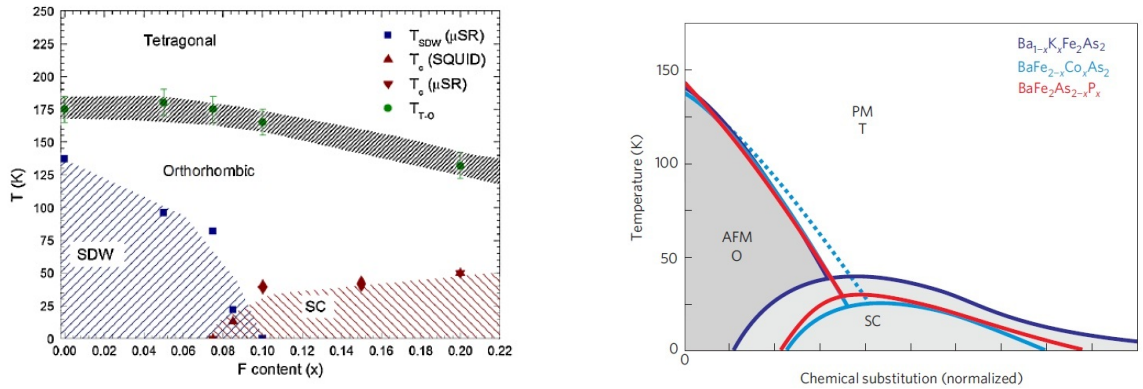
Below the room temperature in the range of 100–210 K, the undoped iron-based superconductors undergo a weakly first or second order structural transition at T_s from tetragonal to orthorhombic, and a magnetic transition at T_N from non-magnetic to a stripe antiferromagnetic. The structural transition and the magnetic order transition can happen simultaneously or successively depending on the compound. It was confirmed both experimentally and theoretically [36, 37] that the magnetic order of Fe at low temperature is stripe-like antiferromagnetism often referred to as spin-density wave (SDW) due to nesting properties of the multiband Fermi surface [38]. Spin-density wave ground state develops as a consequence of the electron-electron interaction. In the SDW state a gap opens at the Fermi level. As we will discuss in section 1.4, similarly to a charge-density wave state, SDW state is an example of a broken symmetry state with a periodically varying electron spin density and it has well defined magnetic response, similar to antiferromagnetic. Upon doping or compressing, the magnetic order is suppressed and the material becomes superconducting.

As we have mentioned before, iron-based superconductors are classified into five different groups. In this thesis, the subject of the research are samples from two different classes of iron-based superconductors: XFeAsO ($X =$ La, Dy, Tb, Gd, Sm, Nd, Pr, Ce) doped with F and Co and $Y Fe_2As_2$ ($Y =$ Ba, Sr, Ca, and Eu). Compounds from the first class are referred as "1111"-family, where the second class is known as "122"-family of iron-based superconductors. Spin-density wave and structural transition are happening at different temperatures in "1111"-family, but coincide in temperature in the undoped "122"-family. In the "1111"-family, T_N is lower than T_s, which seems to suggest that the magnetic transition is induced by the structural transition. In contrast, in "122"-family, $T_N = T_s$, *i.e.*, the structural

and magnetic transitions happen simultaneously (a first-order transition). Whether the magnetic transition is induced by the structural transition or not and what is the driving force of the structural transition are two important questions that are crucial in order to understand the formation of the stripe antiferromagnetic order in the parent compounds.

As an example of "1111"-family we have studied F doped SmFeAsO samples, for which the phase diagram is shown in Fig. 4 (a). From the phase diagram we can see that orthorhombic to tetragonal structural transition boundary exhibits a slight decrease with increasing F content. As the F content increases the T_{SDW} decreases up to a critical value of F ($x \sim 0.07$) above which the SDW is suppressed in the favour of superconductivity.

The phase diagram of the iron-based $BaFe_2As_2$ compound from "122"-family is presented in the Fig. 4 (b). The dotted line indicates the structural transition between tetragonal (T) and orthorhombic (O) crystallographic phases observed for Co-substitution, which is coincident with the paramagnetic (PM) to antiferromagnetic transition in the parent compound $BaFe_2As_2$. Despite of the ease by which "122"-compounds can be prepared in a single crystal form, there are several differences in comparison with "1111"-compounds. While a number of "1111"-compounds have magnetic ordering of the lanthanide site rare earth ion (Pr, Ce, Nd, Sm) in addition to the ordering of the Fe, in the "122" undoped parent compounds there is only $EuFe_2As_2$ where, in addition to the Fe ordering at 190 K the Eu orders antiferromagnetically below 19 K and $EuFe_2(As_{1-x}P_x)_2$, for $x \geq 0.22$, the Eu ordering becomes ferromagnetic [38]. The existence of the pseudogap in these materials is



(a) (b)

Figure 4: (a) The phase diagram of $SmFeAsO_{1-x}F_x$ system up to $x \leq 0.20$. $T_{\mathrm{T-O}}$ refers to the temperature of tetragonal to orthorhombic structural transition and abbreviation μSR stands for mion spin rotation. Adopted from Ref. [39]. (b) Chemical-substitution phase diagram of the $BaFe_2As_2$ system, shown for K, Co and P doping, with the amount of chemical substitution (x) normalized to overlap the descent of the antiferromagnetic transition for simplified comparison of the relative position of the SC phase. Adopted from Ref. [33].

still controversial, since no strong anomalies have been noticed in the normal state in-plane transport properties.

1.3 Charge-density wave systems

As an example of quasi-two dimensional charge-density wave system we studied the 1*T*-TaS_2 system [40–43]. It has a simple crystal structure, composed of planes of tantalum (Ta) atoms, surrounded in an octahedral arrangement by sulphur (S) atoms (Fig. 5). What makes this material so challenging for a study is the existence of many phase transitions. At high temperatures the system is in a metallic phase where at $T = 550$ K a transition to an incommensurate CDW (ICCDW) phase occurs. With further cooling down the system

undergoes a transition from nearly commensurate CDW (NCCDW) phase at $T = 350$ K to commensurate CDW (CCDW) phase at $T = 180$ K. The phase transitions from ICCDW to NCCDW and from NCCDW and CCDW are of first order and therefore a large hysteresis is observed (see Fig. 6).

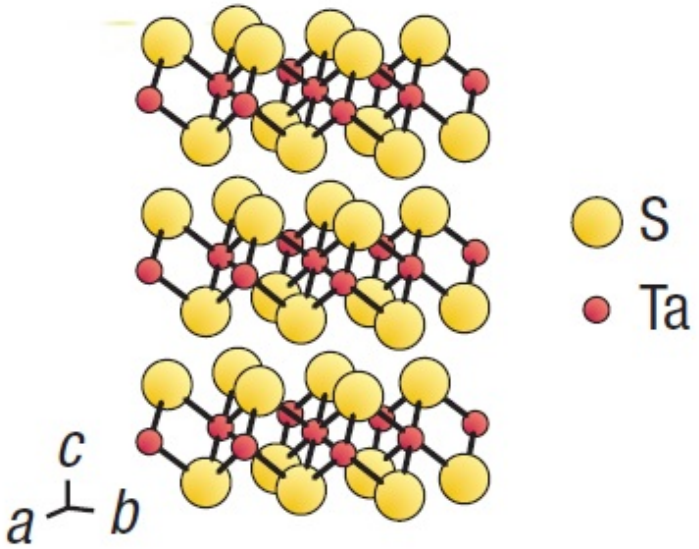


Figure 5: A simple schematic representation of the crystal structure of 1 T-TaS_2. Adopted from [45].

The CCDW phase is geometrically the simplest among the CDW phases in this material. The displacement of the atoms leads to the formation of David-star clusters (they exist also in the NCCDW phase, but they are arranged in less uniform manner), where twelve Ta atoms within the layer move inwards towards a thirteenth central Ta atom. The stars interlock by forming a triangular superlattice. In the CCDW phase, due to the Mott localization [44], the gap appears throughout the Fermi surface. The phenomenon of high resistivity of this phase can be described via development of a Mott insulator state by the electrons near the Fermi energy. The formation of the David-star clusters causes a periodic swelling of the TaS_2 layers. Therefore, the CCDW Mott phase is sensitive to doping, disorder caused by irradiation and pressurization [45].

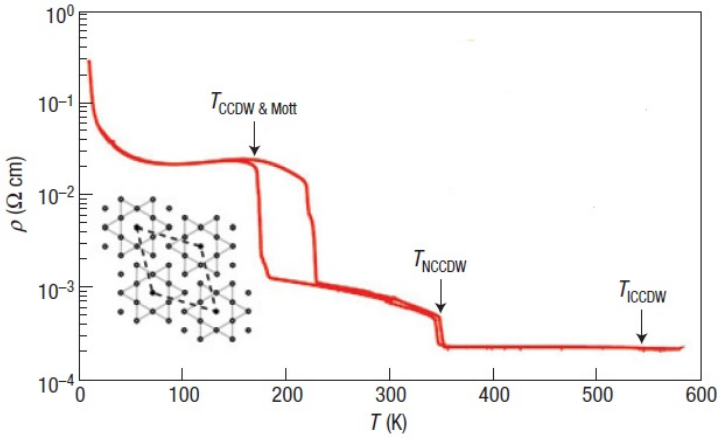


Figure 6: Resistivity measurements on 1 T-TaS_2. In the bottom left inset the Ta atom distortion in the CCDW phase is shown. Adopted from Ref. [45].

Layered dichalcogenide TaS_2 has several polytypes that differ in both the local coordi-

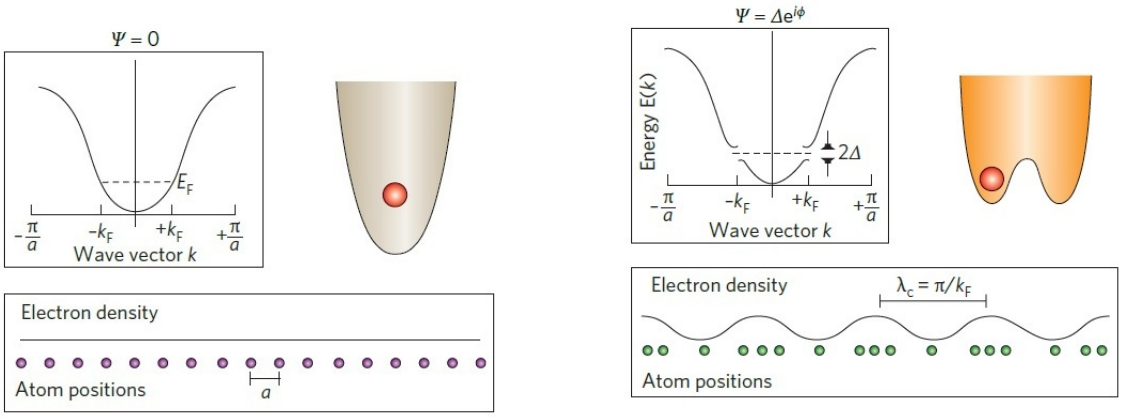
nation of the TaS_6 polyhedron - either octahedral or trigonal prismatic - and the number of TaS_2 layers in an elementary cell. The $1T$ form has a single layer of TaS_6 octahedra sharing edges while $2H$ form is based on edge-sharing TaS_6 trigonal prisms. The $4H$, $3R$ and $6R$ polytypes are also known [46].

1.4 Physics of charge- and spin-density wave systems

The term of the charge-density wave instability was firstly introduced by R. Peierls and H. Fröhlich in the 1955 and later on experimentally observed in the low-dimensional materials [8, 40, 41]. Charge- and spin-density wave systems present an example of a broken symmetry ground state, originating from the electron-phonon (charge-density wave systems) or electron-electron (spin-density wave systems) interactions. These states are characterized by a coupled instability of the electron-lattice or electron-spin subsystem, and often compete with other broken symmetry ground states such as superconductivity. One key ingredient for the formation of charge- and spin-density wave ground states are strong and anisotropic *e-ph* or *e-e* coupling constants and a high density of states at the Fermi level $n(E_F)$ [8]. In contrast to the 3D system, the response function for the low-dimensional systems diverges at wavevector $q = 2k_F$. The Lindhard response function for one-dimensional system at $T = 0$ is given by [8]:

$$\chi(q) = \int \frac{d\vec{k}}{2\pi} \frac{f_k - f_{k+q}}{\varepsilon_k - \varepsilon_{k+q}} = \frac{e^2}{\pi\hbar v_F} \ln \left| \frac{q + 2_{k_F}}{q - 2_{k_F}} \right|. \tag{1}$$

The divergence arises from the specific topology of the Fermi surface referred to as a perfect nesting. This means that an external perturbation will lead to a charge redistribution and subsequently to the formation of a periodically varying electron charge density (Fig. 7). The period $\lambda_0 = \pi/k_F$ of spatial variation is associated with the appearance of the gap in single particle excitation spectrum at the Fermi level.



(a) (b)

Figure 7: Single particle band, electron density and lattice distortion in the metallic state above T_{CDW} (a) and in the charge-density wave state (b) at $T = 0$. The red dot denotes the state of the system. Adopted from Ref. [47].

In the following, we will concentrate on the description of the charge density wave ground state and its implications for the band structure; however, similar concepts hold for the spin-density wave formation [8]. A charge-density wave system can be treated using the mean field approach, where the transition temperature T_{CDW} is defined with [8]:

$$k_B T_{CDW}^{MF} = 1.14\varepsilon_0 e^{-1/\lambda}, \tag{2}$$

where the ε_0 is referred to a cut-off energy usually taken to be equal to the Fermi energy and λ stands for the dimensionless electron-phonon coupling constant. When the CDW system undergoes a phase transition, one of the phonon frequencies, renormalized due to the electron-phonon interaction, goes to zero at $q = 2k_F$, *i.e.* the so-called Kohn anomaly appears [48]. From the BCS theory, we know that the amplitude of the order parameter Δ is related to the magnitude of the gap. Therefore, for the CDW systems the BCS relation at $T = 0$ can be written as [8]:

$$2\Delta_{CDW} = 3.52 k_B T_{CDW}^{MF}. \tag{3}$$

The cut-off energy in CDW systems is the Fermi energy ε_F instead of Debye frequency ω_D in the BCS superconductor and therefore the CDW systems have a much higher transition temperatures compared to the BCS superconductors. The appearance of the single particle (SP) gap, for example, also leads to a finite coherence length ξ which corresponds to the spatial dimension of the electron-hole pairs. At zero temperature it is given by a BCS expression [8]:

$$\xi_0 = \frac{\hbar v_F}{\pi \Delta_{CDW}}, \tag{4}$$

where v_F is the Fermi velocity.

Plenty of experiments have proven the existence of the charge-density wave ordering by measuring the specific heat, thermal expansion, or elastic constants [8]. CDW phase transitions have been observed by neutron or electron diffraction [49], Raman scattering [50] and many different optical experiments [51, 52]. There are many different materials which exhibit a charge-density wave ordering, such as mixed valence platinum chain (for example $K_2Pt(CN)_4Br_{0.3}{\cdot}3.2H_2O$), transition metalchalcogenides (MX_3 and $(MX_4)_nY$, M=Ta, Nb; X=S, Se; Y=I, Br, Cl) and transition blue bronze compounds ($A_{0.3}MoO_3$, A=K, Rb, Tl). A compound (Tetramethyltetraselenafulvalene)$_2PF_6$ $(TMTSF)_2PF_6$ also known as Bechgaard salt is an example of organic CDW material. All these CDWs are one-dimensional (1D) materials. On the other hand, layered dichalcogenides such as $NbSe_3$, $TaSe_3$, $TbTe_3$, $TaSe_2$ and TaS_2 are examples of two-dimensional (2D) CDW materials.

Since it is beyond the scope of this thesis to give an extensive description of the details we advise the book written by Gruener [8] for further reading.

1.5 Dynamics of broken symmetry states

This section overviews the most important theoretical aspects of the dynamics of broken symmetry state. It covers some fundamentals about theory of the superconductivity and the mechanism of the relaxation of the superconducting state.

1.5.1 Fundamentals of the Ginzburg-Landau and Bardeen-Cooper-Schrieffer theory

After the discovery of the phenomenon of the superconductuvity, three famous theories: London, Ginzburg-Landau and Bardeen-Cooper-Schrieffer theories have been proposed for the explanation of the superconducting state. The first theory which proved successful in describing the electrodynamics of the superconductors was the London theory [53]. Later on, this theory was extended by taking into account the quantum effects. The new theory, called the Ginzburg-Landau theory [54], was built on the basis of the theory of the second-order phase transitions. According to this theory, the free energy can be expanded in powers of the order parameter.

The first theory which explained the microscopic mechanism was proposed by J. Bardeen, L. N. Cooper and J. R. Schrieffer [2]. This microscopic theory considers that the interaction between the electrons and phonons leads to a specific electron-electron interaction, *i.e.*

creating the Cooper pair. In the following two subsections, the fundamentals of both theories will be presented.

The Ginzburg-Landau (GL) theory considers that the formation of superconducting state is a second-order phase transition and, it is a more ordered state than the normal state. The GL theory was built on the basis of the theory of the second-order phase transition (the Landau theory) and therefore, it is valid only in the vicinity of the critical temperature *i.e.* within the temperature range $T_c - T \ll T_c$. According to the Landau theory, the free energy can be expanded in powers of the order parameter.

Ginzburg and Landau introduced the macroscopic wave function $\psi(r)$, $\psi(r) = n_s^{\frac{1}{2}} e^{i\phi(r)}$ as a complex order parameter. In addition, the normalization $|\psi(r)|^2 = \frac{n_s}{2}$ of this function represents the local density of the superconducting electrons n_s. By taking into assumption that $\psi(r)$ is small and varies slowly in space, we can expand the superconductor free energy density into a series in the temperature region around the transition temperature T_c [55]:

$$f_s = f_n + \alpha|\psi|^2 + \frac{\beta}{2}|\psi|^4 + \frac{1}{2m}\left|\left(-\hbar i \bigtriangledown - 2e\overrightarrow{A}\right)\psi\right|^2 + \frac{|\overrightarrow{B}|^2}{2\mu_0}, \tag{5}$$

where m is an effective mass, e is the charge of an electron, $\overrightarrow{A}$ is vector potential defined with $\overrightarrow{B} = \bigtriangledown \times \overrightarrow{A}$ and μ_0 is the magnetic permeability of free space. There is one more GL equation that determines the SC current $\overrightarrow{j_s}$ [55]:

$$\overrightarrow{j_s} = -\frac{2e}{m} i\hbar(\Psi^* \bigtriangledown \Psi - \Psi \bigtriangledown \Psi^*) - 2e|\Psi|^2 \overrightarrow{A}, \tag{6}$$

where $\overrightarrow{j_s}$ is current density in the superconductor. In the absence of the magnetic field and gradients, the GL equation [55]:

$$f_s - f_n = \alpha|\psi|^2 + \frac{1}{2}\beta|\psi|^4, \tag{7}$$

has two solutions, depending on the coefficient α (coefficient β is positive and independent of temperature). If $\alpha < 0$, the minimum free energy occurs at $|\psi|^2 = 0$, corresponding to the normal state. For $\alpha > 0$, the minimum appears when $|\psi|^2 = -\frac{\alpha}{\beta}$.

By substituting the last solution for the minimum free energy in the GL equation, for the energy difference we have:

$$f_s - f_n = \frac{-\alpha^2}{2\beta}, \tag{8}$$

where the first term in this equation represents the condensation energy per unit volume, defined with [55]:

$$f_s - f_n = -\frac{\overrightarrow{H}_c^2(T)}{8\pi}, \tag{9}$$

where $\overrightarrow{H}_c^2(T)$ is the critical magnetic field.

By using the variation principle and assuming a series expansion of the free energy in powers of ψ with expansion coefficients α and β, we can derive the following differential equation for ψ [55]:

$$\alpha\psi + \beta|\psi|^2\psi + \frac{1}{2m}\left(-\hbar i \bigtriangledown - 2e\overrightarrow{A}\right)^2 \psi = 0 \tag{10}$$

Ginzburg-Landau theory defines two important lengths in the superconducting state: the coherence length ξ and London penetration depth λ. The London penetration depth

represents the typical distance to which the magnetic field penetrates into a superconductor [55]:

$$\lambda = \left(\frac{mc^2}{4\pi n_s e^2} \right)^{\frac{1}{2}}. \tag{11}$$

The second length, named the coherence length is a temperature and material dependent quantity, defined with [55]:

$$\xi = \left(\frac{\hbar^2}{2m\alpha} \right)^{\frac{1}{2}}. \tag{12}$$

The length ξ is of fundamental importance in the superconductivity, representing the shortest distance over which the wavefunction ψ is allowed to vary without breaking of the pairs. The coherence length is quite long in the low-T_c materials ($\xi = 12 - 14$ nm in $CeCu_2Si_2$) and quite short in the high-T_c superconductors (ξ =2.5 and 1.3 nm in YBCO and Hg-123, respectively) [56]. It is also useful to introduce the dimensionless and temperature independent Ginzburg-Landau parameter k, which is defined as the ratio of these two characteristic lengths:

$$k = \frac{\lambda}{\xi}. \tag{13}$$

Regarding to the response of the superconducting materials in the external magnetic field $\overrightarrow{H}_0$, they are divided into type I and type II superconductors. Type I superconductors include all superconducting elements except niobium. Niobium, superconducting alloys and high-T_c superconductors belong to the second type II superconductors. In order to explain what is difference between these two groups, let us imagine that we have type I superconductor (in its superconducting state) placed in a weak $\overrightarrow{H}$ magnetic field. As the field is increasing, after reaching the value of $\overrightarrow{H}_c$, the superconducting state is destroyed and the field penetrates inside the superconductor. In type II superconductors the flux begins to penetrate in a very special way: as quantized vortex filaments in the sample for the applied fields in the range $\overrightarrow{H}_{c1}(T)$ and $\overrightarrow{H}_{c2}(T)$. If we apply magnetic field higher than $\overrightarrow{H}_{c2}(T)$ type II superconductor reverts back to the normal non-superconducting state. The Ginzburg-Landau parameter is $k<\frac{1}{\sqrt{2}}$ and $k>\frac{1}{\sqrt{2}}$ for type I and type II superconductors, respectively.

After almost 50 years after the discovery of the superconductivity, the mechanism of superconductivity was explained with the microscopic theory of superconductivity [2]. The theory was proposed by J. Bardeen, L. N. Cooper and J. R. Schrieffer, who were awarded the Nobel prize for their work in 1972.

The discovery of the isotope effect (different isotopes of the same superconductor have different critical temperatures) showed that superconductivity arises from the interactions between electrons and lattice vibrations. Interaction between electrons and lattice vibrations (phonons) can give rise to specific form of electron-electron interaction, which lead to pairing/Cooper pair formation.

The electron-electron interaction can be explained as follows (see Fig. 8). Let us imagine a metal at $T = 0$ K and one electron with wave vector $\overrightarrow{k_1}$ traveling through the crystal lattice of the metal. At some moment of time, this electron will interact with the lattice and as a consequence of the interaction, a phonon will be created. If we denote the wave vector of the phonon with $\overrightarrow{q}$ and wave vector of the electron after interaction with $\overrightarrow{k}'_1$, by the law of momentum conservation we have:

$$\overrightarrow{k_1} = \overrightarrow{k}'_1 + \overrightarrow{q}. \tag{14}$$

The phonon $\overrightarrow{q}$ is immediately absorbed by the second electron with wave vector $\overrightarrow{k_2}$ and due to that the electron goes to a new state $\overrightarrow{k}'_2$. We have observed interaction between

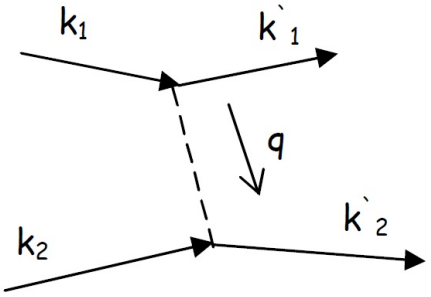


Figure 8: Schematic for the electron-electron interaction via phonon. First electron with wave vector $\overrightarrow{k_1}$ interacts with the second electron with wave vector $\overrightarrow{k_2}$ via phonon $\overrightarrow{q}$. After the interaction, two electron have different wave vectors $\overrightarrow{k}'_1$ and $\overrightarrow{k}'_2$, respectively. Adopted from [55].

these electrons via phonon $\overrightarrow{q}$. When the electron passes through the crystal lattice, at some moment it will be close to an ion. This ion will be attracted to negative electron charge and will start to compensate it. The ion has larger mass than the electron and due to that it takes more time to return back to its equilibrium position. Slower returning, creates positive charge. The second electron will be attracted to the positive charge, *i.e.* the two electrons are attracted to each other.

All Cooper pair states belong to the condensate occupying the ground-state energy level which is separated from the elementary excitations (electrons and holes) by an energy gap Δ (Fig. 9). A single extra elementary excitation (quasiparticle) is not allowed to be in the ground-state energy level and must therefore occupy the first empty level available in the elementary excitation spectrum. If a pair is broken, both electrons must go up to the elementary excitation levels which requires an energy larger than 2Δ.

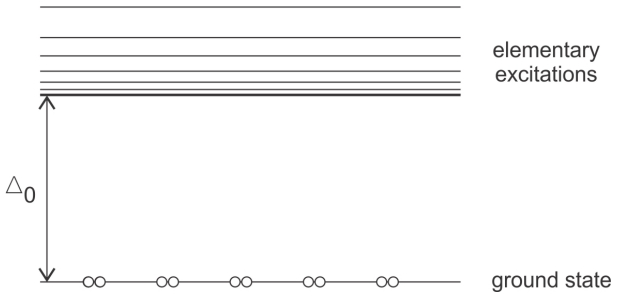


Figure 9: The energy gap Δ_0 separates the energy levels of elementary excitations from the ground-state level (Cooper pairs). Adopted from [55].

The temperature-dependent order parameter $\Delta(T)$ is given with the BCS relation as [55]:

$$\Delta(T=0) = 2\omega_{\mathrm{D}} \frac{\exp(-1/\lambda)}{1-\exp(-1/\lambda)}, \tag{15}$$

where $\lambda = n(E_{\mathrm{F}})V$, V refers to the electron-ion coupling strength and ω_{D} is the Debye frequency.

For the weak coupling limit ($N(0)V < 1$) the Eq.(15) becomes [55]:

$$\Delta(T=0) = 2\omega_{\mathrm{D}} \exp(-1/\lambda), \tag{16}$$

where the T_{c} is expressed with [55]:

$$k_{\mathrm{B}} T_{\mathrm{c}} = 1.14\omega_{\mathrm{D}} \exp(-1/\lambda). \tag{17}$$

Combining Eq.(16) and (17) leads to the expression for the energy gap $\Delta(T=0)$ [55]:

$$2\Delta(0) \sim 3.52 k_{\mathrm{B}} T_{\mathrm{c}}. \tag{18}$$

In contrast, for the strong coupling limit we have [55]:

$$\Delta(T=0) = 2\omega_{\mathrm{D}}\lambda, \tag{19}$$

and for the critical temperature T_{c} we have [55]:

$$k_{\mathrm{B}}T_{\mathrm{c}} = \omega_{\mathrm{D}}\lambda/2. \tag{20}$$

The ground state energy in the weak coupling limit is evaluated as [55]:

$$U = -\frac{1}{2}N(0)\Delta^2(0), \tag{21}$$

where $N(0)$ represents the density of states at the Fermi level and Δ is the superconducting gap.

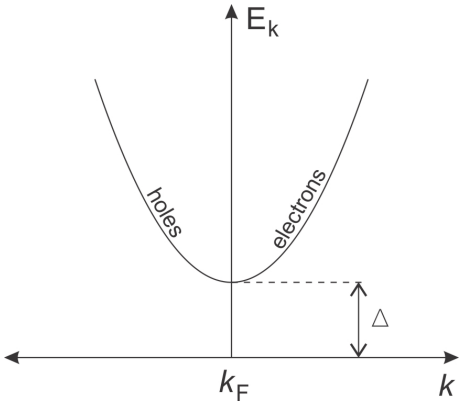


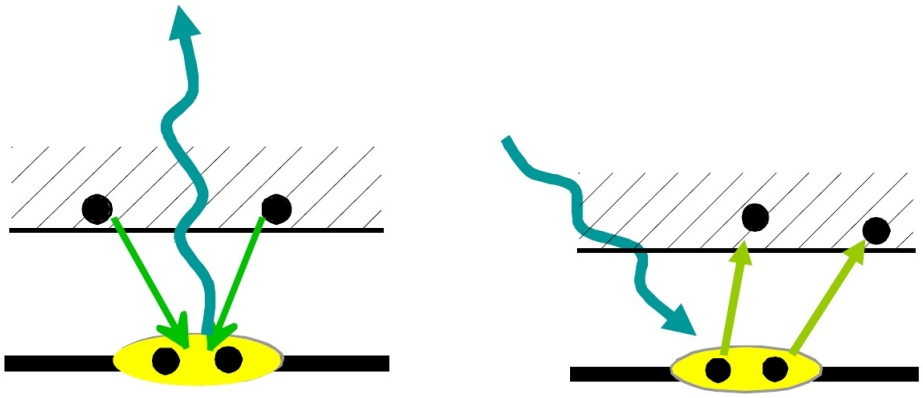
Figure 10: A sketch for the energy spectrum of the quasiparticles in the superconductor.

In order to understand the formation of the quasiparticles in the superconductor, let us add one extra electron to a superconductor at $T = 0$ K. It will occupy one of the vacant $\overrightarrow{k}$ states in the momentum space, while the state $-\overrightarrow{k}$ will remain empty. But unlike the normal metal, in the superconductor, the state $\overrightarrow{k}$ can be either inside or outside the Fermi surface. Thus, in the superconductor, the momentum of an electron-like quasiparticle can be not only greater, but also less than k_{F}, *i.e.* the condition $|k-k_{\mathrm{F}}|/k_{\mathrm{F}} \gg \Delta/\varepsilon_{\mathrm{F}}$ and $k > k_{\mathrm{F}}$ for momentum $\overrightarrow{k}$ is satisfied (Fig. 10). Conversely, if we remove one electron from the state $-\overrightarrow{k}$ in the ground state of a superconductor, the complementary electron in the state $\overrightarrow{k}$ will become uncoupled and start behaving in the same manner as a hole with momentum $\overrightarrow{k}$ for which the inequality $|k-k_{\mathrm{F}}|/k_{\mathrm{F}} \gg \Delta/\varepsilon_{\mathrm{F}}$ and $k < k_{\mathrm{F}}$ is valid.

1.6 Kinetics in the superconducting state

Considerable experimental and theoretical effort has been directed to understanding and explaining the nonequillibrium dynamics of electrons. The rapid development of new experimental techniques, like angle-resolved photoemission, scanning tunneling spectroscopy and ultrafast laser spectroscopy, has also greatly improved the quality and analysis of the experimental data. Detailed study of the quasiparticle relaxation dynamics is crucial in gaining important information about electron-electron and electron-phonon interactions.

The most commonly used theoretical model for the representation of the dynamics in superconductors is the Rothwarf-Taylor (RT) model [57]. According to this phenomenological model, when two quasiparticles (QP) (their energy is greater than the energy of the superconducting gap Δ) recombine into a Cooper pair, a high-frequency phonon (HFP) is created (Fig. 11). If we denote the phonon frequency with ω_{ph} then the inequality ($\omega_{ph} > 2\Delta$) is



(a) (b)

Figure 11: (a) Process of recombination of two quasiparticles into a Cooper pair and creating high-frequency phonon. (b) Breaking up of a Cooper pair into two quasiparticles by the high-frequency phonon.

valid. The emitted high-frequency phonon has enough energy to break a Cooper pair and due to that the recovery depends on the decay of the HFP population.

RT model consists of two nonlinear differential equations [57]:

$$\begin{aligned} \frac{dn}{dt} &= I_0 + \eta N - Rn^2 \\ \frac{dN}{dt} &= J_0 - \eta\frac{N}{2} + \frac{Rn^2}{2} - \gamma(N - N_T), \end{aligned} \tag{22}$$

where n and N are the concentrations of QPs and HFPs, respectively, η refers to the probability for pair breaking by HFP absorption and R is the recombination coefficient. N_T stands for the concentration of the HFP at thermal equilibrium at temperature T and γ is the HFP decay rate. I_0 and J_0 are external sources of QPs and HFPs, respectively. The factor $\frac{1}{2}$ in the second equation from (**??**) arise because one phonon creates two quasiparticles.

We can simplify the RT equations by introducing dimensionless concentrations of QPs and HFPs: $q = \frac{Rn}{\eta}$ and $p = \frac{RN}{\eta}$, respectively.

After substitution, the new form of RT equations is [58]:

$$\begin{aligned} \frac{dq}{d\theta} &= p - q^2 \\ \frac{dp}{d\theta} &= -\frac{p}{2} + \frac{q^2}{2} - \tilde{\gamma}(p - p_T), \end{aligned} \tag{23}$$

with dimensionless time $\theta = \eta t$ and HFP decay rate $\tilde{\gamma} = \frac{\gamma}{\eta}$ and $p_T = RN_T/\eta$ is the dimensionless concentration of HFPs in thermal equilibrium. Moreover, the initial conditions are: $p(0) = p_0$ and $q(0) = q_0$.

Depending on the decay rate of HFPs and density of the QPs and HFPs, we can distinguish several limiting cases as follows. If the density is small $(p_0 - p_T)$, $(q_0 - q_T) \ll 1$ we have weak perturbation regime, while the opposite case is referred to as strong perturbation regime. Depending on $\tilde{\gamma}$ we can distinguish two regimes: strong bottleneck regime $(\tilde{\gamma} \ll 1)$ and a weak bottleneck regime $(\tilde{\gamma} \gg 1)$.

BCS theory allows to estimate the QPs and HFPs density per unit cell at given temperature T [58]:

$$\begin{aligned} n_T &\cong N(0)\sqrt{2\pi\Delta k_B T}\exp(-\frac{\Delta}{T}) \\ N_T &= \frac{36\nu\Delta^2 T}{\omega_D^3}\exp\left(-\frac{2\Delta}{k_B T}\right), \end{aligned} \tag{24}$$

where $N(0)$ stands for density of states at the Fermi energy, Δ is the superconducting gap, ν refers to the number of atoms per unit cell and ω_D is the Debye energy.

1.6.1 Photoexcitation, initial carrier relaxation and probe process

In this subsection we first describe the photoexcitation, initial relaxation and probe process in the ultrafast pump-probe experiments. At the end, we introduce the temperature dependencies of the amplitudes and relaxation times of the photoinduced transients in the experiments performed on materials exhibiting a gap in the low energy excitation spectrum.

Before we go deeper into the photoinduced processes in the pump-probe experiments, let us remind ourselves to the quantum-mechanical description of optical absorption. The strength of the absorption process is determined by the quantum-mechanical probability for the transition rate of the system, changing from an initial electronic state i to a final electronic state f. The transitional probability $T_{i\to f}$ is determined by the Fermi golden rule [59]:

$$T_{i\to f} = \frac{2\pi}{\hbar}|\langle f|H'|i\rangle|^2\rho, \tag{25}$$

where $|\langle f|H'|i\rangle|$ is the matrix element of the perturbation H' between the final and initial states and ρ is the density of allowed final states.

In the pump-probe experiments, the pump pulse with 1.5 eV photon energy excites carriers from occupied states below E_F to unoccupied states in bands up to 1.5 eV above. Immediately afterwards[1], the initial electron-electron thermalization occurs with a characteristic time $\tau_{e-e} \sim \frac{\hbar E_F}{2\pi E^2}$, where E is the carrier energy measured from the Fermi energy E_F. In this thermalization process, quasiparticle avalanche multiplication due to electron-electron collisions takes place as long as τ_{e-e} is less than the electron-phonon relaxation time τ_{e-ph}. In the absence of gap in the density of states, the photoexcitation is followed by rapid carrier relaxation resulting in slightly elevated electron-phonon temperature. In contrast, when the gap with magnitude 2Δ is present in the low energy density of states, phonons with energies less than 2Δ cannot contribute to the relaxation of carriers just above the gap, therefore the situation is strongly modified and a bottleneck in the relaxation occurs. As a result, quasiparticles (QP's) accumulate near the gap, forming a nonequilibrium distribution. Since typical values of the energy gap in the high-T_c superconductors are of the order of $2\Delta \sim 30-50$ meV, each photon thus creates 30-40 QP's given by $E_{pump}/2\Delta$, where $E_{pump} = 1.5$ eV is the laser pump photon energy and 2Δ is the energy gap. Because the final relaxation step across the gap is strongly suppressed, the QP's together with high-frequency phonons $\hbar\omega > 2\Delta$) form a near-steady-state distribution. The QP recombination dynamics of this system is governed by the emission and reabsorption of the high-frequency phonons. Phonons with $\hbar\omega < 2\Delta$ do not participate in the direct relaxation of the QP's. Since the probe laser photon energy E_{probe} is typically well above the plasma frequency in high-T_c superconductors, we make the approximation that the transition probability for the probe light is given by Fermi's "golden rule" (see Eq.(25)) with photoinduced quasiparticles as initial states and with final unoccupied states well above the Fermi energy in a band that lies approximately at $E_0 \sim E_{probe}$.

For a weak perturbation, we can assume that photoinduced reflectivity (or transmission) is proportional to the photoinduced absorption [14, 60–62]. The measured photoinduced signal with the probe pulse is expressed as relative change of the reflected light intensity $\frac{\Delta R}{R} = \frac{R_{pump}-R_o}{R_o}$, where R_{pump} and R_o are reflected intensities with and without pump pulse, respectively. An analogous equation is also valid for the transmitted photoinduced signal. The photoinduced reflectivity (transmission) amplitude is weighted by the dipole matrix

[1] We can assume the process to be instantaneous since it is much faster in comparison with the duration of the pulse.

element and the joint density of states, so $\Delta R/R(\Delta T/T) \propto n_{pe}\rho_f|M_{ij}|^2$, where n_{pe} is the photoexcited carrier density, ρ_f is the final density of unoccupied states and M_{ij} is the dipole matrix element.

In the following we introduce the expressions for the T-dependence of the photoexcited carrier density n_{pe} and QP relaxation time τ_{ph}.

The T-dependence of the photoinduced carrier density n_{pe} in the presence of a temperature-dependent gap was analyzed by Kabanov *et al.* (Ref. [14]):

$$\Delta R/R \propto n_{pe} = \frac{\varepsilon_I/(\Delta(T)+k_{\mathrm{B}}T/2)}{1+\frac{2\nu}{N(0)\hbar\Omega_c}\sqrt{\frac{2k_{\mathrm{B}}T}{\pi\Delta(T)}}\exp[-\Delta(T)/k_{\mathrm{B}}T]}. \tag{26}$$

Here, n_{pe} is the photoexcited carrier density, ε_I is the energy density per unit cell deposited by the incident laser pulse, ν is the effective number of phonon modes per unit cell participating in the relaxation and Ω_c refers to phonon frequency cut off. The expression for the QP relaxation time τ_{ph} as a function of lattice temperature T and photoexcitation energy ε_I which is valid for temperatures $0 < T < T_{\mathrm{c}}$ is given by [14]:

$$\tau_{ph} = \frac{\hbar\omega^2\ln(1/(\varepsilon_I/2N(0)\Delta(0)^2+\exp[-\Delta(T)/k_{\mathrm{B}}T])}{12\Gamma_\omega\Delta(T)^2}, \tag{27}$$

where Γ represent the Raman phonon linewidth.

1.7 Kinetics in the metallic state

In the metallic state the photoexcited carriers first thermalize among themselves via electron-electron scattering with characteristic electron-electron relaxation time τ_{e-e}. Further energy relaxation occurs by electron-phonon relaxation time τ_{e-ph}. At the end, slower relaxation processes (such as heat diffusion) return the system to its initial temperature. A detailed study of the relaxation dynamics in systems provides important parameters of the electron-phonon interactions in the systems.

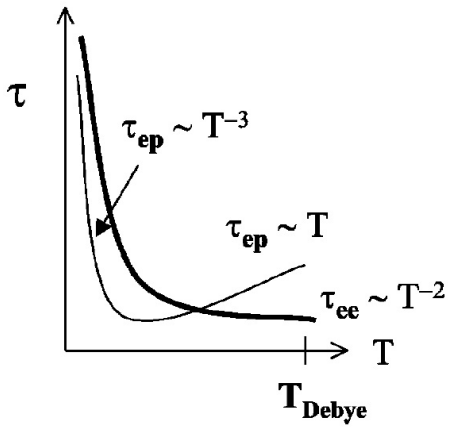


Figure 12: Temperature dependence of electron-electron τ_{ee} and electron-phonon τ_{ep} relaxation times as predicted by [63]. Please note that in the main text we denote electron-electron and electron-phonon relaxation times with τ_{e-e} and τ_{e-ph}, respectively.

The first theoretical model that will be presented is called the two-temperature model (TTM) [64]. This model was described by M. I. Kaganov, I. M. Lifshits and L. B. Tanatarov in 1956. The TTM assumes much faster relaxation within each system (e.g. electron system, phonon system) compared to the relaxation between these systems. According to this model, electrons and phonons are in thermal quasi-equilibrium with different time dependent temperatures: T_e and T_l. The temperature of each system can be defined during relaxation where the relaxation time between system 1 and system 2 is determined by their specific heats C_1 and C_2 and the energy-transfer rate per temperature difference $g(T)$ [64]:

$$\tau^{-1} = g(T)\left(\frac{1}{C_1} + \frac{1}{C_2}\right). \tag{28}$$

TTM predicts that at high temperature ($T > \frac{T_{Debye}}{5}$) τ_{e-ph} relaxation time is proportional to T, where at low temperature ($T < \frac{T_{Debye}}{5}$), the approximation $\tau_{e-ph} \sim T^{-3}$ is valid. It was shown [63] that at high temperatures, the electron system thermalizes faster than the lattice system, whereas at low temperature the *e-e* thermalization becomes slower than the *e-ph* relaxation. In addition, τ_{e-e} and τ_{e-ph} are comparable at low T and $\tau_{e-e} \sim T^{-2}$ (Fig. 12).

According to the TTM, τ_{e-ph} is longer than τ_{e-e}. This means that in the initial electron-electron thermalization process the electrons are decoupled from the lattice and the electronic system can be described with the electronic temperature T_e which differs from the lattice temperature T_l. Moreover, the heat capacity of the electron gas is much smaller than the heat capacity of the lattice, and consequently $T_e \gg T_l$. However it was shown that $\tau_{e-e} < \tau_{e-ph}$ assumption is incorrect on a femtosecond scale [65]. The characteristic *e-e* relaxation time τ_{e-e} is quite long due to the Pauli exclusion principle and it can be estimated by: $1/\tau_{e-e} \approx \pi^3 \mu_c^2 (k_B T_e)^2 / 4\hbar E_F$, where μ_c is the Coulomb pseudopotential characterising the electron-electron interaction. For example, $\tau_{e-e} \approx 1.4$ ps was determined experimentally in $La_{1.85}Sr_{0.15}CuO_4$ at 540 nm probe wavelength, 70 μJ/cm^2 pump fluence and $T = 300$ K [12].

The description in terms of the electron-phonon spectral Eliashberg function is given by Allen's model [66]. The strength of the *e-ph* interaction $\lambda\langle\omega^2\rangle$ can be expressed as [66]:

$$\lambda\langle\omega^2\rangle = 2\int_0^\infty \alpha^2F(\omega)\omega d\omega, \tag{29}$$

where $\alpha^2F(\omega)$ is electron-phonon spectral function or Eliashberg function.

Experimentally, the strength $\lambda\langle\omega^2\rangle$ of the *e-ph* interaction can be derived from the electron relaxation times τ [12]. According to TTM, the relaxation time τ_{e-ph} is expected to be proportional to T_e [64]:

$$\tau_{e-ph} = \frac{\pi k_B T_e}{3\hbar\lambda\langle\omega^2\rangle}. \tag{30}$$

Outside the TTM regime ($\tau_{e-e} > \tau_{e-ph}$) the relaxation time τ_{e-ph} is proportional to the lattice temperature T_l [65]:

$$\tau_{e-ph} = \frac{2\pi k_B T_l}{3\hbar\lambda\langle\omega^2\rangle}. \tag{31}$$

Besides the factor 2, a notable difference compared to the TTM formula (Eq.(30)) is that τ_{e-ph} is predicted to be linearly dependent on T_l (not T_e). Since the heat capacity of the lattice is much higher than that of electrons, in our experiments T_l is close to the cryostat temperature for all fluences.

At the end, it is useful to mention the relation for the relaxation time valid at low temperatures [65]:

$$\tau_{e-ph} = \frac{2\hbar\Theta_D}{\pi^3\lambda k_B T^2}, \tag{32}$$

where Θ_D stands for the Debye temperature.

From all above written formulas, we can see that femtosecond laser spectroscopy measurements allow us to measure accurately the electron-phonon relaxation time τ_{e-ph} and consequently estimate the value of the strength of the electron-phonon interaction λ. This is very important in order to reveal the high-T_c pairing mechanism.

1.8 Introducing the term of condensation energy

The condensation energy U_c can be thought of as the difference in energy between the normal and the superconducting state in a superconductor at $T = 0$ K [48]. In conventional metals the superconductivity has been understood to result from an effective attractive interaction between electrons. As a consequence, a reduction of the interaction energy occurs and the kinetic energy increases when the material becomes superconducting. For conventional superconductors, this phenomenon has been predicted by Bardeen-Cooper-Shrieffer theory [2]. The zero temperature energy difference between the normal state n and superconducting sc state is given by a BCS equation: $\langle E\rangle_{sc} - \langle E\rangle_n = -\frac{1}{2}N(0)\Delta^2(0)$. Here, $N(0)$ is density of states at the Fermi level and $\Delta(0)$ is the energy gap at $T = 0$ K.

Before we derive the equation for U_c, let us introduce the relation of how the entropy is related with the specific heat [67]:

$$S(T) = \int_0^T \frac{C(T')}{T} dT'. \tag{33}$$

If the temperature dependence of the specific heat is known in the superconducting and normal state, the free and internal energy differences can be calculated using the relations [67]:

$$F_n(T) - F_{sc}(T) = \int_T^\infty [S_n(T') - S_{sc}(T')] dT', \tag{34}$$

$$E_n(T) - E_{sc}(T) = \int_T^\infty [C_{sc}(T') - C_n(T')] dT', \tag{35}$$

where n and sc correspond to the normal and superconducting state, respectively. The integration limits ensure that $\lim_{T\to\infty} F_{sc}(T) = F_n(T)$ and $\lim_{T\to\infty} E_{sc}(T) = E_n(T)$ in accordance with the assumption that for $T \to \infty$ superconductivity vanishes. The condensation energy corresponds to the zero-temperature energy difference $U_c = E_n(0) - E_{sc}(0) = F_n(0) - F_{sc}(0)$. The condensation energy U_c can be obtained by integrating the entropy difference [67]:

$$U_c = \int_0^\infty [S_n(T) - S_{sc}(T)] dT. \tag{36}$$

One of the main challenges to theoretical attempts to understand the microscopic mechanism of high-T_c superconductivity is to account quantitatively for the superconducting condensation energy. Thus, a very fundamental test for any superconductivity model is, amongst other things, the correct prediction of the condensation energy. An accurate measurement of the condensation energy is therefore deemed essential test for theory. Unfortunately, there are very few experimental methods which can attempt measure the condensation energy. In principle, the condensation energy can be evaluated from the specific heat data measurements [68, 69] as $U_c^{\rm exp} = -\int_0^{T_c} dT \int_0^{T_c} \frac{\Delta C}{T} dT$. For the cuprates, this approach has been highly controversial due to the fact that the specific heat in the superconducting state can be measured well below T_c, whereas it is impossible to measure the normal state specific heat at low temperatures without destroying the condensate with a magnetic field. However, this might significantly alter the underlying state due to the high fields involved.

Similarly, with the use of Ni or Zn-doping to destroy the superconducting state, the normal state is apparently no longer the same. Alternatively, subtraction of an assumed normal state specific heat is performed with uncertainties. Furthermore, the thermodynamic estimate $G_n - G_s = H_c^2/8\pi$ (Eq.(9)), as pointed out by [70] - is unambiguously applicable only to a type-I superconductor, which makes it unusable for virtually all high-T_c superconductors.

The change of the kinetic energy on transition to the superconducting state can be estimated from the change of optical conductivity on transition to the superconducting state and the application of the Ferrell-Glover-Tinkham sum rule [71], and is applicable to models which are kinetic energy driven, but unfortunately it is model-dependent and does not include any information about the change in the potential energy.

1.9 Experimental measurement of the superconducting destruction energy

In the low-perturbation regime the linear increase of the excitation fluence is followed by a linear $\Delta R/R$ superconducting response. With further systematic increase of the power of the pump beam, we switch to the high-fluence perturbation regime. Here, a saturation of the superconducting condensate was observed when a certain laser fluence threshold $\mathscr{F}_{\mathrm{T}}$ is reached [13, 72]. The appearance of the plateau in the signal is related to the complete destruction of the superconducting state, *i.e.* the saturation is a fingerprint of the SC state destruction. To determine the destruction threshold fluence $\mathscr{F}_{\mathrm{T}}$ we use the inhomogeneous excitation model, described in detail in the following subsection. Before we calculate the destruction energy density, the optical constants as reflectivity R and light penetration depth λ_{op} should be determined.

The values for R reflectivity, optical conductivity $\sigma(\omega)$ and dielectric constant ε can be obtained from the optical studies [73]. The penetration depth λ_{op} can be evaluated from the absorption coefficient α [59]:

$$\alpha = \frac{4\pi k}{\lambda_{op}}, \tag{37}$$

where k is the extinction coefficient, defined as [59]:

$$k = \frac{1}{2}\left[\left(\varepsilon_1^2 + \left(\frac{4\pi\sigma_1}{\omega}\right)^2\right)^{1/2} - \varepsilon_1\right]^{1/2}. \tag{38}$$

In these equations, σ_1 and ε_1 are the real parts of the optical conductivity and dielectric constant, respectively. Since the inhomogeneous model is described in more detail in (Ref. [13]) here we will just summarize the main relations. In the low-excitation regime the linear dependence of $\Delta R/R$ response is expressed with [13]:

$$\frac{\Delta R}{\Delta R_s} = \frac{2\mathscr{F}_0\rho_{eff}^2}{3\mathscr{F}_T\rho_{pr}^2} = \frac{2}{3}f^{-1}(1+\overline{f}^{-2}). \tag{39}$$

On the other hand, for the high-fluence perturbation regime we have [13]:

$$\frac{\Delta R}{\Delta R_s} = \left(1 - f^2 + \frac{2(f\overline{\rho}^2 - f^2)}{\overline{\rho}^2 - 2} + \frac{6f\overline{f}^2/(1+\overline{\rho}^{-2}) - 2f^2\overline{\rho}^{-2}}{6 - 3\overline{\rho}^2}\right), \tag{40}$$

with $\rho_{eff}^2 = \frac{1}{\rho_{eff}^2} = \left(\frac{1}{\rho_{pu}^2} + \frac{1}{\rho_{pr}^2}\right)$ and $\overline{\rho}^2 = \rho_{pu}^2/\rho_{pr}^2$ where ρ_{pu} and ρ_{pr} are the pump and probe beam radii, respectively. $f = \frac{\mathscr{F}_T}{\mathscr{F}_0}$ where with $\mathscr{F}_0$ we denote the external fluence. ΔR_s is the saturated value. The value at which $\Delta R/R$ reaches $2\rho_{eff}^2/3\rho_{pr}^2$ of the maximum value of $\Delta R/R$ is equal to the value of the $\mathscr{F}_{\mathrm{T}}$ threshold fluence (Eq.39). Once we have determined the $\mathscr{F}_{\mathrm{T}}$ threshold fluence and optical constants, the destruction energy density U_d can be determined as [13]:

$$U_d = \frac{(1-R)\mathscr{F}_{\mathrm{T}}}{\lambda_{op}}. \tag{41}$$

1.10 Heating effects

A common problem that arises as a consequence of the laser illumination is heating of the sample [74–77]. While conducting an optical laser experiment, there is an additional energy brought to the system that causes heating of the sample. The heating effect must be taken into account for the data analysis. There are two types of sample heating effects: steady-state and transient heating.

Temperature increase due to absorption of the single laser pulse has a typical $1/\sqrt{t}$ temporal evolution. Before the next pulse is absorbed (~ 12 ns), the system does not completely thermally relax and therefore the temperature pile-up occurs, *i.e.* the probed volume has a higher temperature than the temperature of the cold finger located in the cryostat. The temperature drift caused by the average (high) laser illumination is referred to a steady-state heating. It is more pronounced in the measurements with high laser power and high repetition rates.

Taking into account that the thickness of the single crystal ($\sim 0.3-0.5$ mm) is much larger than the penetration depth (~ 30–100 nm) we can model the steady-state heating due to the pump laser beam with a simple steady-state heat diffusion model [75]. From this model we obtain temperature increase $\Delta T \sim 17$ K and 10 K in $YBa_2Cu_3O_{7-\delta}$ (at 80 K) and $La_{2-x}Sr_xCuO_4$ (at 5 K) at an average laser power 10 mW, respectively[2].

The temperature within the illuminated spot is non-uniform due to the Gaussian beam waist. Therefore, we should consider the effective temperature increase ΔT_{eff} (the average temperature increase sensed by the probe beam). The effective temperature increase ΔT_{eff} and the spread of temperatures within probed volume $\sigma^2_{\Delta T_{eff}}$ can be expressed as [78]:

$$\Delta T_{eff} = \frac{1}{K}\int_0^\infty \Delta T(r) I(r)\,\mathrm{d}r \tag{42}$$

and

$$\sigma^2_{\Delta T_{eff}} = \frac{1}{K}\int_0^\infty (\Delta T(r) - \Delta T_{eff})^2 I(r) r\,\mathrm{d}r, \tag{43}$$

where $K = \int_0^\infty I(r) r\mathrm{d}r$ and $I(r) \propto \exp(-2r^2/d^2)$ represent the spatial profile of the pump beam.

One way to minimize the heating effect in the high power experiments is to place additional optics to increase the pump beam waist. This would decrease $\sigma^2_{\Delta T_{eff}}$.

The steady-state heating can be measured with a four-point probe resistivity measurement of a thin microbridge made of the same superconducting material. Experimental data were found to be in a good agreement with the proposed heating model.

The temperature rise due to absorption of a single laser pulse is named transient heating. During the photoillumination, each pulse separately induces time-dependent temperature decay as $1/\sqrt{t}$. The transient increase in temperature ΔT_{tr} can be estimated in its simplest form as [78]:

$$\Delta T_{tr} = \frac{E_{pulse}}{mc_p}, \tag{44}$$

where E_{pulse} stands for the energy of a single pulse and m and c_p represent the mass of the illuminated volume and specific heat, respectively.

In the experiments where the high repetition rate lasers are used, the contribution of the transient heating is much less pronounced than the steady-state heating. However, the low repetition rate laser induces significant increase of the transient heating that should be properly taken into account.

[2] Please note that the heating strongly depends on the laser spot size. Presented data are an example for a laser beam diameter $d = 60$ μm.

2 Experimental

> "Start by doing what's *necessary*, then what's *possible*; and suddenly you are doing the *impossible*."
>
> Saint Francis of Assisi

This chapter is dedicated to experimental methods used in this thesis. It starts with a short explanation about how the samples were prepared for the optical experiments. Later on, after an introduction to generation of the ultrashort laser pulses, I focus on the pump-probe experimental technique. Here, I provide more detailed description of the pump-probe setup. At the end of this chapter, I discuss how the beam size was characterized.

2.1 Sample preparation and characterization

2.1.1 $YBa_2Cu_3O_{7-\delta}$ superconductor

The high-T_c superconductor $YBa_2Cu_3O_{7-\delta}$ was the first superconductor whose T_c exceeded the boiling temperature of liquid nitrogen [4]. Regarding the crystal structure, YBCO has two modifications [79]. The orthorhombic phase is observed at low temperatures $T \leq 500°C$ and oxygen concentrations $\delta \leq 0.6$. At higher temperatures, when the oxygen content starts to decrease and the disordering in Cu(1)-O(1) chains occurs, the tetragonal phase appears. The undoped $YBa_2Cu_3O_6$ is an insulator and by increasing the oxygen concentration in the Cu(1)-O(1) layers, the phase transition from the Fermi glass to a metallic-like phase occurs. When the oxygen deficiency is equal to $x = 0.07$ the material undergoes superconducting transition with maximum $T_c = 93$ K. With further increase of the hole doping YBCO becomes overdoped.

Single crystals of $YBa_2Cu_3O_{7-\delta}$ were prepared by X. Yao from Shanghai Jiao Tong University and grown in Y_2O_3 crucibles via conventional flux method [80]. The crystals were annealed at high temperatures ranging from a 400 to 900°C in the oxygen atmosphere for a certain time and then rapidly quench to room temperature. In order to prepare samples with a certain doping level, the annealing temperature and atmosphere were varied to best tune the oxygen content over a wide range [81]. In our case, the underdoped single crystals ($T_c = 60$ and 63 K) were annealed in O_2 atmosphere for 70–110 hours at 640–700°C. The superconducting sample with $T_c = 92$ K was annealed at 480°C, first in air for 100 hours and then for 24 hours in O_2 atmosphere. YBCO sample with $T_c = 83$ K was annealed in O_2 atmosphere at 515°C first for 90 hours and then once more for 54 hours. After annealing, the crystals were quenched to room temperature, by rapidly taking out of the oven. The critical temperatures were determined by measuring AC susceptibility for each sample (Fig. 13). For the purpose of the optical experiments, we cleaved the crystals by a razor (Fig. 14) and glued them with G.E. varnish low-temperature glue onto a copper holder. At the end, the holder was mounted in an optical liquid-He flow cryostat.

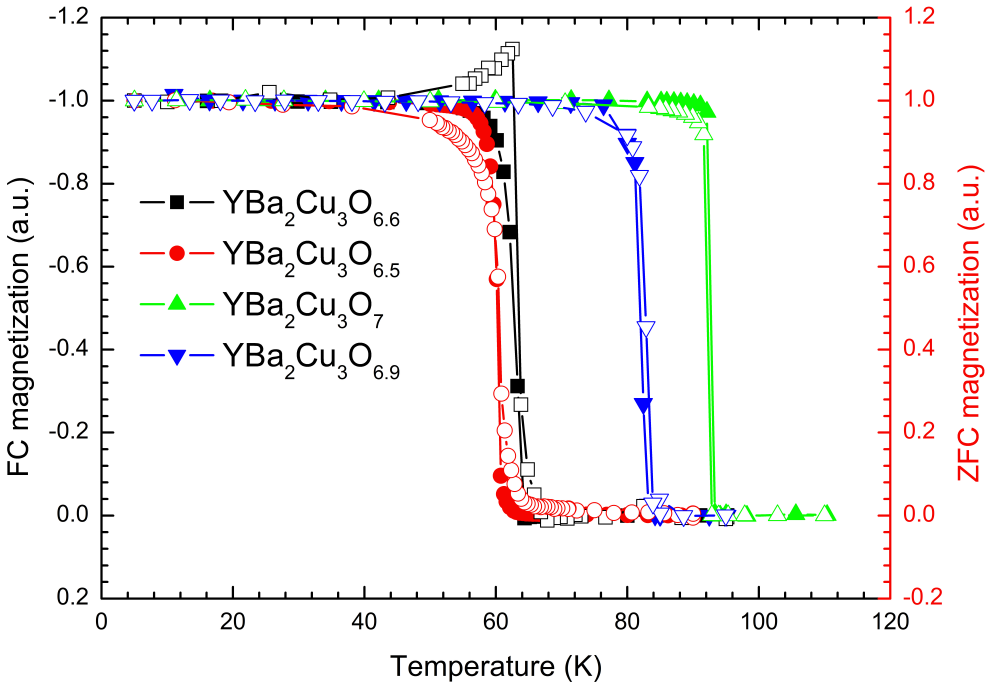


Figure 13: Normalized AC susceptibility data measured on annealed YBCO samples. Full symbols represent the susceptibility measurement in the field-cooled (FC) regime and the open symbols stand for the zero-field cooled (ZFC) cycle.

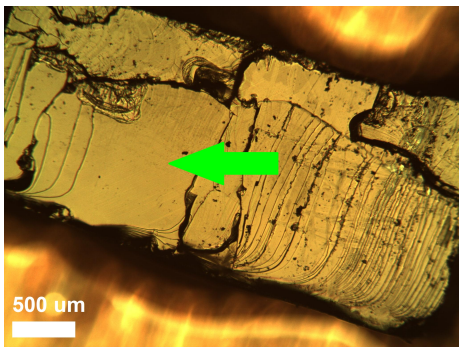


Figure 14: An example of the cleaved YBCO surface taken with an optical microscope. Experiments were performed on the area denoted by the green arrow.

2.1.2 $SmFeAsO_{1-x}F_x$, $SrFe_2As_2$ and $Ba(Fe,Co)_2As_2$ iron-pnictides

The optical experiments were performed on two different types of iron-based pnictides: the fluorine-doped $SmFeAsO_{1-x}F_x$ ("1111" system) and "122"-systems: $SrFe_2As_2$ and $Ba(Fe,Co)_2As_2$.

Single crystals of $SmFeAsO_{1-x}F_x$ were flux grown [82] at high pressure at the Laboratory for Solid State Physics in Zurich in the group of J. Karpinski. They were approximately 120×80 μm^2 in size and therefore they were glued on sapphire substrate, before mounting in the cryostat. We studied the undoped sample with $x = 0$ and SDW transition temperature at $T_{SDW} = 135$ K and structural transition at $T_s = 175$ K [39]. The near-optimally doped superconducting sample $SmFeAsO_{0.8}F_{0.2}$ had a critical temperature $T_c = 49.5$ K.

In contrast to $SmFeAsO_{1-x}F_x$ where we studied only the undoped and superconducting samples, for $Ba(Fe,Co)_2As_2$ we extend the study to a wide doping range. Single crystals of

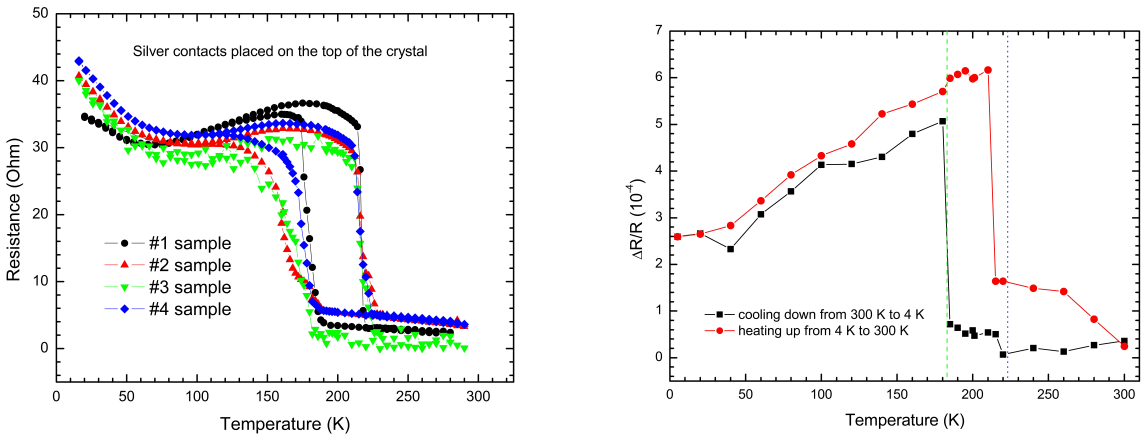
$Ba(Fe_{1-x}Co_x)_2As_2$ with Co-dopings, $x = 0$ %, 2.5 %, 5.1 %, 7 % and 11 % were grown from self-flux [83–85] in the group of I. R. Fisher from Stanford University. The samples with Co-0 % and Co-2.5 % show SDW ordering but not superconductivity, while Co-5.1% sample displays both a SDW and superconductivity at low T. The Co-7% and Co-11% samples refer to the near optimally doped ($T_c = 23$ K) and overdoped region of the phase diagram.

Undoped $SrFe_2As_2$ crystals exhibiting spin-density wave (SDW) ordering were prepared by self-flux method [86] in the group of Z. A. Xu from the Hangzhou University in China.

Similarly as for YBCO samples, the crystals were cleaved by a razor blade before mounting in the cryostat in order to get a fresh flat surface.

2.1.3 1T-TaS_2 charge-density wave system

Single crystals of 1T-TaS_2 were synthetized by P. Šutar via transport reaction synthesis. The TaS_2 powder, sulphur flakes, iodine, and tantalum foil were mixed and placed together in a glass ampoule. As a growth promotor and getter, we added a small amount (~ 0.02 g) of C_{60} fullerene. After vacuuming well below $\sim 10^{-5}$ mbar, the ampule was placed in a three-zone oven where the temperature was slowly increasing up to 900 ° C. After 12 hours, the temperature was set to 750 ° C for the next eight days. In order to get the 1T-polytype, we quenched the ampoule to room temperature, by rapid immersion of glass ampoules in cold water ($T \sim 20°$ C).



(a) (b)

Figure 15: (a) R(T) measurements on different 1T-TaS_2 samples, synthesized by P. Šutar. The experiments were performed with Keithley 6430 source unit and source current of 1 mA. Silver contacts were placed on the top of the crystal. (b) The temperature dependence of the raw $\Delta R/R$ transients amplitude in 1T-TaS_2 single crystals, synthesized by P. Šutar, taken at 11 μJcm^2 pump fluence. Dashed and dotted lines are an eyeguide for the CDW transitions upon cooling down and warming up, respectively.

The 1T polytype of TaS_2 is characterized by its shiny golden appearance in the visible light. An accurate way to distinguish the 1T polytype is to check the temperature dependence of the resistivity. For this purpose, we conducted resistivity measurements by four-point silver contacts fabricated onto a cleaved TaS_2 sample. The results are presented in Fig. 15 (a). In this way, we were able to prepare high-quality 1T-TaS_2 samples for the optical experiments. In order to prepare a fresh surface for optical experiments we cleaved the 1T-TaS_2 crystals by a scotch tape.

2.2 Femtosecond optical spectroscopy

The investigation of fast processes such as phonon and electron energy relaxation in solids or dynamics of biological and chemical reactions, requires a sufficient experimental time resolution. For a successful observation of these phenomena, the resolvable minimum time interval Δt must be shorter than the time scale of the process under investigation.

The discovery of the ultrashort lasers has led to a new era in the experimental spectroscopic techniques. Recent development in the generation of the ultrashort lasers, enabled performing experiments on the femtosecond time scales - the time scales of many phenomena in physics, chemistry and biology. In another words, the ultrafast laser spectroscopy allows us to "watch directly things happening on very short time scales".

Femtosecond laser spectroscopy has several advantages over standard spectroscopic techniques: *high time resolution* (down to 4 fs pulses in the visible and well below 1 fs in the far UV/soft X-ray spectral range have been reported), *high spatial resolution* (given by how tightly you can focus your beam), *high bandwidth* and *huge peak powers*. Femtosecond laser spectroscopy is suitable tool for many research areas. It can be applied for examination of structure and function of proteins in biochemistry [87], material characterization [88], medical applications as tomography [89] and optical imaging [90], fragmentation [91] (for example, of DNA into fragments that may be analyzed using mass spectroscopy), corrective eye surgery [92], dentisty [93] and many more.

Optical experiments described in this thesis were performed with a femtosecond laser spectroscopy system consisting of two main parts: a laser oscillator and an amplifier. As a source for 50 fs laser pulses we used Mira 900 mode-locked Ti:sapphire laser [94] with repetition rate of 88 MHz and energies up to 10 nJ per pulse, manufactured by Coherent Inc. The schematic of Mira is presented in Fig. 16, where the dashed line refers the auxiliary cavity (used only during initial alignment) and the solid line represents the main cavity.

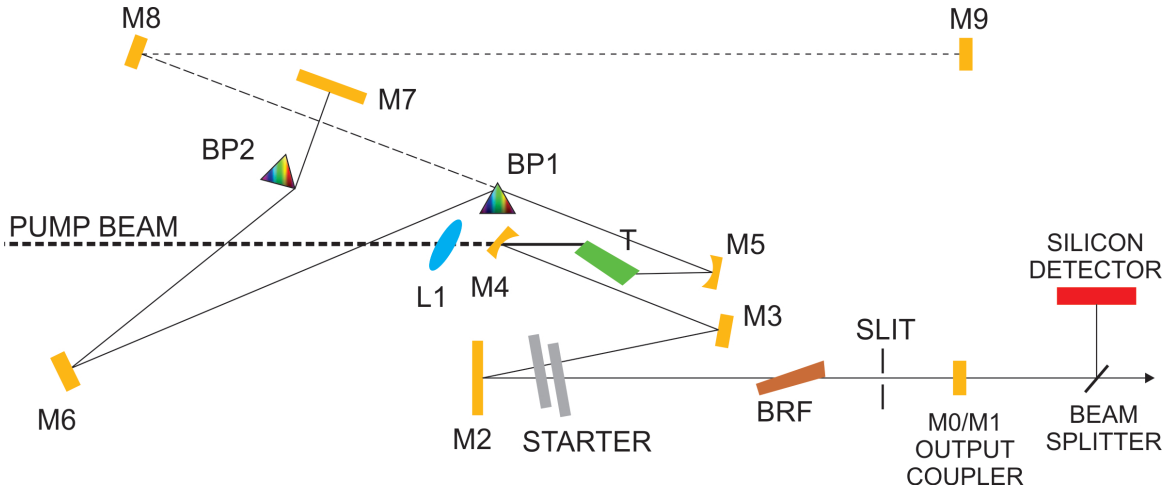


Figure 16: A Ti:Sapphire crystal (T) is pumped through the focusing lens L1 with a solid state diode-pumped laser. M1-M9: mirrors, BP1 and BP2: Brewster prisms and BRF:birefringent filter. Adopted from [94].

The central part of the laser oscillator is a Ti:Sapphire crystal which is pumped with a 5 W solid-state diode-pumped laser. It plays a role of a gain medium for generation of ultrashort laser pulses by means of Kerr lens mode-locking technique [95]. In order to start Kerr lens mode-locking, high power fluctuations need to be induced in the cavity. This can be done by changing the cavity length with the reflective starter. After the generation of the pulse, the beam goes to the birefringent filter (BRF) and to the output coupler. In this way, an ultrafast pulse train with 500 mW average power and pulse width of 120 fs is generated. Before amplification of the beam, there is an additional beam splitter at the

output, reflecting small amount of the beam to a silicon diode detector. The fast silicon diode is used for monitoring the pulsed/CW operation. The Mira output is tuneable from 740 to 1040 nm, but for optimum operation of the regenerative amplifier it is tuned to the peak of the Ti:Sapphire gain at 800 nm.

A pulse from the Mira oscillator is fed into a RegA 9050 regenerative amplifier [96], manufactured by Coherent Inc. (Fig. 17) The optical cavity has two focussed regions (beam waists): one for the Ti:Sapphire gain medium and the second for the acousto-optic cavity dumper (CD). There are two important elements in the RegA optical cavity. The first one is an acousto-optic modulator (Q-switch) used to prevent lasing in the RegA cavity until a pulse from Mira is injected. In this way, the Ti:Sapphire crystal can store enough energy for the amplification of the injected pulse. The Q-switch is made of a 30 mm thick TeO_2 crystal, matched to 80 MHz excitation. The second part is called cavity dumper. It is a high speed acousto-optic modulator used to inject and eject the single pulse amplified in RegA. Similarly as the Q-switch, it is made of a Brewster angled TeO_2 plate matched to respond to 380 MHz excitation.

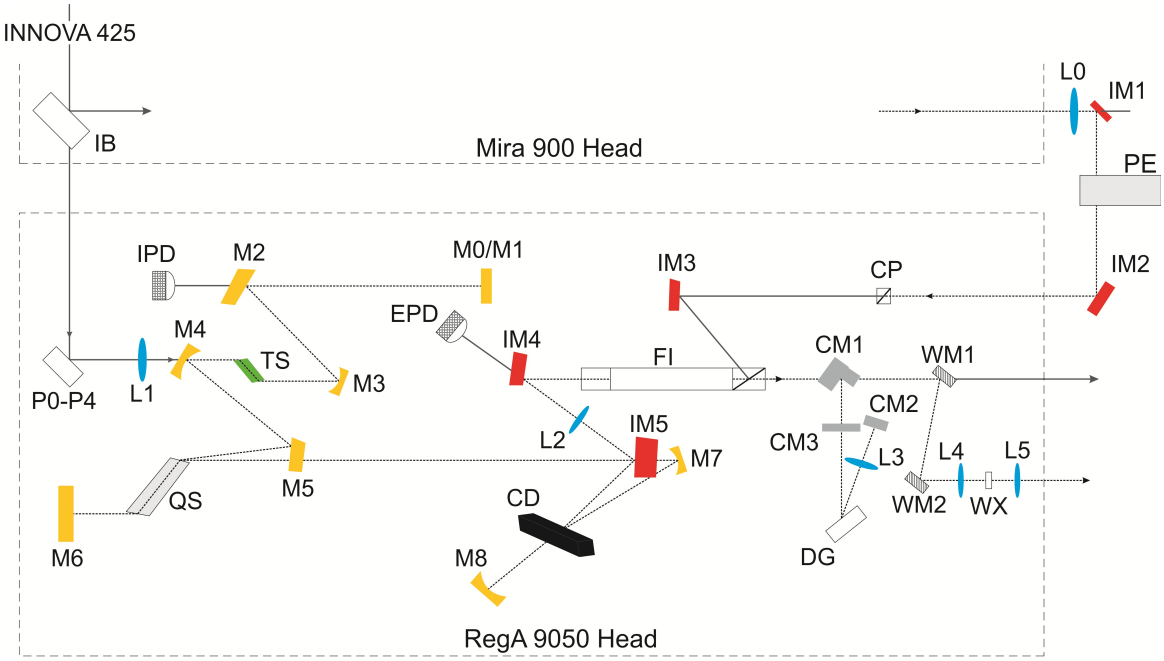


Figure 17: A schematic of the RegA regenerative amplifier used in experiments. IB:Ion Beamsplitter, IPD:Injection Photodiode, EPD:Ejection Photodiode, QS:Q-switch, CD:Cavity Dumper, FI:Faradey Isolator, CP:Cube Polarizer, DG:Diffraction Grating, WX;White light Crystal, M0-M8:Cavity Optics, IM1-IM5:Injection Optics, CM1-CM3:Compression Optics, WM1-WM2:Whitelight Optics, L0-L5:Lenses, P0-P4:Pump Optics, TS:Ti:sapphire Crystal, PE:pulse expander. Adopted from [96].

The input Mira beam passes through a Faraday insulator (used for the separation of the input Mira beam and output RegA beam without attenuation of the RegA or feedback into the Mira) and a single pulse is injected into the RegA via the cavity dumper. Amplification over 20 to 30 roundtrips allows to expand this pulse to 40 ps. The cavity dumper then extracts a exactly one single pulse which at 250 kHz repetition rate has 4 μJ energy. From the cavity dumper, the beam is returned to the Faraday insulator and separated from the input beam by a polarizer. At the output, the average power of the RegA pulse is 1 W. Before conducting the optical experiments, the RegA laser pulse passes through the pulse compressor where at the output the laser pulse has 50 fs pulse width (80 fs autocorrelation).

Since the laser system is placed in an air-conditioned laboratory, after its initial setup we do not need any additional adjustments for the stable daily operation. However, the main problem that dramatically reduces laser efficiency is the dust. Depending on the frequency

of the usage of the femtosecond laser system, it should be cleaned properly in order to maintain an optimum performance.

2.2.1 The pump-probe technique

The most commonly used technique for investigation of the ultrafast phenomena is the pump-probe technique (see Fig. 18). It is a two-step process in which the first intensive pulse named *pump*, excites the sample under investigation. In the second step, an attenuated and controllably time delayed pulse named *probe*, monitors the changes in the sample initiated by the pump pulse. Usually, but not always the pump and probe pulse are at the same wavelength. Depending on the process under investigation, they can also be derived from different synchronized lasers.

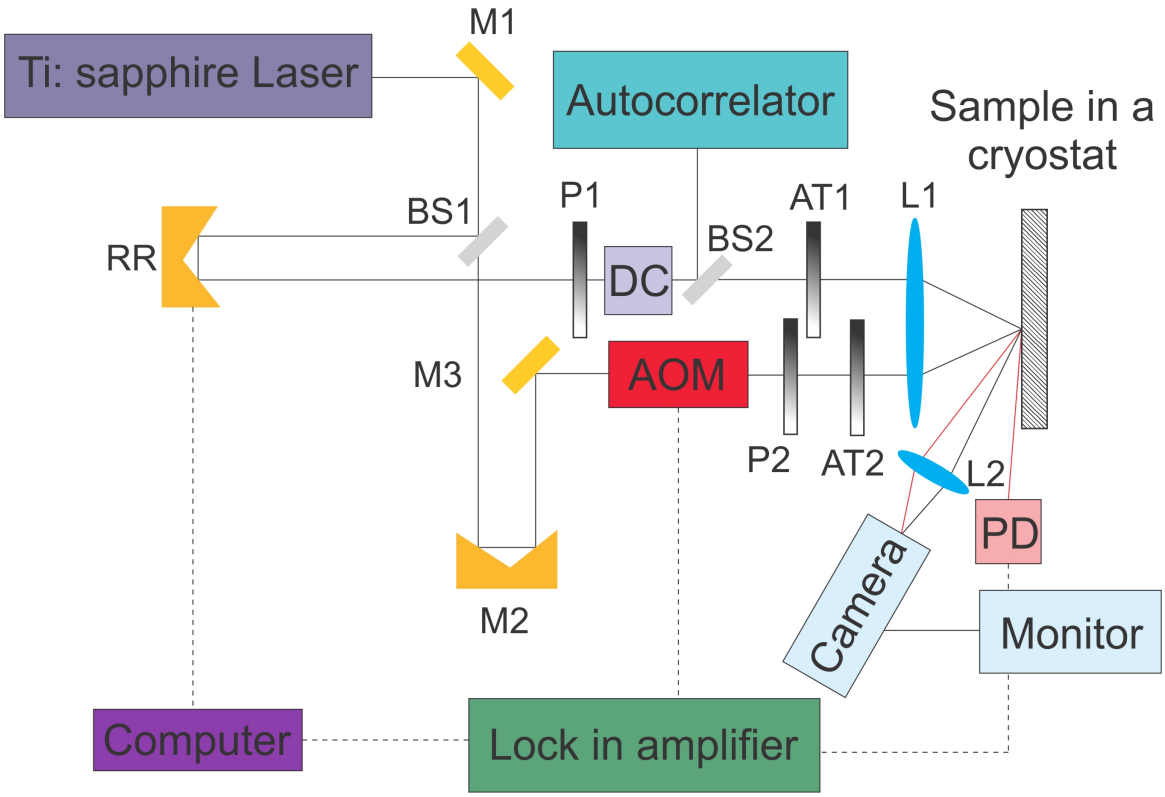


Figure 18: A schematic of the pump-probe technique. M1-M3:mirrors, RR:retroreflector, P1-P2:polarizers, BS1-BS2:beamsplitters, L1-L2:lenses, AT1-AT2:attenuators, AOM:acousto-optical modulator, PD:Photo diode and DC:dispersion compensator.

The pump pulse initiates some processes in the sample under investigation leading to the changes in the optical properties of the sample. The pump pulse destroys the equilibrium state by exciting the carriers from lower occupied states into higher unoccupied states. After the absorption of the pump laser photons the carrier relaxation process starts immediately including the carrier recombination and returning the system to its equilibrium state. When the probe pulse passes through the sample, it will be reflected and/or absorbed as a consequence of the photoinduced processes taking place in the sample. In other words the second pulse, provides a real-time observation of the dynamics of photoinduced processes.

The pump-probe technique is a powerful tool not only for real-time studies of the dynamics of photoinduced processes and determination of the lifetime of the excited state, but also for separation of different processes since it can distinguish between different excitations by their different relaxation dynamics, even if they are not well separated spectrally.

In our experiments, the pump and the probe beams were generated from a single beam using a beamsplitter (see Fig. 18). To delay the probe beam, we employ a moveable retrore-

flector that changes its optical path. The pump beam was modulated with an acousto-optical modulator or chopper at certain frequency. Both beams were perpendicularly polarized, and focused on the same spot on the sample. Depending on the nature of the problem, we were able to measure the change in the reflectivity/transmission as a function of the time delay.

Usually the photoinduced signals are small ($\Delta R/R \gtrsim 10^{-6}$) and comparable or smaller than the noise in the laser system. Therefore, in order to distinguish the signal and reduce the spectrally integrated noise from the lasers, the pump beam should be modulated at chosen frequency. The signal from the reflected/transmitted probe beam is detected with a lock-in amplifier that is phase locked to the pump modulation frequency. From the lock-in amplifier we can read out two signals: a signal modulated in phase of the given frequency modulation and a signal modulated at 90 deg out of the phase. Another practical issue which should be taken into account is related to the pump beam scattering that comes to the signal detector (photodiode). It can be minimized either by placing a polarizer in front of the detector or setting the pump and probe beams at different wavelengths. Moreover, the orientation/polarization of both beams relative to the crystal surface/axes is usually varied to obtain the maximum/minimum response at low temperature.

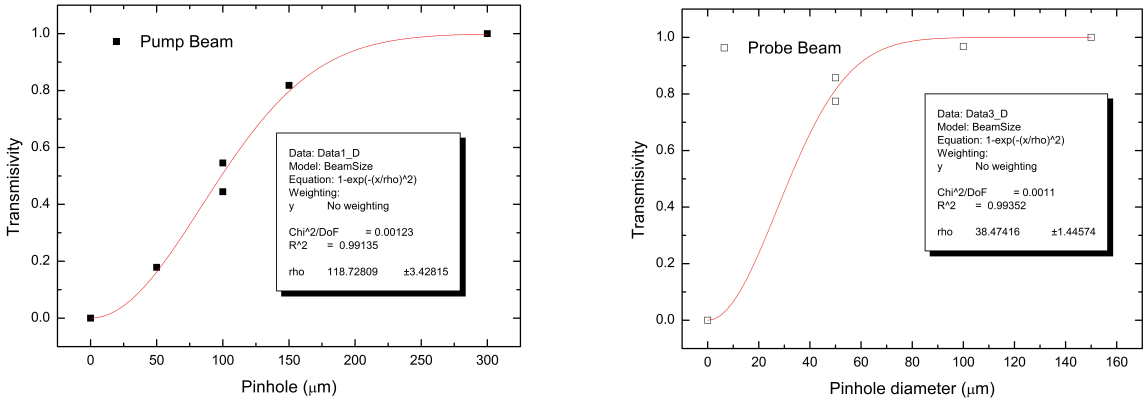
Unless otherwise noted, we used the pump photons at either 3.1 eV or 1.5 eV and probe photons at 1.5 eV phonon energy. The doubled photon energy of 3.1 eV was used to easily suppress the huge pump scattering by long-pass filtering in some delicate experiments.

2.3 Beam size determination

To estimate the waist of the Gaussian profile of the pump and probe beam, we place a pinhole with $2r_{pin}$ diameter at the focus of the both beams. We measure the beam power in front of the pinhole (P_{in}) and after the pinhole (P_{tr}). The diameter of the beam ρ can be easily determined with [13]:

$$\frac{P_{tr}}{P_{in}} = \frac{\int_0^{r_{pin}} \exp\left(-\frac{2r^2}{\rho^2}\right) 2\pi r \mathrm{d}r}{\int_0^{\infty} \exp\left(-\frac{2r^2}{\rho^2}\right) 2\pi r \mathrm{d}r}. \tag{45}$$

The light fluence penetrating into the sample is $\mathscr{F}_0$=(1-R)$\mathscr{F}_{pu}$ where $\mathscr{F}_{pu}$ refers to the laser fluence on the surface of the sample. To obtain the $\mathscr{F}_0$ we accounted for the light reflected from the cryostat CaF_2 window (0.08) and the part reflected from the sample (R).



(a) (b)

Figure 19: An example of the fit with Eq.(45) of measured transmissivity of the pump (a) and probe (b) beam. In this case, the diameters were estimated to be ~ 118 and ~ 40 μm for the pump and probe beam, respectively.

In the experiments presented in this thesis, the pump and probe beam diameters were measured with calibrated 50, 100 and 150 μm pinholes. Depending on the optimization of the focusing system in each experiment, the pump and probe beam diameters were 60–120 μm and 40–60 μm, respectively.

3 Study of the femtosecond relaxation dynamics in iron-based pnictides

> "My grandfather once told me that there were two kinds of people: those who *do the work* and those who *take the credit*. He told me to try to be in the first group; there was much less competition."
>
> Indira Gandhi

This chapter covers a systematic study of the relaxation dynamics in three different iron-based pnictides. Firstly, we present pump-probe experiments on undoped and near optimally doped SmFeAsO single crystals. The spin-density wave (SDW) ordering and superconducing state were studied as a function of temperature and pump fluence. Later on, we continue with the study of relaxation in the undoped $SrFe_2As_2$ single crystals. At the end, we focus our attention to the extensive study of the response in Co-doped $Ba(Fe,Co)_2As_2$ single crystals at different level of doping.

3.1 Femtosecond spectroscopy in $SmFeAsO_{1-x}F_x$ iron-pnictide superconductor

Discovery of the superconductivity in the iron-based pnictides [7] set up plenty of new challenges for the researchers worldwide. Even though, there have been significant experimental and theoretical attempts to reveal the puzzles related to their properties, we still have not been able to answer all open questions. Their similarities and differences compared with the cuprates have attracted the attention of the scientists worldwide in the past years. Contrary to the cuprate superconductors, where a single band with a high degree of correlations is believed to be sufficient starting point for the description of the electronic properties, there is a clear theoretical [97] and experimental [98] evidence that in pnictides there are several bands at the Fermi energy [99]. First optical experiments [100] in "122" and "1111" family of pnictides have shown the presence of the SDW gaps in the undoped samples and SC gaps in the SC samples. In addition, NMR experiments [101, 102] and point-contact Andreev spectroscopy [103] indicated a possible pseudogap. In contrast to the cuprates where the pseudogap is omnipresent, in the iron-based pnictides its omnipresence is still questionable. Similarly as in the cuprates, understanding the unusual normal state is important for explaining the mechanism leading to the superconductivity in iron-based pnictides.

Here, we present a femtosecond quasiparticle relaxation dynamics in undoped and near optimally doped $SmFeAsO_{1-x}F_x$ single crystals. A systematic temperature (T) and fluence ($\mathscr{F}$) dependent study will be presented. The aim of the presented work was to obtain a detailed information about the quasiparticle (QP) dynamics in the normal, SDW, and

superconducting states. The analysis on the experimental data will be divided into two subsections.

3.1.1 The undoped Sm-1111 sample

Undoped single crystals of SmFeAsO were prepared and characterized as it was described in detail in Chapter 2. Optical experiments were performed in reflectivity. To measure the $\Delta R/R$ photoinduced reflectivity change we used 50 fs laser pulses at $\hbar\omega_p = 3.1$ and $\hbar\omega_p = 1.5$ eV for the pump photons and $\hbar\omega_{pr} = 1.55$ eV for the probe photons. To avoid any coherent effects[3] the pump and the probe were perpendicularly polarized. The pump fluence was 0.58–174 μJ/cm^2 and 0.76–76 μJ/cm^2 for $\hbar\omega_p = 1.5$ eV and $\hbar\omega_p = 3.1$ eV, respectively. The ratio of pump and probe intensities was typically 100. Pump ρ_{pu} and probe ρ_{pr} diameters were accurately measured with calibrated pinholes and found to be $\rho_{pu} = 118\pm3$ μm and $\rho_{pr} = 38\pm1$ μm (Fig. 19).

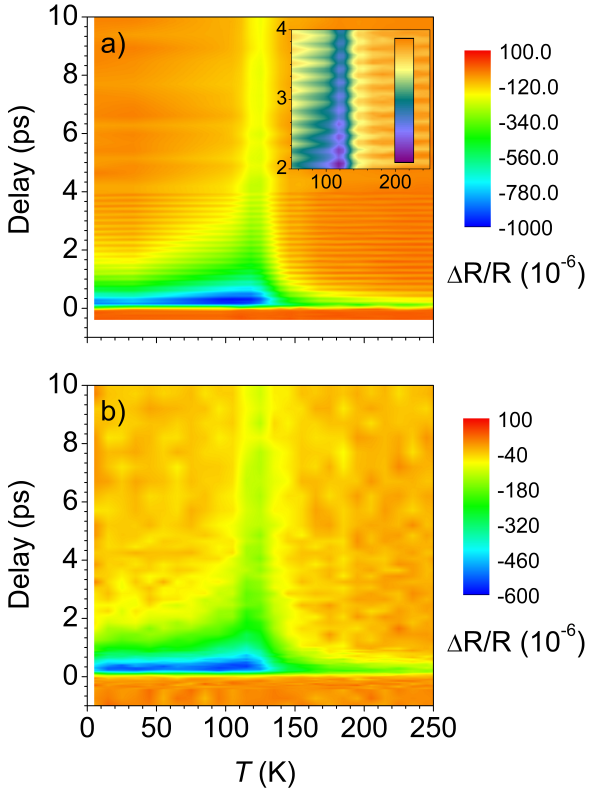


Figure 20: 2D temperature dependence plot of $\Delta R/R$ transients in undoped SmFeAsO, measured at 18 μJ/cm^2 (a) and 15 μJ/cm^2 (b) for the 1.55 eV and 3.1 eV pump photon energy, respectively. A coherent phonon with $f = 5.1$ THz is presented in the inset.

To study the temperature dependence of the relaxation dynamics we performed measurements at low excitation pump fluence at 18 μJ/cm^2 ($\hbar\omega_p = 1.55$ eV) and 15 μJ/cm^2 ($\hbar\omega_p = 3.1$ eV) in the temperature range 4–300 K. A temperature study on the $\Delta R/R$ transients is shown in Fig. 20. The response at different pump-photon energies is quite similar in both cases and the only noticeable difference of the response is the presence of a coherent phonon oscillation with the frequency 5.1 THz (170 cm^{-1}) at 295 K, at $\hbar\omega_p = 1.55$ eV, which is absent at $\hbar\omega_p = 3.1$ eV, consistent with Raman data [104].

[3]These effects arise from coherent interactions between the pump and the probe beam. The interference between both beams creates a grating in the sample which can diffract light from the pump into the probe beam or vise versa, thus contributing to the signal.

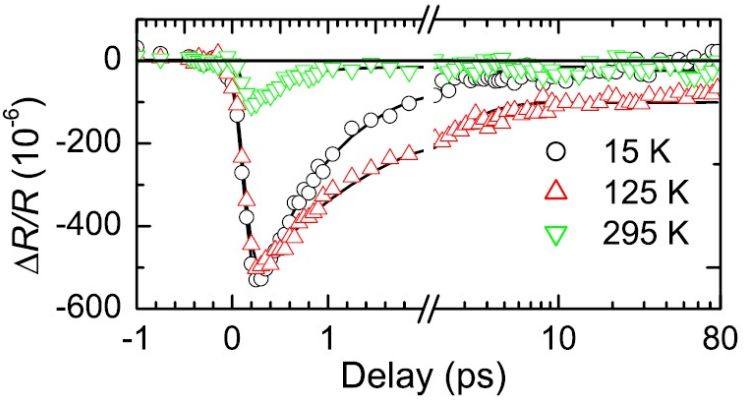


Figure 21: Raw $\Delta R/R$ transients in undoped SmFeAsO measured at 3.1 eV pump photon energy and 15 μJ/cm^2 fluence. Thin lines are single exponential decay fits of the data.

The amplitude of the transients increases with decreasing temperature, where at $T_{\mathrm{SDW}} =$ 125 K an additional long-lived response appears with decay time beyond our measurement delay range. The amplitude of $\Delta R/R$ achieves maximum at 115 K, upon entering the SDW state (see Fig. 22). With further decrease in the temperature the amplitude slightly drops at first and then remains constant below 50 K. At high temperatures, the $\Delta R/R$ transient can be described with a negative-amplitude single-exponential relaxation with a temperature-independent rise time of ~ 180 fs (Fig. 21). Below 200 K the relaxation time τ starts to increase where simultaneously with the maximum of the amplitude τ shows a remarkable divergentlike peak at ~ 120 K and then drops to a temperature independent value of 0.8 ps below 50 K (Fig. 22).

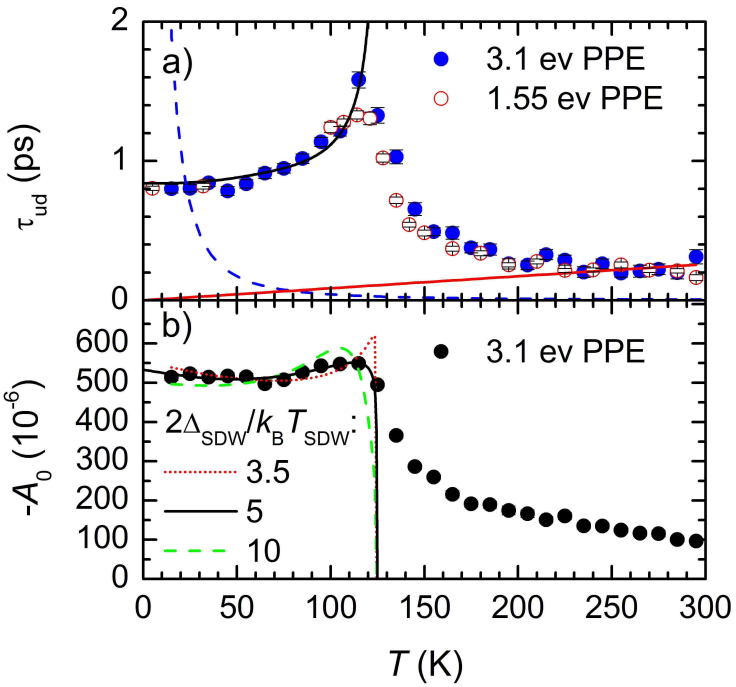


Figure 22: (a) Temperature dependence of the relaxation time in undoped SmFeAsO at 3.1 eV (blue circles) and 1.55 eV (red circles) pump photon energy. The red solid line is fit of Eq.(31). Blue dashed line is Eq.(32) with $\lambda = 0.2$ and $\Theta_{\mathrm{D}} = 175$ K. The black solid line is a fit of Eq.(27). (b) Temperature dependence of the $\Delta R/R$ amplitude. Thin lines represent the fits of the Eq.(26), discussed in the text with different magnitudes of the gap.

The rise and decay times are virtually independent of $\mathscr{F}$ pump fluence (Fig. 23).

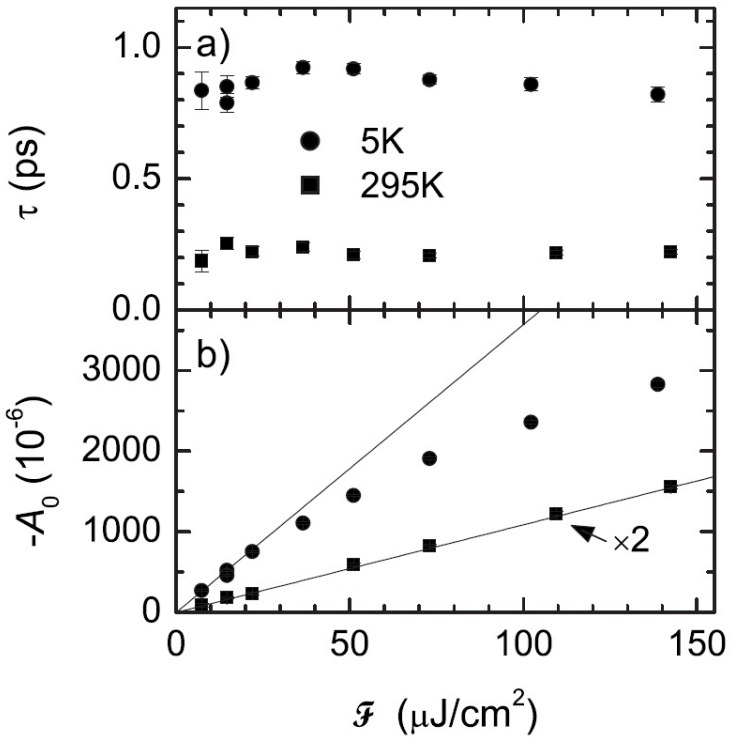


Figure 23: Fluence dependence of the relaxation time (a) and $\Delta R/R$ amplitudes (b) at 5 K (black circles) and 295 K (black squares) measured at 3.1 eV pump fluence in undoped SmFeAsO. The thin lines in (b) are linear extrapolations of the low fluence data.

On cooling down, undoped LaFeAsO (the most studied material in the X-1111, X=Rare Earth element pnictides group) undergoes a sequence of a structural transition from a tetragonal to orthorhombic symmetry at $T_s = 156$ K and a magnetic SDW transition at $T_{SDW} = 138$ K [105]. In SmFeAsO the SDW transition was reported at $T_{SDW} \sim 135$ K (Ref. [106]) while the structural transition was reported at lower temperature $T_s = 130$ K [107]. However, Martinelli *et al* [39] by using high resolution synchrotron powder diffraction have determined the temperature of structural transition to be $T_s = 175$ K. So far due to a possible different oxygen deficiencies in the two experiments and strong doping dependence of both T_{SDW} and T_s it was not possible to reliably distinguish between T_{SDW} and T_s in SmFeAsO. Our data show a marked critical slowing down at 125 K (see Fig. 20) in the form of the longlived relaxation tail, while the initial picosecond exponential decay time shows a maximum at ~ 115 K. Since the longlived relaxation tail affects the quality of the single exponential picosecond fit (see Fig. 21) we cannot reliably identify 115 K as a separate transition temperature. We are therefore unable to differentiate between structural and spin transitions so we will only refer to a single transition temperature $T_{SDW} = 125$ K in our data. From our data T_{SDW} is lower than reported in literature [106, 108]. Due to a variable thermal coupling to the sapphire substrate for such small crystals a small decrease in T_{SDW} originating from the oxygen deficiency cannot be distinguished from an apparent decrease in T_{SDW} due to the laser heating in our samples. Possible explanation for the appearance of the anomaly in the response at $T = 115$ K is slightly doping of our sample. From the previously published phase diagram [106] for $SmFeAsO_{1-x}F_x$ where it is assumed that $T_s = T_N$ for all dopings $x \leq 0.040$, we can see that for finite dopings $x \leq 0.040$ $T_s = T_N \sim 115$ K. This value suits our experimental observation and it is smaller than the reported value for the undoped samples, $T_s = T_N \sim 125$ K.

3.1.1.1 Gap in the SDW state

As we have mentioned before, below T_{SDW} a gap opens at the Fermi surface introducing a bottleneck in the relaxation [109].

The relaxation across a temperature-dependent gap was analyzed by Kabanov *et al.* (Ref. [14]). To fit the amplitude $\Delta R/R$ below T_{SDW} we use the equation (26) and from the fit, for a single SDW gap with BCS temperature dependence we get $2\Delta_{SDW}/k_B T_{SDW} \simeq 5$ (see Fig. 22(b)). Equation (27) for the relaxation time from [14] with the same $\Delta_{SDW}(T)$ describes well also the temperature dependence of the relaxation time (see Fig. 22(b)). However, Eq. (27) from [14] also predicts a fast decrease in the relaxation time with $\mathscr{F}$, which is not observed in our data (Fig. 23). The reason for this might originate in the fact that the SDW state is not fully gaped and the energy relaxation is not limited by the anharmonic energy transfer from the high-frequency to the low-frequency phonons as assumed in the derivation.

3.1.1.2 Relaxation dynamics at the room temperature

At the room temperature undoped pnictides are bad metals with resistivities in the milliohm centimeter range [110, 111] and plasma frequency in an ~ 1 eV range [100, 110]. Therefore, at temperature above T_{SDW} the $\Delta R/R$ transients are attributed to the relaxation of hot electrons in the states near the Fermi energy E_F. The magnitude of the $\Delta R/R$ due to the hot electrons relaxation in a metal strongly depends on the particle-hole asymmetry near the Fermi energy and might vary strongly among different materials. We analyze the $\Delta R/R$ transients at high T in the framework of the recent theoretical results on electron relaxation in metals [65], using Eq.(31) and Eq.(32). The relaxation time τ above T_{SDW} was determined from fitting the initial part of $\Delta R/R$ transient with a finite-rise-time single exponential decay (Fig. 22(a)). From the fit we obtain $\lambda\langle\omega^2\rangle = 135 \pm 10$ meV^2. If we estimate $\langle\omega^2\rangle \approx 252$ meV^2 from inelastic neutron data [112] we obtain $\lambda \approx 0.2$ indicating a rather weak electron-phonon coupling, which cannot explain high-T_c in the doped compound within a single-band BCS model. To check the consistency of the resulting value of λ we plot in Fig. 22(a) also the low-T result (Eq.(32)) indicating validity of the high-T approximation (Eq.(31)) above 230 K.

3.1.2 The superconducting Sm-1111 sample

Contrary to the undoped Sm-1111 sample, the reflectivity transients $\Delta R/R$ of superconducting $SmFeAsO_{0.8}F_{0.2}$ show complex time and temperature dependencies. The temperature dependence of $\Delta R/R$ was studied with the excitation pump fluence at 15 μJ/cm^2 ($\hbar\omega_p = 1.55$ eV) and 17 μJ/cm^2 ($\hbar\omega_p = 3.1$ eV) in the temperature range 4–300 K. From 2D plot presented in Fig. 24, we can distinguish three T regions. Firstly, at high temperatures, a negative transient is observed with initial 0.25 ps decay followed by a slower response consisting from a weak peak at 12 ps (see Fig. 25 (a)) at pump energy $\hbar\omega_p = 3.1$ eV. The transients scale linearly with increasing fluence except in the region of the initial 0.25 ps decay where a weak $\mathscr{F}$ dependence is observed at low $\mathscr{F}$. At $\hbar\omega_p = 3.1$ eV the transients have the same shape and similar amplitude as in undoped SmFeAsO without the coherent phonon. At $\hbar\omega_p = 1.55$ eV the negative high-T transients are much weaker than at $\hbar\omega_p = 3.1$ eV so only the initial 0.25 ps decay is resolved from the noise (see Fig. 26). In addition, a coherent phonon is observed with a softer frequency than in undoped SmFeAsO of 4.6 THz (153 cm^{-1}) having similar amplitudes at both pump energies.

In the temperature region at intermediate temperatures above T_c and low $\mathscr{F}$, the transients are positive on the subpicosecond time scale cross zero around 4 ps with the slow dynamics similar to the high-temperature one. At high $\mathscr{F}$ the positive part of the transients vanishes and the transients become qualitatively identical to those at higher temperatures

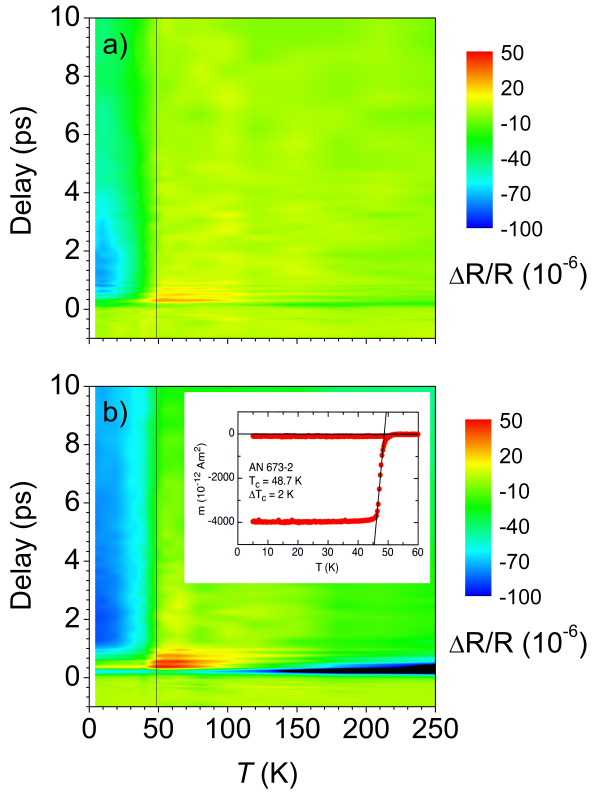


Figure 24: 2D temperature dependence plot of $\Delta R/R$ transients in superconducting $SmFeAsO_{0.8}F_{0.2}$, measured at 15 μJ/cm^2 (a) and 17 μJ/cm^2 (b) for the 1.55 eV and 3.1 eV pump photon energy, respectively. AC susceptibility is shown in the inset.

(see Fig. 25). The only remaining difference is a delay-independent positive vertical shift of the intermediate T scans with respect to those measured at 250 K and an increased coherent phonon frequency of 5.1 THz (170 cm^{-1}). At $\hbar\omega_p = 1.55$ eV transients are, as at higher temperatures, similar to the $\hbar\omega_p = 3.1$ eV transients, but weaker.

In the third T region, below T_c, an additional negative component appears with a rise time of 0.2–0.6 ps, depending on the pump energy and pump fluence, and decay time of ~ 5 ps. The component has a similar amplitude at both pump energies. At high $\mathscr{F}$ the additional negative component becomes undetectable due to a saturation and the transients become virtually identical to those measured at 55 K including the coherent phonon response.

3.1.2.1 Decomposition of the $\Delta R/R$ transients in superconducting $SmFeAsO_{0.8}F_{0.2}$ into components

While the transients in the undoped sample show a simple single-exponential relaxation the transients in the doped sample show a clear multicomponent relaxation. To separate contributions from different components we first use the fluence dependence of the reflectivity transients [15, 113]. The contributions from the relaxation processes corresponding to the normal state are expected to scale linearly with $\mathscr{F}$ because the perturbation of a few hundred microjoule per square centimeter is weak for the normal state. On the other hand, the low T-ordered states are more fragile and can be destroyed by a significantly weaker external perturbation resulting in the saturation with increasing $\mathscr{F}$. It turns out that the data can be consistently described by three distinct components A, B, and C, which are tightly connected with the three observed temperature regions. The temperature-independent linear

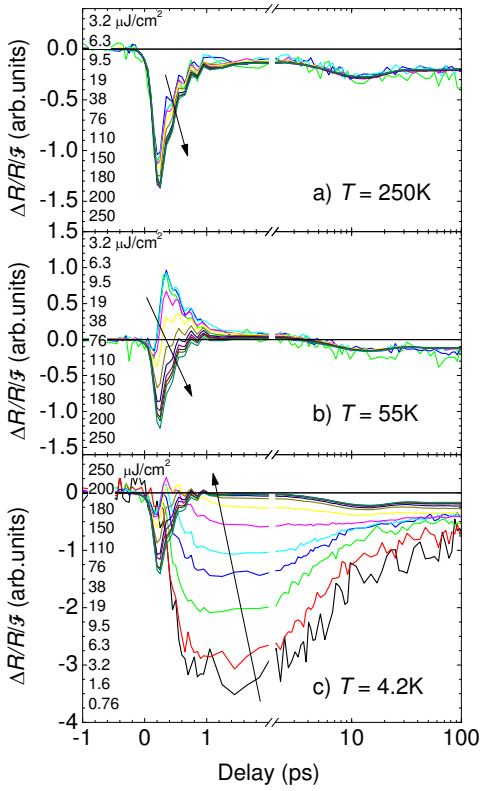


Figure 25: Fluence dependence of normalized $\Delta R/R$ transients measured at different temperatures and 3.1 eV pump photon energy. The arrow indicates the direction of increasing $\mathscr{F}$.

scaling of the transients with $\mathscr{F}$ above 150 μJ/cm^2 suggests the decomposition of the raw $\Delta R/R$ into component A which scales linearly with fluence and a *residue* composed from components B and C which saturate at finite $\mathscr{F}$ (see Fig. 27).

Component A dominates at high temperatures and has to originate in at least three distinct relaxation processes due to the relatively complex time evolution. (i) The slower dynamics, which is virtually the same as in undoped SmFeAsO at high temperatures (see Fig. 26), could be attributed to the band renormalization due to the lattice expansion. (ii) The subpicosecond decay, also having a similar decay time as in undoped SmFeAsO at high temperatures, will be discussed in more detail below. (iii) The oscillatory part of component A is attributed to a coherent phonon oscillation which appears softer as in undoped SmFeAsO. Except for the shift of the coherent phonon frequency all show only a minor T dependence. The *residue* shows a single-exponential decay (see Fig. 26) above T_c, which we name component B. Component B dominates in the raw transients in the intermediate temperature range, above T_c. Below T_c the *residue* changes to a multiexponential decay with the sign change, evidently due to the appearance of an additional relaxation process associated with the superconducting state named component C. Component C saturates at lower $\mathscr{F} \approx 10$ μJ/cm^2 than component B, which saturates above ~ 70 μJ/cm^2. The separation of component C from components A and B is further supported by comparison of the raw $\Delta R/R$ at different pump energy shown in Fig. 26 where components A and B show much smaller amplitudes at $\hbar\omega_p = 1.55$ eV in comparison to $\hbar\omega_p = 3.1$ eV, while the amplitude of component C shows a negligible pump energy dependence. Above T_c we fit the *residue* with a single-exponential decay component B [114] (see Fig. 28):

$$\frac{\Delta R_B}{R} = \frac{A_B}{2} e^{-(t-t_0)/\tau_B} \mathrm{erfc}\left(\frac{\sigma^2 - 4(t-t_0)\tau_B}{2\sqrt{2}\sigma\tau_B}\right). \tag{46}$$

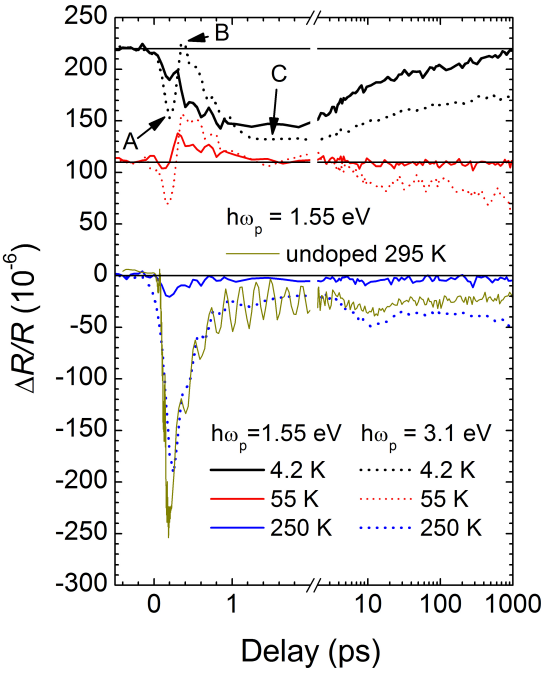


Figure 26: Reflectivity $\Delta R/R$ transients at 1.55 eV (full lines) and 3.1 eV (dotted lines) pump photon energy, measured at 4.2, 55 and 250 K. For the comparison the data for the undoped SmFeAsO at T=295 K is shown. Three different components A, B and C discussed in the text are shown in the upper figure.

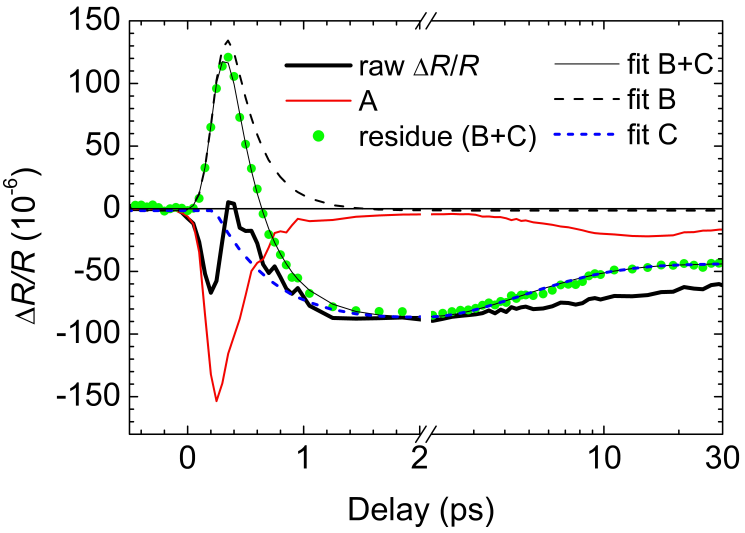


Figure 27: Decomposition of $\Delta R/R$ transients into three different components in the superconducting $SmFeAsO_{0.8}F_{0.2}$ sample.

Here, σ refers to the effective width of the excitation pulse with a Gaussian temporal profile arriving at t_0 and τ_B the exponential relaxation time. Below T_c an additional exponential

decays representing component C are needed to fit the *residue*:

$$\frac{\Delta R_{\rm C}}{R} = A_{1\rm C}(e^{-(t-t_0)/\tau_{1\rm C}} - e^{-(t-t_0)/\tau_{r\rm C}}) + A_{2\rm C}(e^{-(t-t_0)/\tau_{2\rm C}} - e^{-(t-t_0)/\tau_{r\rm C}}), \tag{47}$$

where $\tau_{r\rm C}$ stands for the rise time and $\tau_{i\rm C}$ are the decay times.

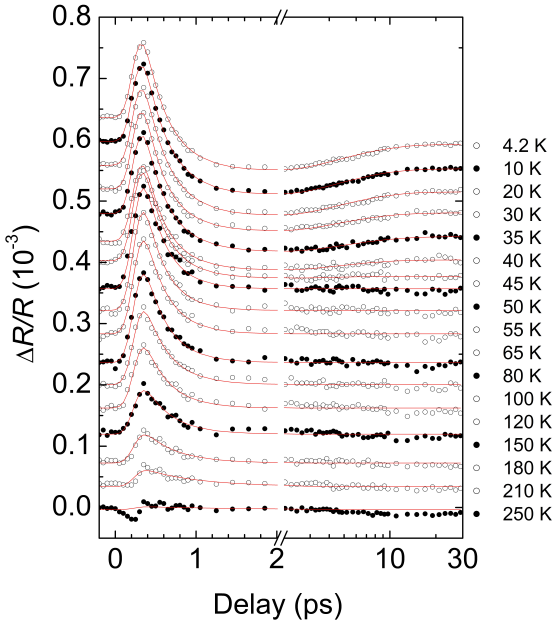


Figure 28: $\Delta R/R$ transients with component A subtracted, taken at different temperatures. Thin lines are single exponential decay fits of Eq. (46) above $T_{\rm c}$ and a multiexponential decay fits (a sum of Eq.(46) and Eq.(47) below $T_{\rm c}$.

From the fit we get for the decay time $\tau_{1\rm B} \approx 0.25$ ps at 4 K which slightly increases with increasing the temperature below 200 K. Above 200 K, where artifacts due to subtraction of component A start to be significant, $\tau_{1\rm B}$ steeply increases toward 1 ps. In addition, the amplitude of component B, $A_{\rm B}$, stays almost constant up to ~ 70 K and then drops monotonically.

For easier separation of component C associated with the superconducting response we use the fact that components A and B are temperature independent in the superconducting state. We therefore extract component C, without relying on the fluence dependence, by subtracting the average of the transients measured at 55 and 65 K from transients measured below 55 K. The subtraction gives the same results as the decomposition based on the fluence dependence. Component C clearly shows a two-step decay with a finite rise time and are excellently fit by Eq.(47) as shown in Fig. 29.

In the spirit of the Rotwarf-Taylor model [57] we associate the rise time with establishment of the thermal quasi-equilibrium between the photoexcited quasiparticles and high frequency ($\hbar\omega > 2\Delta_{\rm SC}$) phonons. The shorter relaxation time is associated with establishment of the local thermal equilibrium between all degrees of freedom, while the longer relaxation time is due to energy escape out of the probed volume. This is supported by increased relative amplitude of the long decay with respect to the total amplitude at higher $\mathscr{F}$. Neither the rise time nor the relaxation times (see Fig. 30) shows any temperature dependence within experimental error while only $\tau_{r\rm C}$ shows dependence on $\mathscr{F}$ and $\hbar\omega_{\rm p}$. At $\hbar\omega_{\rm p} = 1.55$ eV $\tau_{r\rm C}$ is faster and shows much weaker $\mathscr{F}$ dependence than at $\hbar\omega_{\rm p} = 3.1$ eV. At $\hbar\omega_{\rm p} = 3.1$ eV $\tau_{r\rm C}$ increases from 0.3 ps at $\mathscr{F} = 3$ μJ/cm^2 to 0.6 ps at $\mathscr{F} = 15$ μJ/cm^2. While an increase in $\tau_{r\rm C}$ with increasing $\hbar\omega_{\rm p}$ is expected due to the photoexcitation being farther away from $E_{\rm F}$ the $\mathscr{F}$-dependence with increasing $\hbar\omega_{\rm p}$ is not completely understood.

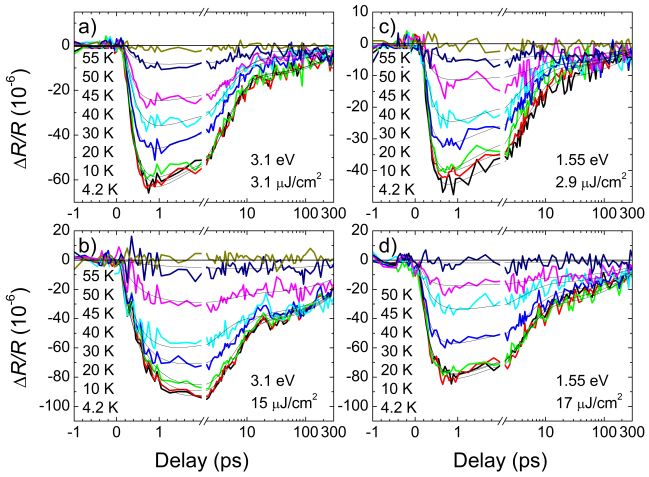


Figure 29: Temperature dependence of the superconducting component C in the low-excitation pump regime (a,c) and high-excitation pump regime (b,d) at 3.1 and 1.55 eV pump photon energy. Thin lines are fits with Eq.(47).

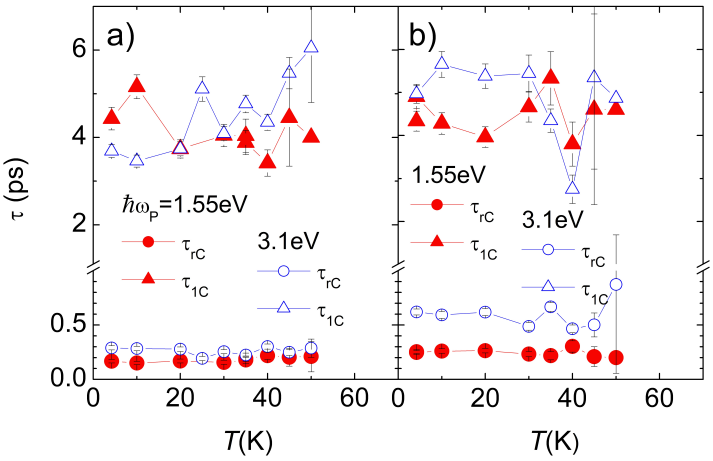


Figure 30: Temperature dependence of the rise time (circles) and relaxation time (triangles) at (a) 2.9 μJ/cm^2 (1.55 eV) and 3 μJ/cm^2 (3.1 eV) and (b) 17.4 μJ/cm^2 (1.55 eV) and 15 μJ/cm^2 (3.1 eV).

3.1.2.2 Experimental determination of the superconducting destruction energy

Similarly to previous reports [13] a saturation of the SC component was observed when a certain pump fluence threshold $\mathscr{F}_{\mathrm{T}}$ is reached (see Fig. 31). The optical penetration depth was found to be $\lambda_{op} = 31 \pm 15$nm in the near optimally doped Sm-1111 sample. Taking into account the optical penetration depth and reflectivity of $LaAsFeO_{1-x}F_x$ [73] we determine the energy density U_d required to completely destroy the superconducting state as: $\frac{U_d}{k_{\mathrm{B}}} = \frac{\mathscr{F}_{\mathrm{T}}(1-R)}{\lambda_{\mathrm{op}} k_{\mathrm{B}}} = 2.2$ K/Fe ($U_d = 18$ J/mol) at $\hbar\omega_{\mathrm{p}} = 3.1$ eV and $\frac{U_d}{k_{\mathrm{B}}} = 1.5$ K/Fe ($U_d = 12$ J/mol) at $\hbar\omega_{\mathrm{p}} = 1.55$ eV.

The magnitude of the superconducting gap was estimated from the fit of the temperature dependence of $\Delta R/R$ transients above $\mathscr{F}_{\mathrm{T}}$ by the high-frequency limit of the Mattis-Bardeen formula [115]:

$$\frac{\Delta R}{R} \propto \left(\frac{\Delta(T)}{\hbar\omega_{pr}}\right)^2 \log\left(\frac{3.3\hbar\omega_{pr}}{\Delta(T)}\right). \tag{48}$$

Here, $\hbar\omega_{pr}$ represents the probe photon energy and $\Delta(T)$ is the magnitude of the superconducting gap. In Fig. 32 we obtain good fit to the observed temperature dependence by

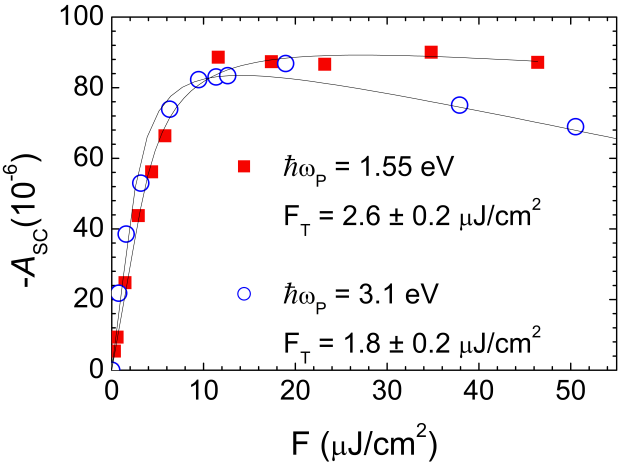


Figure 31: Fluence dependence of the amplitude of the component C below T_c. For $\mathscr{F} > \mathscr{F}_T$ the plateau appears. Thin lines are fits with Eq.(39) and (40).

taking into account the BCS-gap temperature dependence with $\frac{2\Delta_0}{k_B T_c} \approx 3.52$.

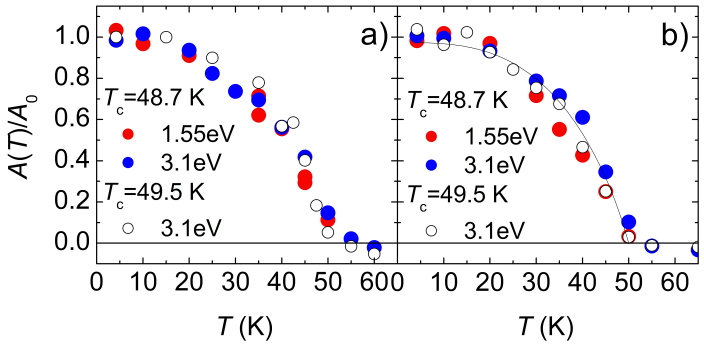


Figure 32: Temperature dependence of the superconducting component C (a) at 2.9 μJ/cm^2 and 3 μJ/cm^2 for 1.55 eV and 3.1 eV and (b) 17.4 μJ/cm^2 and 15 μJ/cm^2 for 1.55 eV and 3.1 eV, respectively. Thin lines in (b) are fits with Eq.(48).

However, the shape of the temperature dependence in Eq.(48) is a very weak function of $\frac{2\Delta_0}{k_B T_c}$ and therefore we cannot reliably distinguish the contributions from different gaps [116] and reliably determine $\frac{2\Delta_0}{k_B T_c}$.

3.1.2.3 Response in the normal state

The temperature dependence of the component-B amplitude is consistent with a bottleneck due to the relaxation over a T-independent gap (see Fig. 33) with a magnitude $2\Delta_{PG} = 120$ meV as noted previously [15]:

$$\Delta R \propto n_{pe} \propto \left[1 + g_{ph} \exp\left[-\frac{\Delta_{PG}(T)}{k_B T}\right]\right]^{-1}. \tag{49}$$

The subpicosecond part of component A on the other hand is temperature independent suggesting a finite density of states at E_F. This is consistent with heat-capacity measurements in polycrystalline $SmFeAsO_{1-x}F_x$ (Refs. [117] and [118]) where a finite Sommerfeld constant in the superconducting state suggests a finite density of states at E_F. Due to very

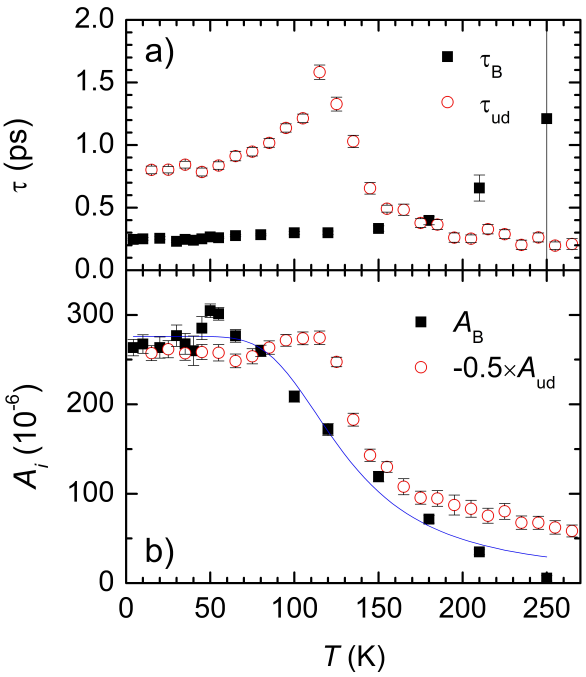


Figure 33: (a) Temperature dependence of the component-B relaxation time and (b) amplitude in superconducting $SmAsFeO_{0.8}F_{0.2}$ obtained from the fits. The thin line is the fit with Eq.(49) for the case of a relaxation over a T-independent gap. For comparison, the temperature dependence of the relaxation time and the transient amplitude in undoped SmAsFeO is also shown.

similar pump-photon energy dispersion of components A and B (see Fig. 26) we believe that they originate from the same electronic states which develop a soft-gapped density of states at E_F when temperature is decreased. Saturation of component-B amplitude with increasing $\mathscr{F}$ indicates that the pseudogap can be destroyed so it is not a simple band-structure effect.

The pump-photon energy dispersion similar to that of components A and B is not observed for component C. Electronic states involved in the relaxation related to components A and B must therefore be different than for component C. This confirms that the relaxation below T_c does not proceed via a cascade but rather through distinct parallel channels as suggested previously [15]. These channels correspond to two distinct electronic subsystems which are weakly coupled on the subpicosecond timescale. One exhibits the superconducting gap(s) and the other a pseudogap.

A possible origin of the distinct electronic subsystems could be a chemical phase separation of the doped F. However, the superconducting transition is rather narrow (see Fig. 24) so the presence of weakly superconducting fluorine-poor regions in which SDW is suppressed giving rise to additional pseudogapped electronic subsystem is also unlikely. More importantly undoped SmFeAsO shows virtually no pump-photon energy dispersion which the superconducting sample does, so a simple chemical phase separation to doped and undoped regions is very unlikely despite similarity (see Fig. 26) between component A and the undoped SmFeAsO room temperature transients. Moreover, there is no divergent signal at 125 K (or anywhere near that temperature) which can be attributed to the presence of the undoped phase in the superconducting sample. We therefore believe that both electronic subsystems are intrinsic to the SC material.

Apart from the chemical phase separation an intrinsic electronic phase separation akin to that proposed for the cuprates [119] could be origin of the distinct electronic subsystems. The existence of intrinsic electronic phase separation has been reported in "122" systems [120, 121], however, at present the issue is still rather controversial.

In the case of the spatially homogeneous electronic state different electronic subsystems

would correspond to different bands crossing E_F. This would imply that the interband scattering between parts of the Fermi surface corresponding to different electronic subsystems is negligible on a timescale of a few hundred femtosecond, since excitation photon at 1.5 eV only weakly excites components A and B. Further, since both components exist in the superconducting state even at low $\mathscr{F}$ the part of the Fermi surface corresponding to components A and B has to remain ungapped or pseudogapped in the superconducting state.

Another possibility for a weakly coupled electronic subsystem is Sm crystal-field levels. The energy of the levels in $SmFeAsO_{1-x}F_x$ is in the range of 20–60 meV as determined indirectly from heat-capacity fits [122, 123]. Involvement of the crystal-field levels could explain the strong $\hbar\omega_p$ dependence of components A and B and decoupling from the other lowlying electronic states. However, the observation of a pseudogap by NMR in La-1111 (Refs. [101] and [102]) (which has no crystal-field level structure at low energy), and the weak $\hbar\omega_p$ dependence in undoped SmFeAsO point against such a scenario.

3.2 Femtosecond spectroscopy in *X*-122 (*X*=Sr,Ba) iron-based pnictides

This section is organized as follows. Firstly, we present a study of quasiparticle relaxation dynamics in undoped $SrFe_2As_2$ single crystals, exhibiting spin-density wave (SDW) ordering. A temperature and fluence dependence study of the transient reflectivity will be discussed in detail. From the relaxation time above T_{SDW} we determine the second moment of the Eliashberg spectral function. The second part of this section is dedicated to a systematic doping dependence of the quasiparticle relaxation dynamics in $Ba(Fe_{1-x}Co_x)_2As_2$ single crystals. We determined the destruction SC energy density from the pump fluence dependence. In addition, the magnitudes of the SDW and SC gap were estimated from the temperature dependence of $\Delta R/R$ transients. At the end, from the relaxation dynamics at room temperature we estimated the electron-phonon coupling constant λ and found that λ decreases with increasing doping.

3.2.1 Temperature dependence of $\Delta R/R$ transients in undoped $SrFe_2As_2$ single crystals

Optical experiments on $SrFe_2As_2$ single crystals were conducted in essentially the same way as it was done for Sm-1111. To study the quasiparticle relaxation dynamics in undoped $SrFe_2As_2$ single crystals we apply 50 fs laser pulses at photon energy $\hbar\omega_p = 3.1$ eV and $\hbar\omega_{pr} = 1.55$ eV for the pump and probe pulses, respectively. The pump and probe beam diameters remained the same as in Sm-1111 experiments.

In Fig. 34 we plot the temperature dependence of $\Delta R/R$ transients measured at pump fluence 17 μJ/cm^2. Similarly as in undoped SmFeAsO, we can label three T regions. Below T_{SDW} the $\Delta R/R$ transients are dominated by the initial single exponential relaxation followed by a weak structure at around 10 ps (see Fig. 35).

At T_{SDW} a critical slowing down of relaxation is observed in the form of a long-lived relaxation tail which is following the initial ~ 1 ps exponential decay. Above T_{SDW} the amplitude of the initial subpicosecond relaxation strongly drops and the structure on a longer time scale becomes apparent. The behavior is similar to undoped SmFeAsO (see Fig. 20) with the exception of the subpicosecond relaxation amplitude above T_{SDW} being smaller in $SrFe_2As_2$.

In accordance with the previous experiments (see Section 3.1.1., [124]), we observed an increase of the $\Delta R/R$ transients amplitude at $T<T_{SDW}$ (Fig. 36). This is related to the appearance of the bottleneck in the relaxation [14], due to opening of a T-dependent charge gap. The SDW gap itself arises from the SDW formation and concurrent Fermi surface reconstruction. From the fit with Eq.(26) we found $2\Delta_{SDW}/k_B T_{SDW} \simeq 7.2 \pm 1$.

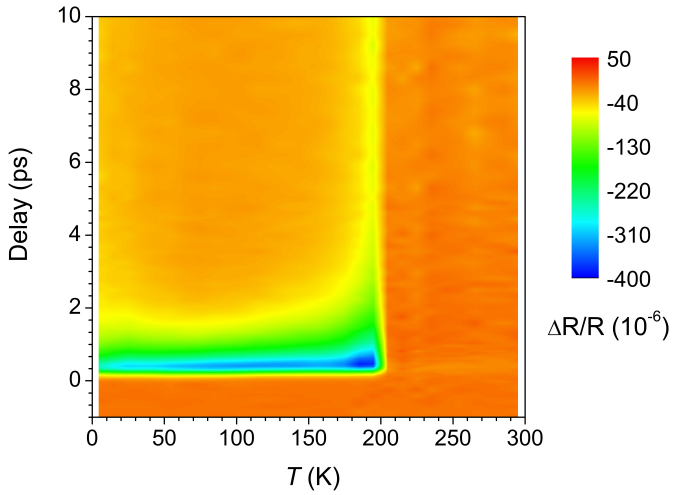


Figure 34: 2D temperature dependence plot of the reflectivity $\Delta R/R$ transients measured at $\hbar\omega_p = 3.1$ eV and 17 μJ/cm^2 pump fluence.

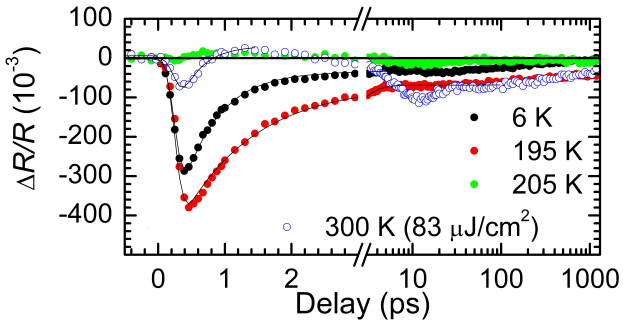


Figure 35: Reflectivity transients $\Delta R/R$ at 6, 195 and 205 K, taken at 17 μJ/cm^2 pump fluence. A remarkable slowing down of the relaxation at $T_{SDW} = 200$ K is clearly seen. Thin lines are single exponential decay fits of the data and data for 300 K is inserted for a comparison.

The observed characteristic SDW gap energy is close to the magnitude of the largest of the two SDW gaps (see Fig. 37) obtained from the optical conductivity [100]. Since the interband scattering is strong, as argued below, the smallest of the gaps should present the bottleneck for the hot carrier energy relaxation so our data do not confirm the existence of the smaller gap as suggested by [100].

Above $\sim$ 230 K our data on relaxation time τ nicely follow the predicted linear T-dependence (see Fig. 36(b)) with $\lambda\langle\omega^2\rangle$=110$\pm$10 meV^2. The phonon spectrum of $SrFe_2As_2$ extends up to $\sim$40 meV with the acoustic phonon cutoff at $\sim$10 meV [125]. To estimate the electron-phonon coupling constant, λ, we determine the ratio $\lambda\langle\omega^2\rangle/\lambda$ by assuming that the electron-phonon spectral function, $\alpha^2F(\omega)$, has the phonon density-of-states (DOS) shape [125,126] and obtain $\lambda\langle\omega^2\rangle/\lambda \simeq 430$ meV^2. This gives $\lambda \simeq 0.25$, which is rather low to explain the superconducting critical temperatures in doped compounds within a standard BCS model. If however, $\alpha^2F(\omega)$ is for some reason enhanced in the low-energy phonons region, λ could easily reach significantly higher values.

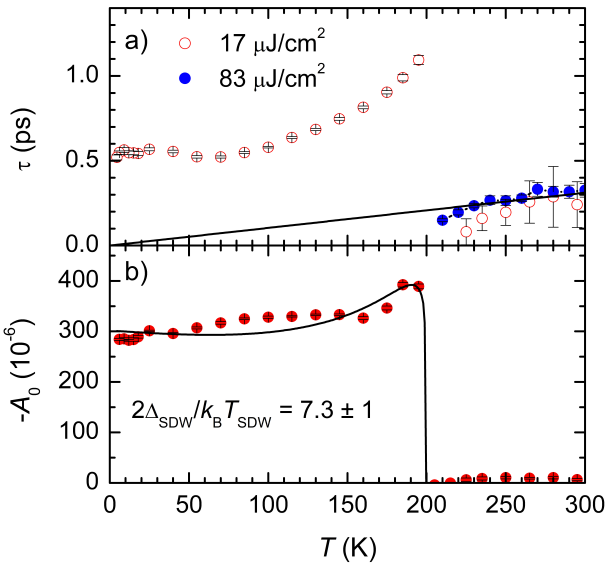


Figure 36: Temperature dependence of the relaxation time (a) and reflectivity $\Delta R/R$ transients amplitudes (b), measured at 17 μJ/cm^2 pump fluence. Thin black lines in (a) and (b) represent the fits with Eq.(31) and Eq.(26), respectively.

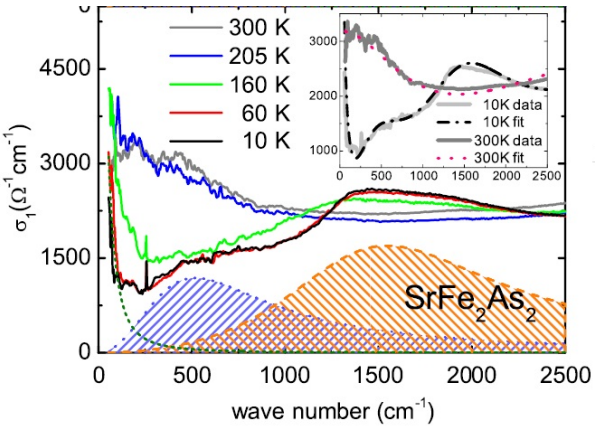


Figure 37: The real part of the optical conductivity $\sigma_1(\omega)$ measured in undoped $SrFe_2As_2$ single crystals. Two peaks at ~ 500 cm^{-1} and ~ 1360 cm^{-1} refer to two SDW gaps with magnitude $2\Delta/k_BT_{SDW} \approx 3.5$–$3.6$ and 9–9.6, respectively. Adopted from Ref. [100].

3.2.2 Fluence dependence of $\Delta R/R$ transients in undoped $SrFe_2As_2$ single crystals

The amplitude of the initial subpicosecond peak shows a minor departure from the linear pump fluence dependence at the highest $\mathscr{F}$ (see Figs. 38 and 39) while the subpicosecond relaxation time is virtually $\mathscr{F}$-independent (see Fig. 38(a)).

At low T however, an additional nonexponential slow relaxation component appears at the lowest fluence (see Fig. 39) which can be (beyond 5–10 ps) attributed to the heat diffusion out of the excitation volume [16] as indicated by fits in Fig. 39(b).

Similarly as in SmFeAsO, the relaxation time τ and $\Delta R/R$ transients amplitudes are

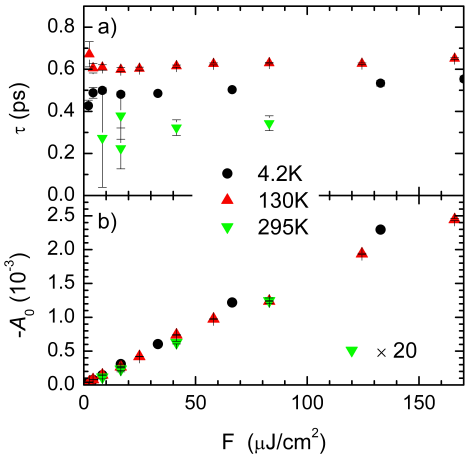


Figure 38: Fluence dependence of (a) the relaxation time and (b) reflectivity $\Delta R/R$ amplitudes at different temperatures.

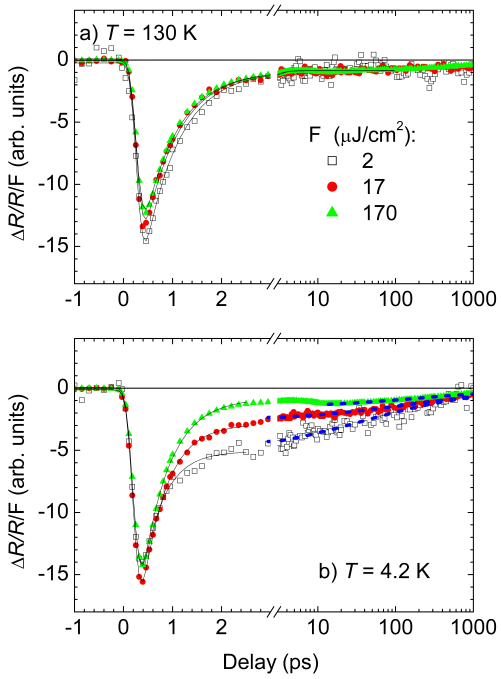


Figure 39: Normalized $\Delta R/R$ transients at selected pump fluences measured at $T = 130$ K (a) and $T = 4.2$ K (b). Thin black lines are single exponential decay fits and blue dashed lines are one-dimensional diffusion fits [16].

independent of the fluence at all temperatures. We can rule out the ballistic hot electron escape as a source of the low-T relaxation-time divergence cutoff [17] due to the relatively high resistivity of $SrFe_2As_2$ [127] and large optical penetration depth of ~ 60 nm at $\hbar\omega_{pr} = 1.55$ eV. However, in iron pnictides, due to the presence of ungapped electronic bands below T_{SDW}, the energy relaxation is not limited by the anharmonic energy transfer from the high-frequency to the low frequency phonons, but rather by the interband scattering (IBS) from the states at the edge of the SDW gap to the states in ungapped band(s) with energies $\varepsilon - \varepsilon_F \gg k_B T$. Such scattering can be enhanced by the presence of impurities, which may explain the difference between the higher residual resistivity in $SrFe_2As_2$ and lower residual resistivity in $UNiGa_5$ [109] (Fig. 40).

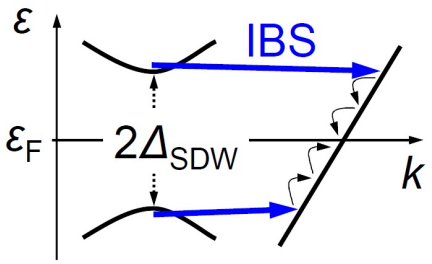


Figure 40: A schematic of the relaxation pathway via interband scattering in $SrFe_2As_2$.

The absence of multiple relaxation components (apart from diffusion) from the $\Delta R/R$ transients together with IBS imply that mainly the hot carriers from the SDW gaped electronic bands contribute to the photoinduced reflectivity transients. This does not hinder the determination of $\lambda\langle\omega^2\rangle$ as discussed above since the momentum scattering, which becomes faster than the energy relaxation rate at high temperatures, results in an effective averaging of $\lambda\langle\omega^2\rangle$ over all the bands.

3.2.3 Relaxation dynamics in underdoped $Ba(Fe_{1-x}Co_x)_2As_2$ single crystals

Temperature dependence of the raw photoinduced reflectivity $\Delta R/R$ in undoped Ba-122 samples (Co-0 % 2.5 % and 5.1 %) is shown in Fig. 41. Even though, no deliberate uniaxial strain was applied, the samples showed a twofold rotational anisotropy with respect to the probe polarization at temperatures $T < 200$ K. In the orthorhombic state, the anisotropy indicates a preferential ordering of the orthorhombic twin domains in the probed volume. The anisotropy slightly varies along the surface of the samples with isolated spots that show almost no anisotropy. The transients of the less anisotropic spots are consistent with a linear combination of the most anisotropic transients. Therefore, the variation is not due to the sample inhomogeneity [85], but due to the spatially inhomogeneous detwinning.

In the iron-based pnictides, the probed volume is limited to a few tens of nanometers thick layer near the surface [124] due to their optical penetration depth values. Therefore, we attribute the observed anisotropy to an anisotropic surface-strain bias induced by the local pump-beam thermal load in the presence of the unidirectionally ordered terraces (see Fig. 42).

In the absence of information which crystallographic direction corresponds to the two different orthogonal probe polarization we denote the polarization according to the low-T minimum and maximum $\Delta R/R$ peak as $\mathscr{P}^-$ and $\mathscr{P}^+$, respectively.

The response in the undoped Co-0 % sample is very similar to previous results in undoped $SrFe_2As_2$ [72] and SmAsFeO [124]. In the 2D plot we can identify three different T areas. Below $T_s = T_{SDW}$ the transients are dominated by the initial single exponential relaxation (see Fig. 21). At T_s a slowing down of relaxation is observed in the form of a long-lived

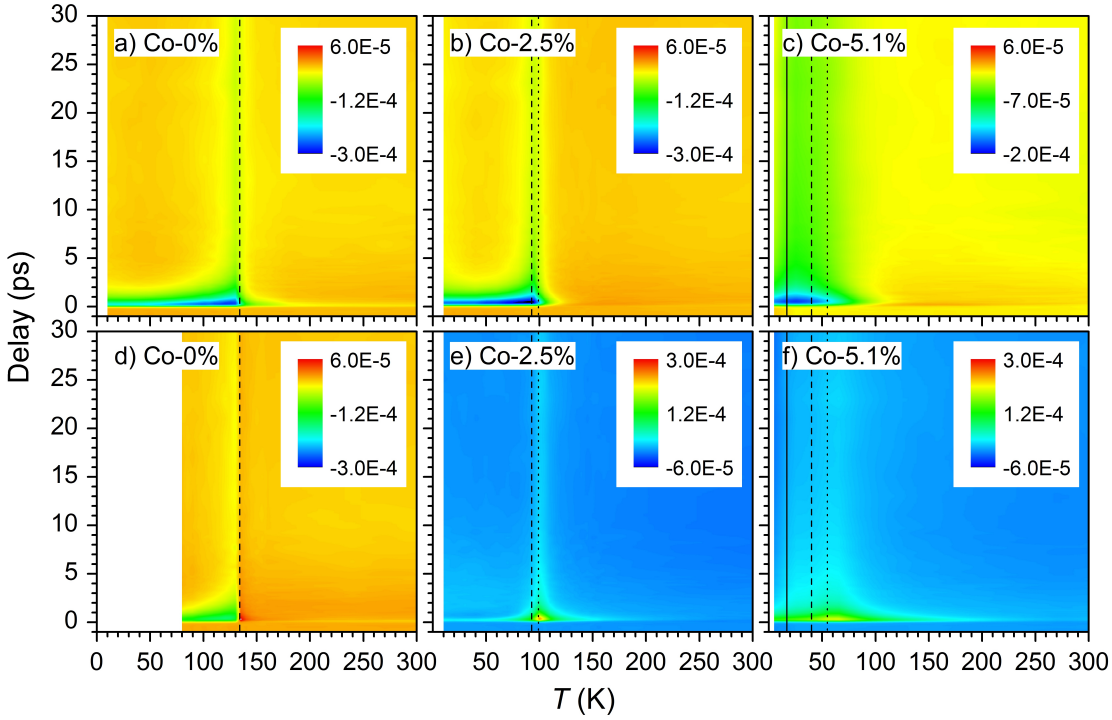


Figure 41: 2D temperature dependence plot of $\Delta R/R$ transients in underdoped $Ba(Fe_{1-x}Co_x)_2As_2$ at 13 μJ/cm^2 pump fluence. The top row (a)-(c) refers to the $\mathscr{P}^-$ and bottom row (d)-(f) to the $\mathscr{P}^+$ probe polarization. The vertical lines indicate T_c (full lines), T_{SDW} (dashed lines), and T_s (dotted lines). The level of Co-doping is indicated in left top corner of each figure.

relaxation, which is following the initial ~ 1.5 ps exponential decay and extends throughout the experimental nanosecond time window. Above T_s the amplitude of the initial sub-ps relaxation strongly drops and the structure at around 10 ps, which was observed also in previously studied iron-pnictides, becomes apparent. The structure could be associated with the acoustic wave propagating into the sample after expansion of the excited volume due to the transient laser-pulse heating and will not be discussed further.

With increasing Co doping the anomalies around T_s become broader (see Figs. 41 and 43) and the drop of the amplitudes with increasing T above T_s becomes slower. There are no clear separate features observed at the spin-density-wave (SDW) transition temperature (T_{SDW}) in the Co-2.5 % and Co-5.1 % samples, where the SDW transition is split from the structural phase transition.

Regarding the probe polarization anisotropy, there is marked difference in the probe polarization anisotropy of the Co-0 % sample with respect to the Co-2.5 % and Co-5.1 % samples where the amplitude shows either a peak for the $\mathscr{P}^+$ polarization or a step-like increase for the $\mathscr{P}^-$ polarization at T_s (see Fig. 47). This difference could be explained by a lower degree of detwinning due to the surface-strain bias in the Co-0 % sample.

At low-T the initial relaxation can be fit well with a single exponential decay in both polarizations in Co-0 % sample.(Fig. 43 (a), (b)) However, the samples with finite dopings show a multicomponent relaxation (Figs. 43 and 44). To fit the $\Delta R/R$ transients for both polarizations up to 100 ps delay and to determine T-dependencies of relaxation time, we employ three exponentially decaying components [114]:

$$\frac{\Delta R}{R} = \sum_{i\in(\mathrm{A,B,C})} \frac{A_i}{2} \mathrm{e}^{-\frac{t-t_0}{\tau_i}} \mathrm{erfc}\left[\frac{\sigma^2 - 4(t-t_0)\tau_i}{2\sqrt{2}\sigma\tau_i}\right] + \frac{A_0}{2}\mathrm{erfc}\left[\frac{\sqrt{2}(t_0-t)}{\sigma}\right]. \tag{50}$$

Here, σ stands for the effective width of the excitation pulse with a Gaussian temporal profile arriving at t_0 and τ_i exponential relaxation times. The last term in Eq.(50) accounts

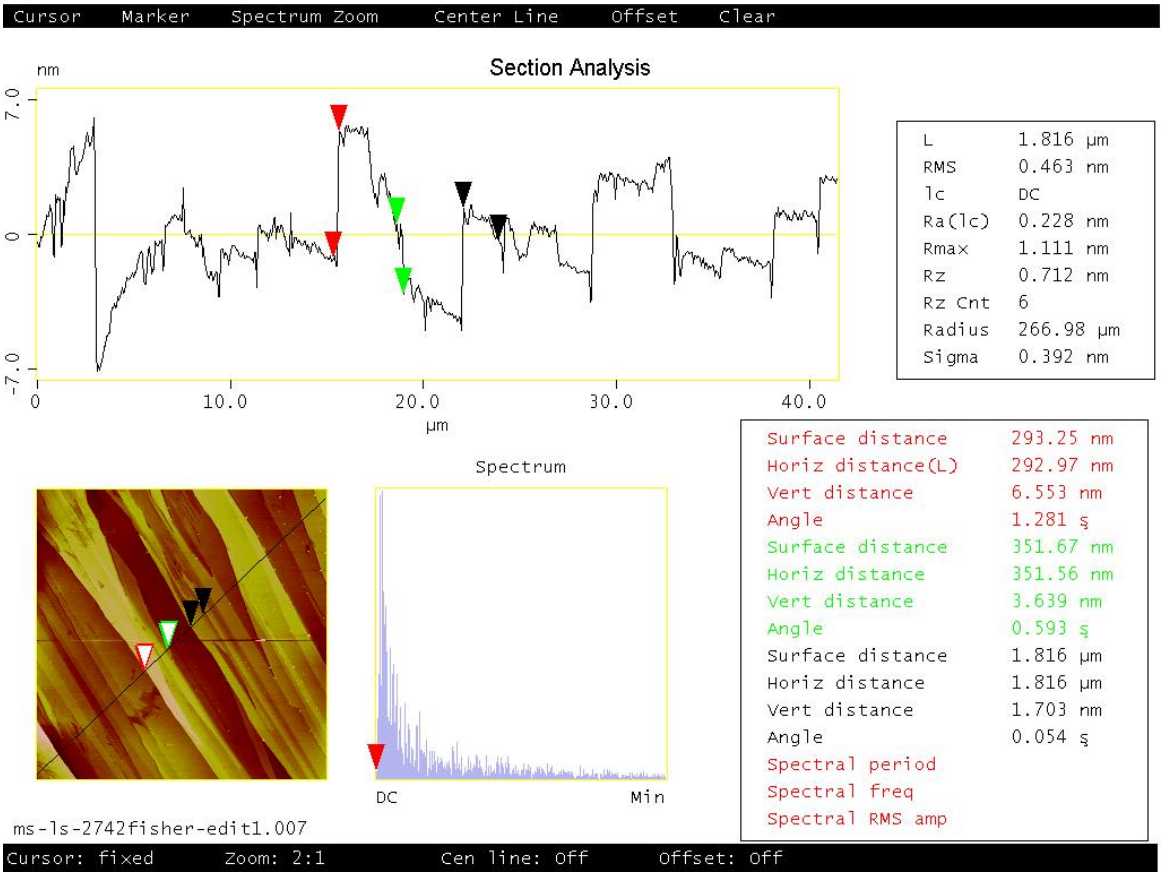


Figure 42: Atomic force microscopy (AFM) characterization of the cleaved surface in Co-5.1% doped $Ba(Fe_{1-x}Co_x)_2As_2$ sample. The AFM analysis was done at $T = 300$ K on the area where the optical experiments were previously performed.

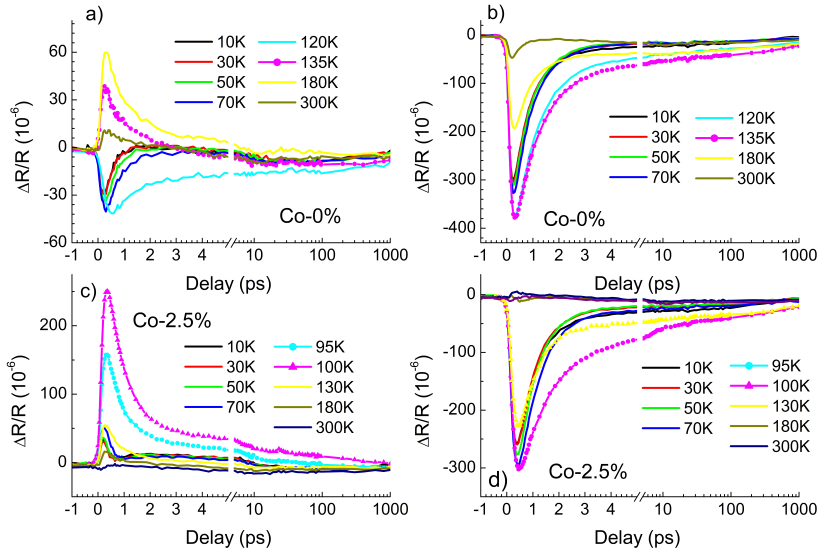


Figure 43: The photoinduced reflectivity $\Delta R/R$ transients at 13 μJ/cm^2 pump fluence as a function of temperature at Co-0 % (a),(b) and Co-2.5 % (c),(d) dopings. The left column corresponds to the $\mathscr{P}^+$ and the right one to the $\mathscr{P}^-$ polarization. Full circled line represents T_{SDW}, where the full triangled line refers to T_{s}.

for slower processes which are not of interest here. During the fitting the relaxation times for the two orthogonal polarizations were linked while amplitudes were kept independent.

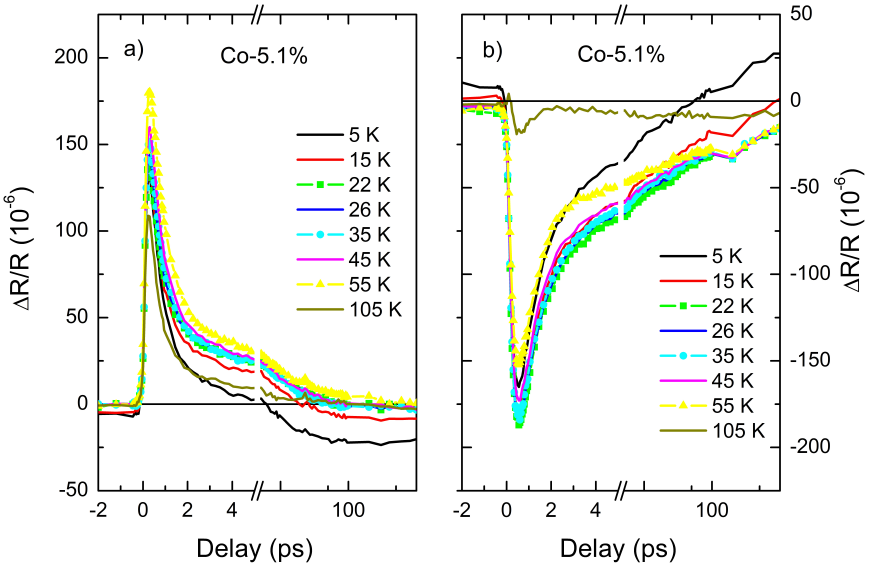


Figure 44: Raw T-dependence of $\Delta R/R$ transients in Co-5.1 % sample, taken at 13 μJ/cm^2 pump fluence. (a) corresponds to the $\mathscr{P}^+$ and (b) to the $\mathscr{P}^-$ polarization. Full circled line represents the T_{SDW}, full triangled line refers to T_{s} and full squared line applies to T_{c}.

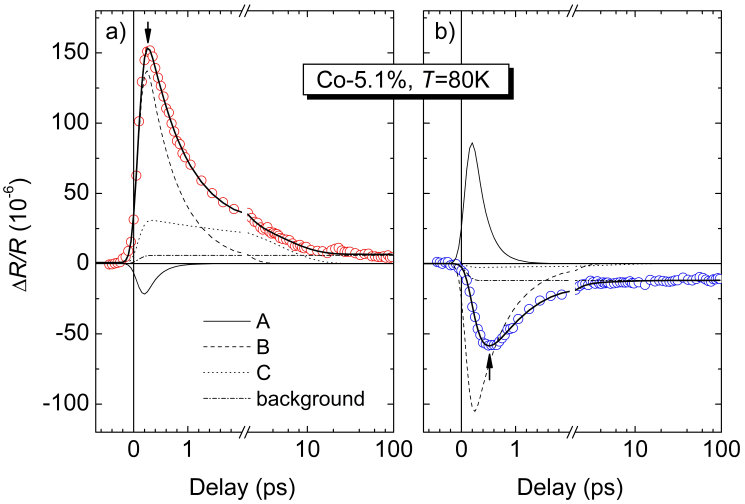


Figure 45: Three-exponential fit with Eq.(50) for (a) $\mathscr{P}^+$ and (b) $\mathscr{P}^-$ probe polarization for Co-5.1 % doped $Ba(Fe_{1-x}Co_x)_2As_2$ sample.

Component A (see. Fig. 45) with relaxation time $\tau_{\mathrm{A}} \sim 0.2$ ps is needed to fit the difference in the rise time dynamics between the two orthogonal probe polarizations. The component is absent in the Co-0 % and superconducting Co-11 % samples and appears below ~ 150 K in the other samples (Fig. 46 (a), (b)) with the relaxation time only weakly dependent on the temperature. It could be associated with the initial relaxation of the high energy optically excited electrons towards the Fermi energy and/or the inter-band momentum scattering between states near the Fermi energy at different parts of the Fermi surface [128, 129].

Component B is the main component present in all samples (Fig. 46 (d)) representing the initial $0.3 - 1.5$ ps decay. The relaxation time, τ_{B}, (see Fig. 46 (c)) shows a slowing

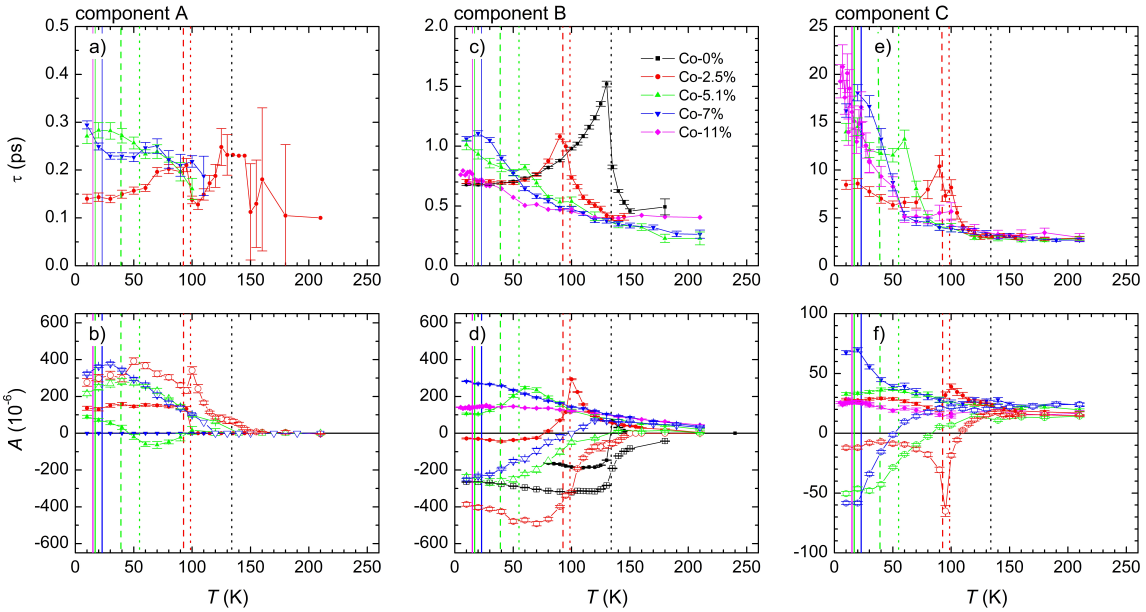


Figure 46: Multiexponential fit of the relaxation time (a), (c), (e) and corresponding amplitudes (b), (d), (f). Full symbols refer to $\mathscr{P}^-$ and empty symbols to $\mathscr{P}^+$ probe polarization. Data for optimally doped Co-7 % and overdoped Co-11 % sample are also shown. The vertical lines indicate T_c (full lines), T_{SDW} (dashed lines), and T_s (dotted lines).

down at T_s in the samples with the SDW order. The peak in τ_B is only weakly pronounced in the Co-5.1 % sample, which shows the SDW-SC coexistence, and is completely absent in the Co-7 % and Co-11 % samples, where we observe a monotonous increase of τ_B with decreasing temperature. The apparent peak of τ_B at T_c in the Co-7 % sample is due to the appearance of the SC relaxation component.

Component C (see Fig. 46 (e), (f)) has the longest relaxation time (τ_C) spanning from a few ps at 200 K up to 20 ps at 5 K in the Co-7 % and Co-11 % samples. At high temperatures, the component C is strongly influenced by the acoustic wave feature around 10 ps delay. In the Co-2.5 % and Co-5.1 % samples τ_C also slows down near T_s. The qualitative behavior of this component is very similar to component B so it is very likely that both components together are due to a single process with a non-exponential decay dynamics.

3.2.3.1 Determination of the gap in the SDW state

Below T_s the $\Delta R/R$ amplitude shows different T-dependence for the two orthogonal probe polarizations which is the most clearly pronounced in the Co-2.5 % sample (see Fig. 47). This indicates that the states involved in the two orthogonal probe polarizations correspond to different parts of the Fermi surface, presumably originating from different bands crossing the Fermi energy as confirmed by the recent ARPES photon-polarization analysis in untwinned $Ba(Fe_{1-x}Co_x)_2As_2$ [130]. However, the SC component shows the same T-dependence for both polarizations consistent with isotropic SC gaps.

To analyze the anisotropic T-dependence we use the relation that describes the photoinduced reflectivity change due to the presence of photoexcited carriers:

$$\Delta R_{\alpha,\beta} \propto \int \mathrm{d}^3k \left[|M_{\alpha,\beta}(\mathbf{k})|^2 \Delta f_\alpha(\mathbf{k}) \times g(\varepsilon_\beta(\mathbf{k}) - \varepsilon_\alpha - \hbar\omega_{\mathrm{probe}}) \right]. \tag{51}$$

Here, $M_{\alpha,\beta}$ is the effective probe-polarization dependent optical-dipole matrix element between an initial band, α, and a final band, β, $\Delta f_\alpha(\mathbf{k})$ the photoexcited change of the charge-carrier distribution function in the initial band, $g(\varepsilon)$ the effective transition line-shape and

$\hbar\omega_{\text{probe}}$ the probe photon energy. For simplicity we assumed that the energy of the final band is far from the Fermi energy, $\left|\varepsilon_\beta(\mathbf{k})-\varepsilon_{\text{F}}\right|\sim\hbar\omega_{\text{probe}}\gg k_{\text{B}}T$, so $\Delta f_\beta(\mathbf{k})$ can be neglected after the fast initial relaxation of the ultra-hot carriers.

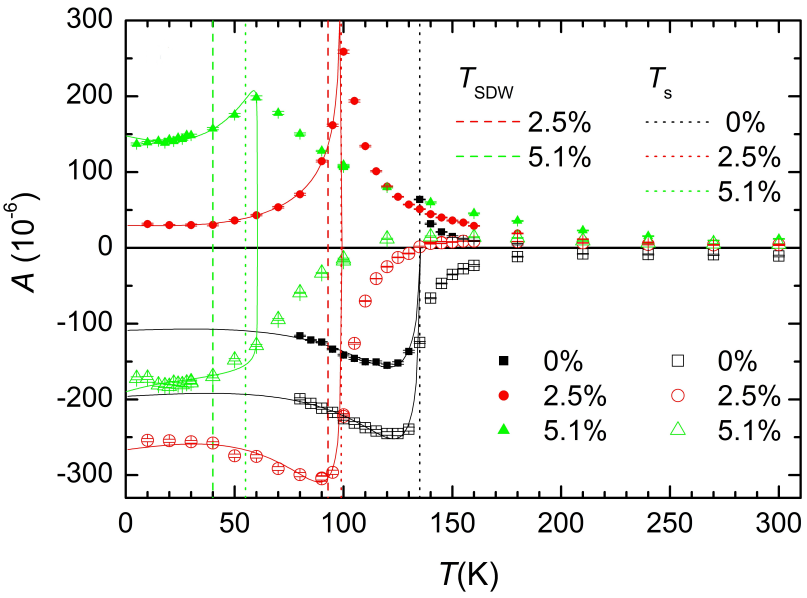


Figure 47: Temperature dependence of the raw $\Delta R/R$ transients in 0 %, 2.5 % and 5.1 % Co-doped samples at 13 μJ/cm^2 pump fluence. Full and open symbols correspond to $\mathscr{P}^+$ and $\mathscr{P}^-$ probe polarization. The vertical lines indicate T_{SDW} (dashed line) and T_{s} (dotted line). Thin lines are fits of Eq.(52).

The integral in Eq.(51) selectively samples $\Delta f_\alpha(\mathbf{k})$ in different regions of k-space depending on the probe polarization and photon energy. Due to contributions of several optical transitions with finite effective line-widths it is usually assumed that Eq.(51) smoothly samples over the relevant energy range in the vicinity of the Fermi energy and ΔR can be approximated by the total photoexcited carrier density, $\Delta R=\gamma n_{\text{pe}}$ [14, 18], and any change of ΔR upon change of external parameters (T for example) is attributed to the change of n_{pe} while the proportionality factor γ is assumed to be a constant.

Table 1: Charge gap magnitudes in the Ba-122 samples, exhibiting SDW ordering.

Material	$2\Delta(0)/k_{\text{B}}T_{\text{s}}$
Co-0 %	9±2
Co-2.5 %	7±2
Co-5.1 %	4±2

In $Ba(Fe_{1-x}Co_x)_2As_2$ however, a complex band structure reorganization with bands shifting by as much as 80 meV has been observed below T_{s} [131]. These shifts can significantly modify the sampling region of the integral (Eq.(51)) and violate the assumption of a constant γ. To take this into account, we therefore assume that γ is temperature dependent and expand it in terms of an order parameter. The order parameter can be associated with the opening of a partial T-dependent charge gap $\Delta(T)$ upon the Fermi surface reconstruction below T_{s}. Assuming a complex BCS-like order parameter with the magnitude $\Delta(T)$ below T_{s} we obtain:

$$\Delta R=\left[\gamma_0+\eta\Delta(T)^2\right]n_{pe}. \tag{52}$$

The relative gap magnitudes presented in Table (1) are consistent with values [124, 132] in SmFeAsO and $SrFe_2As_2$ and show a decrease with doping, consistent with a decrease of

the stability of the orthorhombic SDW state.

Similarly to *Re*FeAsO (*Re*=La, Nd and Sm) [133] the onset of the partial gap opening can be associated with the structural and not SDW transition.

3.2.4 Response in the superconducting $Ba(Fe_{1-x}Co_x)_2As_2$ samples

Due to a finite noise magnitude we were able to investigate the $\mathscr{F}$-dependence of the SC component below the saturation fluence only in the nearly optimally doped sample ($x = 7$ %) with the highest $T_c \simeq 23$ K. At the lowest $\mathscr{F}$ the SC component dominates the raw $\Delta R/R$ transients (see Fig. 49). With increasing $\mathscr{F}$, however, the SC component quickly saturates while an increasing contribution of the normal state components starts to prevail at shorter timescales resulting in a shift of the minimum corresponding to the saturated SC component for the $\mathscr{P}^-$ probe polarization (see Fig. 48 (a)) and the maximum for the $\mathscr{P}^+$ probe polarization (see Fig. 48 (b)) towards longer delays.

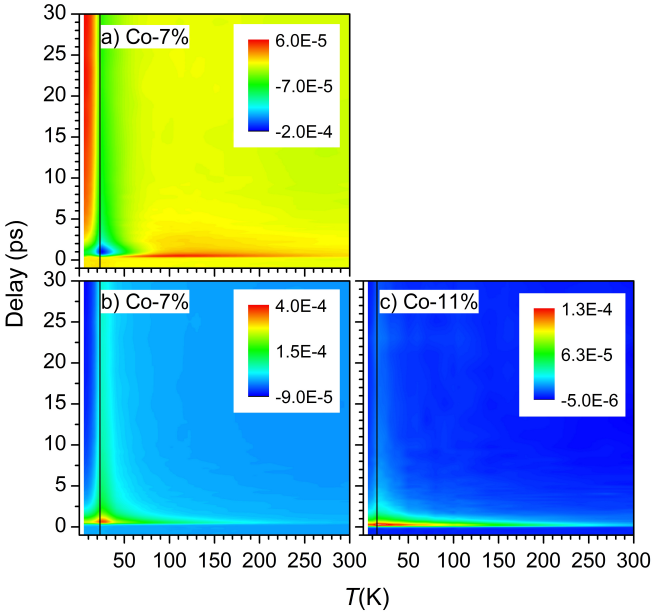


Figure 48: 2D temperature dependence plot of $\Delta R/R$ transients in optimally (a), (b) and overdoped (c) $Ba(Fe_{1-x}Co_x)_2As_2$ samples at 13 μJ/cm^2 pump fluence. The top row (a) refers to the $\mathscr{P}^-$ and bottom row (b)-(c) to the $\mathscr{P}^+$ probe polarization. The anisotropy is absent in Co-11 % doped sample. The vertical lines indicate T_c (full lines), T_{SDW} (dashed lines), and T_s (dotted lines). The level of Co-doping is indicated in left top corner of each figure.

Similarly as in Sm-1111, we subtract the $\Delta R/R$ transients measured at $T = 30$ K from the transients $\Delta R/R$ measured at 5 K in order to extract the SC component. Using the same inhomogeneous SC-state destruction model (Eq.39, 40) we fit the $\mathscr{F}$-dependence of the SC component amplitudes and find $\mathscr{F}_T$=0.43±0.04 μJ/cm^2. Taking into account the optical constants from [134] we obtain for the reflectivity $R = 0.37$ and the optical penetration depth $\lambda_{op} = 34$ nm at the 1.55 eV pump photon energy, giving the bulk SC state destruction energy density required to completely destroy the superconducting state: $U_{d,Co-122}/k_B = \frac{\mathscr{F}_T(1-R)}{\lambda_{op}k_B} = 0.3$ K/Fe ($U_{p,Co-122} = 4.9$ J/mole). This value is much smaller than the energy necessary to heat the sample thermally to T_c, $U_Q/k_B = \int_{5K}^{T_c} c_p/k_B dT \simeq 2.4$ K/Fe ($U_Q = 40$ J/mole) indicating that the SC destruction is highly non-thermal.

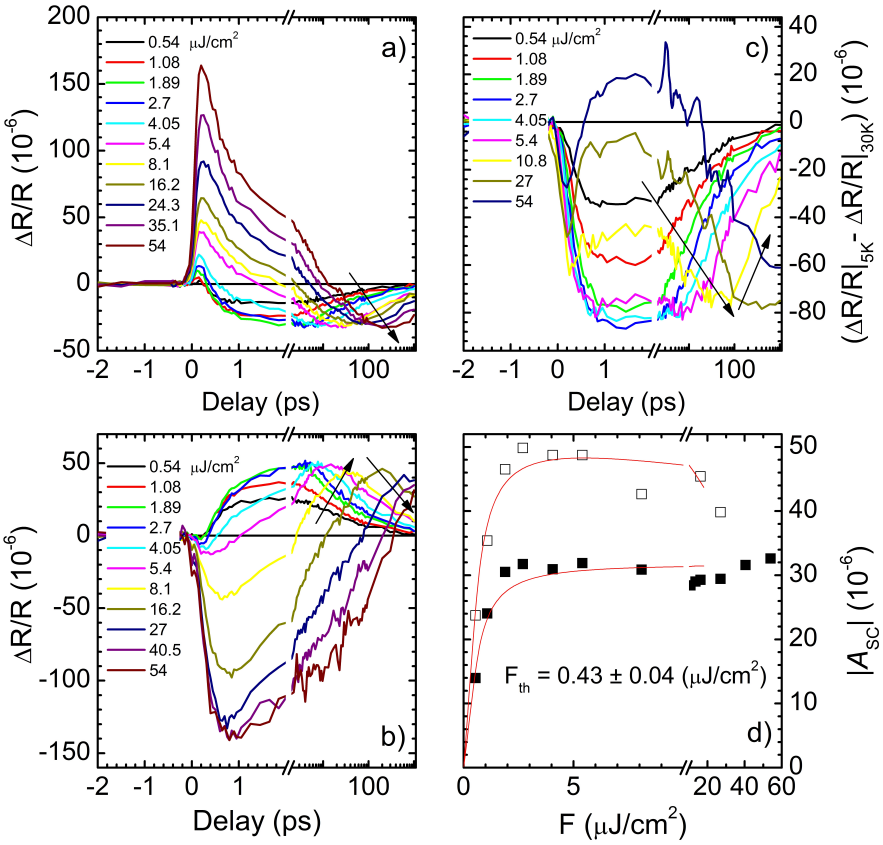


Figure 49: Fluence dependence of the raw $\Delta R/R$ transients in the optimally doped Co-7 % sample for (a) $\mathscr{P}^+$ and (b) $\mathscr{P}^-$ probe polarization, measured at $T = 5$ K and 1.55 eV pump photon energy. In (c) the fluence dependence of the subtracted SC component is shown for $\mathscr{P}^+$ polarization. The arrows indicate the direction of increasing $\mathscr{F}$. Fluence dependence of the SC component amplitude for $\mathscr{P}^+$ (full symbols) and $\mathscr{P}^-$ (open synmols) polarization is presented in (d) together with the fits (thin lines) with Eq.(39) and (40).

3.2.4.1 Temperature dependence and comparison with SmFeAs(O,F)

The temperature dependence of the SC component is shown in Fig. 50. (the average of the normal-state $\Delta R/R$ transients up to ~ 10 K above T_c were subtracted from the raw transients). The SC component shows a rise-time of $\tau_r \lesssim 0.5$ ps followed by a plateau extending from tens of picoseconds at 5 K to several hundred picoseconds when the temperature is increased towards T_c. The weak non-monotonic temporal dependence of the SC component during the plateau could not be reliably identified as an intrinsic effect and is attributed to a weak T-dependence of the subtracted normal state response. As discussed above, the plateau corresponds to the transient destruction of the SC state. The timescale of the SC state recovery following the plateau is ~ 1 ns at 5 K and increases with increasing temperature.

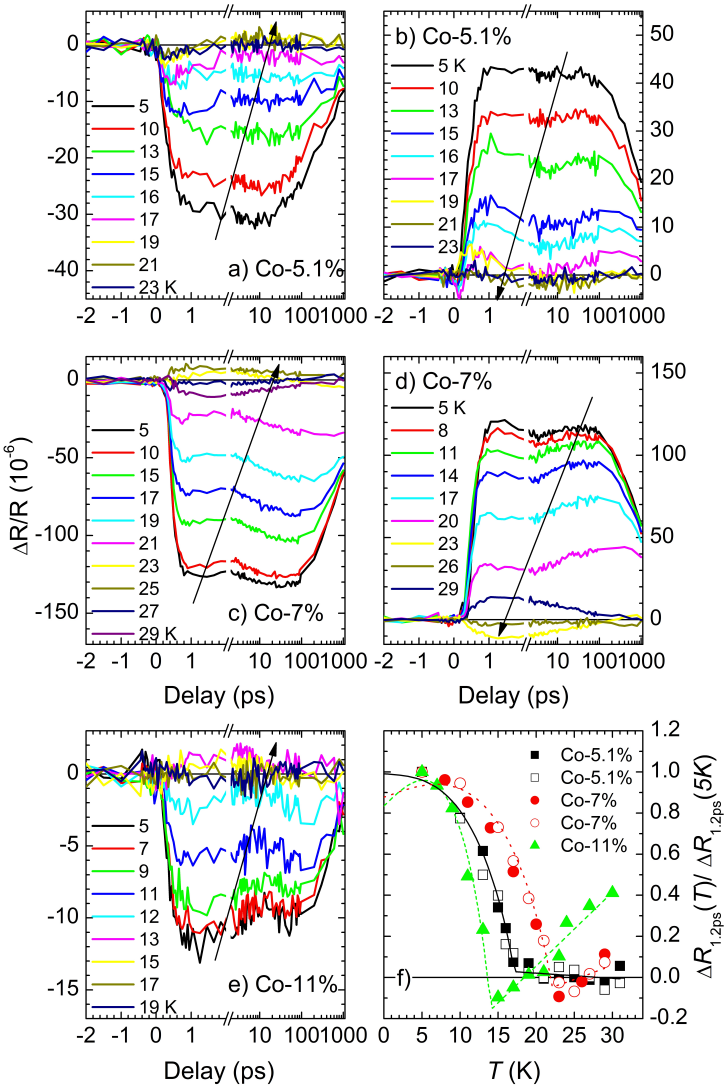


Figure 50: Temperature dependence of the SC component at 3.9 μJ/cm^2 in Co-5.1% sample (a) and (b), in the Co-7 % sample at 13 μJ/cm^2 pump fluence (c) and (d) and in Co-11 % sample at 2.9 μJ/cm^2 pump fluence (e). The left column corresponds to $\mathscr{P}^-$ and right to $\mathscr{P}^+$ probe polarization. In (f) the normalized photoinduced reflectivity at 1.2 ps in all superconducting samples is shown, where full and open symbols correspond to $\mathscr{P}^+$ and $\mathscr{P}^-$ probe polarizations, respectively. Thin lines in (f) are fits with the Mattis-Bardeen equation (48). The arrows indicate the direction of increasing temperature.

In Fig. 50 (f) we plot the temperature dependence of the SC-component saturated

amplitude for all SC samples. The linear T-dependence of the amplitude above T_c indicates some residual contribution due to the weak T-dependence of the non-SC contributions. Below T_c we observe (on top of the linear T-dependence) the characteristic Mattis-Bardeen T-dependence given by the high-frequency limit of the Mattis-Bardeen formula Eq.(48).

The presence of the plateau and the slow SC state recovery is different than in the near-optimally doped SmFeAs(O,F), where a two stage SC recovery was observed (see Section 3.1.2.1). The fast equilibration stage, appearing on a ~ 5 ps timescale in SmFeAs(O,F), corresponds to the initial local equilibration among all degrees of freedom and the slow, appearing on a several-hundred-picosecond timescale, corresponds to the energy escape from the optically probed volume by the diffusive heat transport. The absence of the two-stage relaxation in $Ba(Fe_{1-x}Co_x)_2As_2$ is consistent with the fact, that, at the pump fluences used for the T-scans, the total laser energy deposited in the optically probed volume corresponds to heating the sample to a temperature well above T_c, in the 30–40 K range. The sample thus remains in the normal state after the fast stage and the SC recovery is governed by the diffusive-heat-transport slow stage only.

Moreover, in the present case a separate two-stage relaxation is not observed even at the lowest $\mathscr{F}$ just above the threshold (see Fig. 49 (c)) suggesting that the initial local equilibration is slower than in SmFeAs(O,F). This could be ascribed to virtually clean SC gaps in the case of $Ba(Fe_{1-x}Co_x)_2As_2$ (and other "122" systems) in comparison to SmFeAs(O,F) where the relaxation dynamics and a large low-T heat capacity [117] suggest the presence of ungapped parts of the Fermi surface in the SC state [124].

However, only $\hbar\omega_p = 1.55$ eV and $\hbar\omega_p = 3.1$ eV were used to study $Ba(Fe_{1-x}Co_x)_2As_2$ and therefore additional ultrafast pump-probe spectroscopy study at different $\hbar\omega_p$ in "122" systems and measurements in $LaFeAsO_{1-x}F_x$ are needed for determination whether some fundamental difference between "1111" and "122" systems is responsible for the different relaxation-time behavior and marked temperature dependence above T_c in Sm-1111.

3.2.5 Normal state

Above T_s the T-dependent $\Delta R/R$ amplitude shows tails which can not be described by Eq.(26). These tails indicate a bottleneck in relaxation and therefore the presence of a pseudogap persisting up to ~ 200 K. With increasing Co doping the bottleneck becomes even more pronounced at higher T and remains present also in the non-SDW Co-7 % and Co-11 % samples.

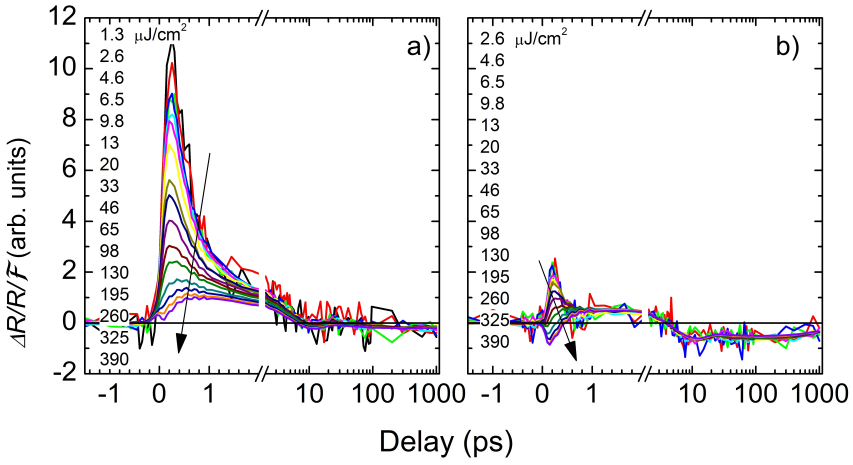


Figure 51: Fluence normalized $\Delta R/R$ transients for $\mathscr{P}^+$ (a) and $\mathscr{P}^-$ (b) probe polarization in the normal state at $T = 120$ K in Co-5.1 % sample. The arrows indicate the direction of increasing $\mathscr{F}$ where overlapping curves indicate a linear $\mathscr{F}$ dependence.

The $\mathscr{F}$ dependence of the $\Delta R/R$ transients shown in Fig. 51 indicates that at high excitation the relaxation component, saturates and the shapes of transients become almost identical to the room temperature ones. The observed external saturation fluences of the order of 100 μJ/cm^2 correspond to the absorbed optical energy of $\sim$50 K/Fe. This amount of energy would thermally heat the experimental volume for only a few K. Any property or a state, that is responsible for the tails, can therefore be non-thermally destroyed. This rules out any static effect, such as the surface-strain bias, a rigid band shift with T or a band-structure pseudogap, for example, as possible origins of the tails.

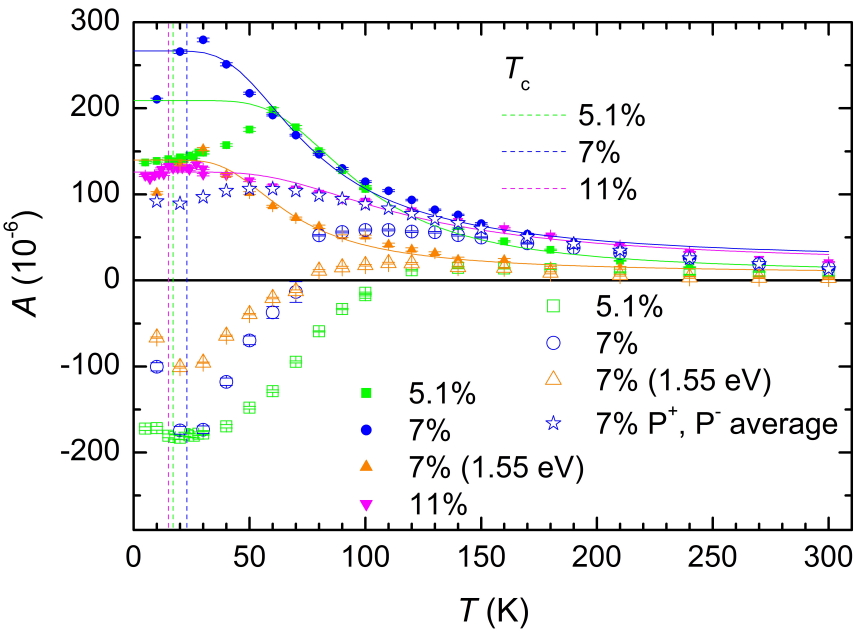


Figure 52: Temperature dependence of the raw $\Delta R/R$ reflectivity transients at 13μJ/cm^2 pump fluence in Co-5.1 %, 7 % and 11 % doped samples. Full and open symbols refer to $\mathscr{P}^+$ and $\mathscr{P}^-$ probe polarization, respectively. Vertical dashed lines indicate T_c. Open stars represent the amplitude of the probe-polarization averaged transients in the Co-7% sample. Thin lines are fits with Eq.(49).

To obtain a quantitative information about the pseudogap we analyze the normal state T-dependent $\Delta R/R$ magnitude (Fig. 52) in the context of the relaxation across a T-independent gap (Eq.(49)).

The obtained pseudogap magnitudes $2\Delta_{PG}$ (see Table (2)) are very similar to spin pseudogap magnitudes obtained from T-dependence of the Knight shift [135] suggesting that a suppression of density of states in the fluctuation region is present in both, spin and charge, densities of states. The presence of the charge pseudogap is supported also by the T-dependence of the c-axis electrical resistivity [130] and the V shape of the tunneling conductance spectra [136].
It should be noted that the charge pseudogap was observed also in the electron doped SmFeAs(O,F) [124,137], which, similarly as Ba(Fe$_{1-x}$Co$_x$)$_2$As$_2$, shows the spin pseudogap [101].

Table 2: Charge pseudogap magnitudes obtained from the fit with Eq.(49) and comparison with the pseudogap magnitudes obtained from T-dependence of the Knight shift [135].

Material	$2\Delta_{PG}$ (K)	$2\Delta_{Knightshift}$
Co-5.1 %	800±100	570 (Co-4 %)
Co-7 %	660±100	520 (Co-8 %)
Co-11 %	610±100	490 (Co-10.5 %)

3.2.5.1 Anisotropy

One of the most striking features of our data set is the observation of the 2-fold in-plane rotational anisotropy of the optical transients in the tetragonal phase (see Figs. 41, 48), well above T_s, without any deliberately applied external uniaxial stress. The absence of the anisotropy at the room temperature (Fig. 53) and in the Co-11 % sample proves that the observed anisotropy is not an experimental artifact but is intrinsic to our samples. At low dopings the high-T anisotropy axes match the orthorhombic-state anisotropy axes indicating that also the high-T anisotropy is oriented along the orthorhombic crystal axes direction. Moreover, the change of the sign of the SC component in Co-5.1 % and Co-7 % samples is a strong indication that the anisotropy originates from the bulk of the probed volume and not from the edges of the terraces.

In the absence of any structural data which would indicate that our samples are not tetragonal in the thermodynamic equilibrium above T_s, we assume that the breaking of the 4-fold tetragonal symmetry is not spontaneous, but is a consequence of anisotropic boundary and/or excitation conditions that introduce an anisotropic surface strain.

We believe that the strain is a consequence of the local crystal expansion due to the local thermal load. The anisotropy of the strain could be linked to the unidirectional terraces observed on the surface of the cleaved crystals. The strain is expected to be weak since the average increase of the temperature in the experimental volume is at most just a few K. The anisotropic response of the sample is therefore possible only if the system is very close to a spontaneous symmetry-breaking instability of the 4-fold rotational symmetry.

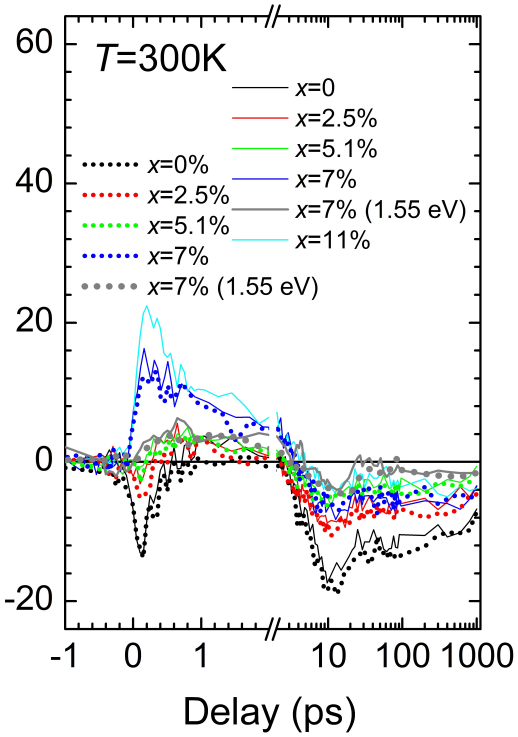


Figure 53: Raw $\Delta R/R$ transients measured at 13 μJ/cm^2 pump fluence and $T = 300$ K. The full and dotted lines correspond to $\mathscr{P}^+$ and $\mathscr{P}^-$ polarizations, respectively. The gray lines are the transients measured with 1.55 eV pump photon energy at 11 μJ/cm^2 in the Co-7 % sample.

Since the reflectivity is a second rank tensor the observed 2-fold anisotropy can not distinguish between the 2-fold in-plane rotational symmetries and the absence of any rotational symmetry (C_1). The observed 2-fold anisotropy is therefore compatible with a nematic order parameter [138] as well as with an in-plane antiferromagnetic (AF) ordering and even

in-plane ferro orderings. Since photons do not directly couple to spins the observation of AF fluctuations in optical response is at best of second order and therefore very unlikely. Moreover, there is no appreciable external magnetic field to order spins and the anisotropy is a continuous function of temperature with a clear anomaly at T_s and no anomaly at T_{SDW} in Co-2.5 % and Co-5.1 % samples. We therefore tentatively associate the 2-fold symmetry breaking instability with nematic fluctuations or ordering of the Fe d orbitals. The ordering is not necessary static at all temperatures since the timescale of relaxation is below ~ 0.5 ps. Similar nematic ordering, albeit static in the presence of an external uniaxial strain and at somewhat lower temperatures, was observed also by other techniques [83, 84, 131, 136].

Due to the concurrent appearance of the bottleneck and the polarization anisotropy of the transients around 200 K the pseudogap might be associated with the nematic fluctuations responsible for the 4-fold rotational symmetry breaking. The fluctuations appear to be particularly strong in the Co-5.1 % and Co-7 % samples where they order due to the surface-strain bias resulting in the probe polarization anisotropy and the change of the sign of the $\mathscr{P}^-$-probe-polarization transients well above any transition at ~ 110 K and ~ 70 K in the Co-5.1 % and 7 % samples, respectively. (see Fig. 52).

In the Co-11 % sample no probe polarization anisotropy is observed despite a clear indication of the pseudogap. However, the temperature dependence of the $\Delta R/R$ magnitude in this sample is very similar to the $\Delta R/R$ magnitude of the polarization-averaged $\Delta R/R$ transients in the Co-7 % sample suggesting that the absence of the anisotropy is not due to the absence of nematic fluctuations, but due to the absence of their macroscopic ordering. The pseudogap can therefore be consistently associated with nematicity well into the overdoped region of the phase diagram.

A similar weak tetragonal symmetry breaking at high-T extending well into the SC dome region of the phase diagram has been recently observed also in F-doped Sm-1111 by high resolution synchrotron powder diffraction [39]. This suggests that the presence of the nematic fluctuations is a general property of the electron doped FeAs planes.

3.2.5.2 Determination of the electron-phonon coupling constant

To determine the relaxation time above 200 K we fit the initial part of $\Delta R/R$ transients with a finite-rise-time single exponential decay similar to Eq.(50). In agreement with the model Eq.(31) we find a clear linear T-dependence of the relaxation time in the near optimally doped Co-7 % and overdoped Co-11 % samples (Fig. 54 (b)).

At lower Co dopings, there is a clear departure from the linear T-dependence below ~ 250 K indicating that characteristic Eliashberg-function phonon frequency ω_0 rises with decreasing Co doping and/or the effects of the nematic fluctuations can not be neglected up to ~ 250 K.

Due to the optical selection rules and the multiband nature of the iron-based superconductors, it is possible that the relaxation in some bands with possible higher couplings is not directly detected in $\Delta R/R$ transients. This would happen if the interband momentum scattering was slower than the energy relaxation rate in the unobserved band(s). The slow interband scattering rate possibility is suggested by the marked pump-photon energy dispersion of the Co-7 % sample transients at high T (see Fig. 54(a)), which should be absent in the case of a very fast interband momentum scattering rate. Trying to clarify this, we estimate the upper bound for the interband momentum scattering rate, $1/\tau_{IB}$, by the scattering rate of the narrow Drude peak [139] and find that $\tau_{IB} \gtrsim 1/30$ cm$^{-1} \sim 200$ fs. This is comparable to the measured energy relaxation time (Fig. 54(b)) indicating a possibility that the estimated $\lambda\langle\omega^2\rangle$ is not well averaged over different bands. The observed pump-photon energy dispersion of the transients (see inset to Fig. 54(a)), which is negligible in the Co-0 % sample, therefore suggests that $\lambda\langle\omega^2\rangle$ is well averaged over the bands in the undoped sample. This can not be claimed (due to the significant pump-photon energy

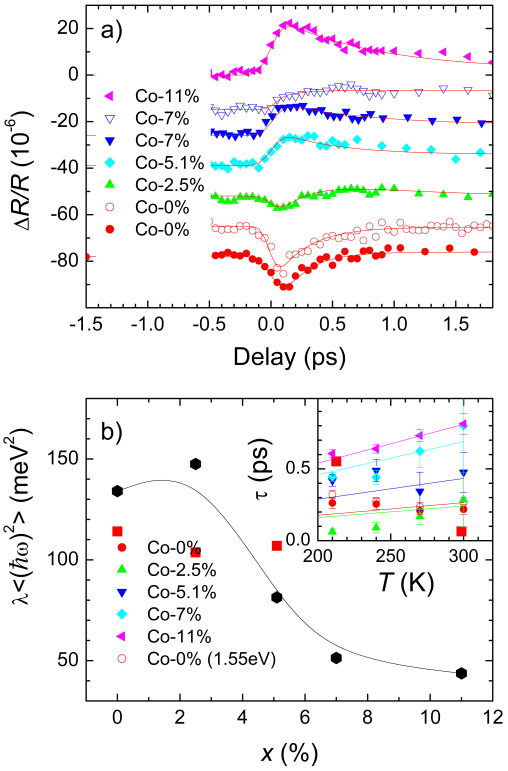


Figure 54: (a) The initial part of $\Delta R/R$ transients at 13 μJ/cm^2 pump fluence and $T = 300$ K. Open symbols correspond to the transients measured with 1.55 eV pump-photon energy in the Co-0 % and Co-7 % samples. (b) The second moment of the Eliashberg function as a function of Co-doping. Thin line is an eye-guide. Fits with Eq.(31) of the T-dependence is shown in the inset.

dispersion in the Co-7 % sample) for the samples with the Co doping well in the SC dome. Recent experiments with different pump/probe photon energies and better time resolution have, however, shown the presence of a faster relaxation component and consequently the presence of bands with $\lambda\langle\omega^2\rangle \sim 150$ meV^2 also in Co-7 % and Co-11 % samples [140].

In the Table 3 we summarize the values for λ in Ba-122 iron-based superconductors[4]. We find that in non-SC samples $\lambda\langle\omega^2\rangle$ is similar indicating a moderate electron phonon coupling constant. Moreover, λ decreases with increasing Co-doping in Ba-122 systems.

Table 3: Electron-phonon coupling parameters in Ba-122 iron-based superconductors.

Material	$\lambda\langle(\hbar\omega)^2\rangle$ (meV^2)	λ
Co-0 %	134±0.75	~ 0.34
Co-2.5 %	148±29	~ 0.36
Co-5.1 %	81±9	~ 0.2
Co-7 %	51±3	~ 0.13
Co-11 %	44±0.2	~ 0.1

[4]To calculate λ, we estimate $\hbar\omega_0 \sim 20$ meV.

3.3 Summary and conclusions

In this chapter we presented experimental results using femtosecond time-resolved optical spectroscopy in iron-based pnictides: Sm-1111, Sr-122 and Ba-122 systems.

Below T_s/T_{SDW} the $\Delta R/R$ transients in the undoped samples, are dominated by the initial single exponential relaxation. The temperature dependence of the relaxation at $T \ll T_{s,SDW}$ indicates appearance of the a QP relaxation bottleneck. The bottleneck is attributed to the partial charge gap opening with a BCS-like temperature dependence due to the band-structure reconstruction below T_{SDW}/T_s. In $Ba(Fe_{1-x}Co_x)_2As_2$ samples the relative charge gap magnitude $2\Delta(0)/k_B T_{s,SDW}$ decreases with Co-doping, consistent with a decrease of the stability of the orthorombic/SDW state (see Table 4).

In contrast, the analysis on the superconducting samples showed multicomponent relaxation. An additional SC component appears in $\Delta R/R$ transients which corresponds to the relaxation across a T-dependent superconducting gap with a BCS temperature dependence. The amplitude of the superconducting component saturates with increasing pump excitation fluence and at high-enough pump fluence a complete destruction of the superconducting state was observed. The density of the SC state destruction energy was determined from the inhomogeneous SC-state destruction model.

In Sm-1111 samples the multicomponent relaxation in SC samples strongly suggests the presence of two relatively weakly coupled electronic subsystems, one exhibiting the SC gap(s) and the other the pseudogap. From the temperature and fluence dependence of photoinduced optical reflectivity transients is clear that the presence of two electronic subsystems in the superconducting sample is not a result of a simple phase separation. The fact that no relaxation component-such as appears in the SDW phase-is seen in the SC phase appears to rule this out. The presence of two electronic subsystems therefore originates either in an intrinsic phase separation or more likely in the multiband nature of the superconducting iron pnictides.

In contrast to Sm-1111 where the relaxation dynamics suggests the presence of ungapped parts of the Fermi surface in the SC state, the absence of the two-stage relaxation in Ba-122 systems, can be ascribed to virtually clean SC gaps.

At room temperature, the transients were analyzed in the framework of electron-phonon relaxation model. In all three systems, the second moment of the Eliashberg spectral function is moderate, *i.e.* analysis indicates a moderate electron phonon coupling (see Table 4).

In Ba-122 single crystals we observe in nominally tetragonal phase a twofold rotational anisotropy with respect to the probe polarization up to ~ 200 K. The observation of unidirectional terraces on the surface of the cleaved crystals suggests, that this anisotropy might be due to the anisotropic component of the surface strain induced by the laser heating. Since this strain is weak this indicates a high susceptibility of the samples for 4-fold to 2-fold rotational symmetry breaking consistent with a nematic order parameter. The anomalous normal state behavior is therefore tentatively attributed to electronic nematic fluctuations, that persist up to ~ 200 K, and open a pseudogap in the density of states near the Fermi energy. The fluctuation region extends well above T_s in the underdoped region and across all of the investigated SC dome region of the phase diagram. Due to the surface-strain bias these fluctuations tend to align resulting in an anisotropic optical response also in the tetragonal near-optimally-doped Co-7 % sample.

Surprisingly, no clear separate anomaly is observed upon SDW formation at slightly lower T_{SDW} in underdoped samples ($x = 2.5$ % and 5.1 %). This suggests that the mechanism responsible for the pseudogap formation, nematic orbital fluctuations and partial gap opening below T_s is, despite the ubiquitous coupling to spins, not spin driven.

Lastly, in Table 4 we summarize the estimated values for SDW and PG magnitudes and electron-phonon coupling constant λ for Sm-1111, Sr-122 and Ba-122 iron-based supercon-

ductors.

Table 4: Estimated SDW and PG gap magnitudes and electron-phonon coupling parameters in iron-based superconductors.

Material	SDW gap magnitude	PG magnitude	λ
Sm-1111, undoped	$2\Delta_{SDW}/k_BT_{SDW} \simeq 5$	-	~ 0.2
Sm-1111, optimally doped	-	$2\Delta_{PG} = 120$ meV	~ 0.18[1]
$SrFe_2As_2$	$2\Delta_{SDW}/k_BT_{SDW} \simeq 7.2 \pm 1$	-	~ 0.25
Ba-122, Co-0 %	$2\Delta(0)/k_BT_s = 9 \pm 2$	-	~ 0.34
Ba-122, Co-2.5 %	$2\Delta(0)/k_BT_s = 7 \pm 2$	-	~ 0.36
Ba-122, Co-5.1 %	$2\Delta(0)/k_BT_s = 4 \pm 2$	$2\Delta_{PG} = 800 \pm 100$ K	~ 0.2
Ba-122, Co-7 %	-	$2\Delta_{PG} = 660 \pm 100$ K	~ 0.13
Ba-122, Co-11 %	-	$2\Delta_{PG} = 610 \pm 100$ K	~ 0.1

[1]Data from Ref. [140].

4 Nonthermal destruction of the superconducting state

> "A dream doesn't become reality through magic; it takes sweat, determination and hard work."
>
> Colin Powell

In this chapter we investigate the processes leading to a nonthermal condensate destruction with femtosecond laser pulses in different high-T_c materials. Firstly, we present a systematic study on the excitation pump fluence dependence of the relaxation dynamics in $YBa_2Cu_3O_{7-\delta}$ superconductor and compare it with the results in iron-based superconductors. We find that the destruction is relatively slow and inefficient in cuprates and pnictide superconductors, exhibiting a strong systematic dependence of the destruction energy U_d on T_c. In addition, we discuss a possible model based on phonon-mediated quasiparticle bottleneck mechanism, which explains observed systematics behavior in both systems.

4.1 Previous studies and motivation

Photoinduced phase transitions on the sub-picosecond timescale in superconductors [141–143] and other electronically ordered systems have attracted increasing attention in recent years, partly because of the fundamental desire to control collective states of matter with femtosecond laser pulses, partly because of potential applications in ultrafast phase-change memories, and partly because they may reveal some fundamental insight into the mechanism of high-temperature superconductivity. The rapid development of new experimental techniques, including angle-resolved photoemission, scanning tunneling spectroscopy, local structural probes and ultrashort pulsed laser spectroscopy have given important new insights into the physics of these important and theoretically challenging materials. However, the details of how absorbed photons cause a change of state on ultrafast timescales have so far not been investigated in detail.

The first experiments [13] performed in the high excitation regime on $La_{2-x}Sr_xCuO_{4+\delta}$ (LSCO) have shown that we can accurately determine the U_d destruction energy, *i.e.* energy needed for nonthermal destruction of the superconducting state. It was found that value of the destruction energy is significantly higher than the U_c^{exp} condensation energy density. These and other measurements on the cuprate superconductors [19, 20, 144] give values of U_d which are significantly larger than the experimental condensation energy U_c^{exp}, or the BCS theoretical values, opening the question of mechanism for the destruction of the condensate, the dependence of U_d on doping and on the critical temperature T_c. It is also not clear if this occasional large discrepancy between U_c^{exp} and U_d is peculiar feature of cuprate superconductors, is a consequence of a large gap in the density of states, or depends on the detailed mechanism responsible for the formation of the low-temperature ordered state.

4.2 Fluence dependence of $\Delta R/R$ transients in $YBa_2Cu_3O_{7-\delta}$

Trying to answer above-mentioned questions, we performed a systematic study of the dependence of U_d on doping and T_c in $YBa_2Cu_3O_{7-\delta}$. Optical experiments were performed on freshly cleaved underdoped $YBa_2Cu_3O_{6.5}$, $YBa_2Cu_3O_{6.6}$ and optimally doped $YBa_2Cu_3O_7$ single crystals at $T = 4$ K. The samples were prepared as it was described previously in Chapter 2 and measured with the standard pump-probe setup (section 2.2.1) at 800 nm. The Ti:sapphire laser system covered the range of excitation fluences $\mathscr{F}$ from ~ 1 to ~ 200 μJ/cm^2 at a repetition rate of 250-kHz to ensure that no heat builds up between the pulses. In addition, a wavelength of 800 nm is chosen because it is a well-understood pump-probe wavelength for investigating the superconducting (SC) and pseudogap (PG) response in pump-probe experiments (Fig. 55) and the best signal/noise ratio as determined by previous studies [13,14,18,22,23,145]. The 2-component response, PG and SC, including lifetimes, T-dependence, anisotropy and doping dependence have been previously studied at 800 nm and other pump/probe wavelengths as well, including pump/probe in the THz region [146,147]. The results of these measurements are quantitatively self-consistent, and have all been systematically discussed. The second reason for using 800 nm (1.5 eV) is that the optical constants are known more accurately at this wavelength, which improves the accuracy of the determination of the superconducting destruction energy. The reason for not using far infrared (FIR) wavelengths in the gap region is that even with transform-limited pulses, the pulses become too long to be able to distinctly detect the SC component and distinguish it from the PG. Hence THz or FIR pulses in the gap region are not suitable for our purpose.

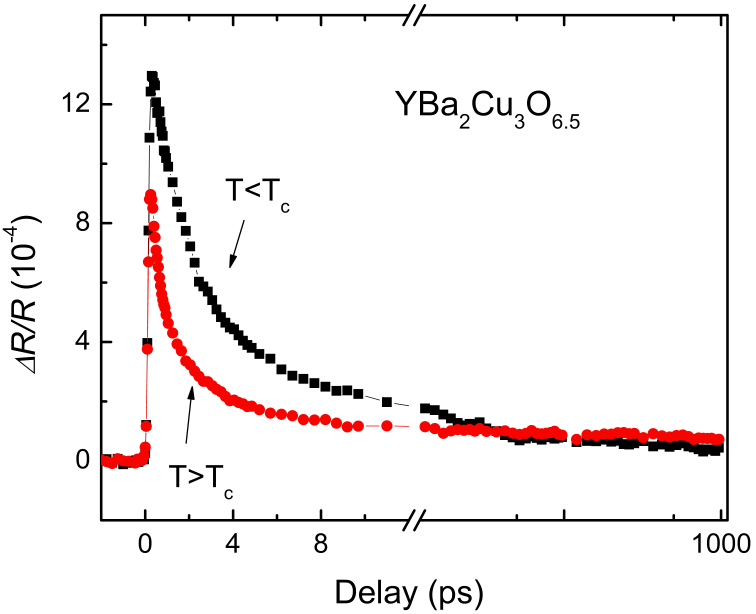


Figure 55: Reflectivity $\Delta R/R$ transients for $T < T_c$ (black squares) and $T > T_c$ (red circles) measured at $\mathscr{F} = 17.4$ μJ/cm^2 in underdoped $YBa_2Cu_3O_{6.5}$ sample.

The photoinduced reflectivity transient $\Delta R/R$ for $YBa_2Cu_3O_{6.5}$ well below T_c (4 K) and above T_c (at 68 K) are shown in Fig. 56 (b) and (c), respectively, while the net superconducting signal, obtained by subtracting the response at $T = 68$ K from the response at $T = 4$ K : $\Delta R_{sc}/R = \Delta R/R|_{T<T_c} - \Delta R/R|_{T>T_c}$ is plotted in Fig. 56 (a) for different laser pump pulse fluences. This behavior is generic, so we have shown the raw data only for one sample. The results for other YBCO samples are presented in Appendix 2. $\Delta R_{sc}/R$ shows a saturation

plateau above $\mathscr{F} \gtrsim 100\ \mu\mathrm{J/cm}^2$, which is a signature of the destruction of the SC state [13].

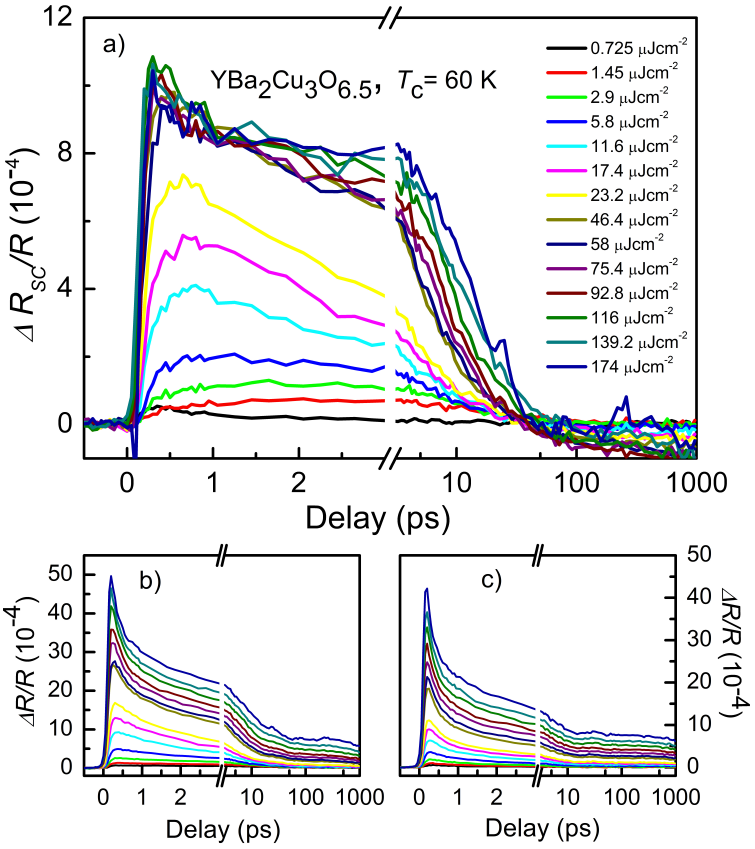


Figure 56: (a) $\Delta R_{\mathrm{sc}}/R$ for $YBa_2Cu_3O_{6.5}$ as a function of time delay for different $\mathscr{F}$. For $\mathscr{F} > 46\ \mu\mathrm{J/cm}^2$ the saturation is observed. The reflectivity $\Delta R/R$ transients at $T = 4$ and 68 K are shown in (b) and (c), respectively.

The normalized magnitude of $\Delta R_{\mathrm{sc}}/R$ for different materials (data on LSCO and CaY-BCO were included just for comparison [13]) and different doping levels as a function of $\mathscr{F}$ is shown in Fig. 57. As we can see, at low fluence $\Delta R_{\mathrm{sc}}/R$ the normalized magnitude $\Delta R_{\mathrm{sc}}/R$ is linearly dependent on $\mathscr{F}$ up to a certain threshold fluence $\mathscr{F}_{\mathrm{T}}$, whereupon it either becomes saturated or continues increasing, but with a different slope. To determine the destruction threshold fluence $\mathscr{F}_{\mathrm{T}}$ from the data in Fig. 57, we use the the Eq.(39) and (40) from the inhomogeneous excitation model [13].

It is important to take into account carrier-density dependent change of $\Delta R/R$ arising from $e-h$ asymmetry in the band structure. Therefore, we have also included a linear term in the fit to the data in Fig. 57, such that $\Delta R/\Delta R_{\mathrm{s}} = \Delta R_{\mathrm{sc}}/\Delta R_{\mathrm{s}} + \phi(\mathscr{F})$. Empirically, it was found that in LSCO [13], $\phi \simeq 0$ while in YBCO samples $\phi(\mathscr{F}) \simeq \phi_0 \mathscr{F}$, where ϕ_0 is a constant. Note that this term has no effect on the values of $\mathscr{F}_{\mathrm{T}}$ obtained from the fits to the data in Fig. 57. (As a check, $\mathscr{F}_T$ can also be directly read out as the point where $\frac{\Delta R_{sc}(\mathscr{F})}{R}$ departs from linearity).

In Fig. 58 we present the determined values of the destruction energy density $U_d = (1-R)\mathscr{F}_{\mathrm{T}}/\lambda_{\mathrm{op}}$ for wide range of doping in the YBCO superconductor as a function of T_{c}. To answer the question whether there is some general mechanism for the destruction of the SC condensate in all high-temperature superconductors, we added the previously published data for U_d obtained for iron-based pnictides [124, 148] and NbN conventional

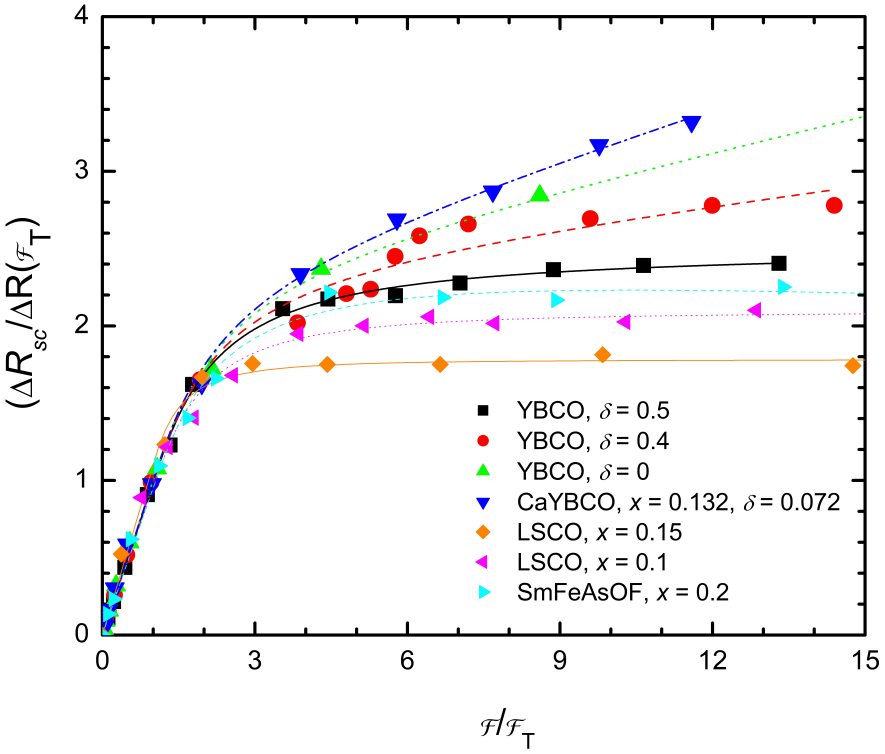


Figure 57: Normalized fluence dependence of $\Delta R_{sc}/R$ for different high-T_c materials. Thin lines are fits with Eq.(39) and (40) from Chapter 3.

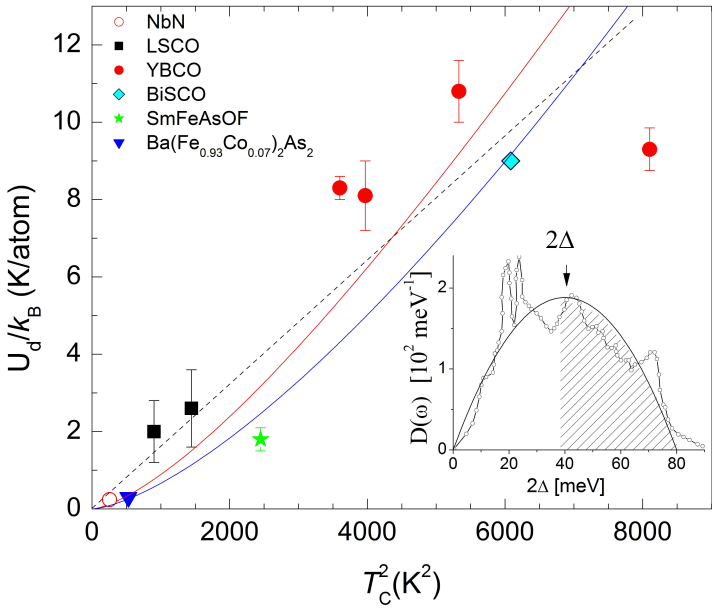


Figure 58: Destruction energy U_d as a function of T_c^2 expressed in K per planar Cu for the cuprates. The data for NbN, $SmFeAsO_{0.8}F_{0.2}$, and $Ba(Fe_{0.93},Co_{0.07})_2As_2$ are included for comparison (in K/Fe or K/Nb). The solid curve is a plot of $U_{\rm lost}$ using $D(\omega_{\rm ph})$ from Eq. (54) for YBCO (red/gray) and the iron oxy-pnictide (blue/dark gray). The dashed line is a square law $U_d = \eta T_c^2$. The inset shows the phonons with $\hbar\omega > 2\Delta$ (shaded) which can break pairs. The measured phonon density of states $D(\omega_{\rm ph})$ for YBCO (Ref. [149]) is approximated by a parabola (line).

superconductor [144]. Surprisingly, we observe a systematic increase of U_d with T_c, giving an approximate square power law dependence $U_d = \eta T_c^2$, with $\eta \simeq 1.5 \times 10^{-3} \mathrm{K}^{-2}\mathrm{atom}^{-1}$ irrespective of whether the material is overdoped, optimally doped or underdoped.

4.3 Comparison of the optically measured SC destruction energy by femtosecond laser spectroscopy and condensation energy determined by specific heat measurements in high-T_c superconductors

In Table (5) we compare U_d with the condensation energy U_c^{exp} obtained from specific heat measurements. In the cuprates, we notice a significant discrepancy between the magnitudes of U_d and U_c^{exp}. While U_c^{exp} shows a distinct asymmetry between overdoped and underdoped materials with the same T_c, U_d depends systematically on T_c irrespective of doping level. Thus U_d and U_c^{exp} show fundamentally different systematics.
After absorption of a photon, the photoexcited (PE) electrons and holes lose energy very rapidly through "avalanche" scattering with phonons on a timescale of $\tau_E < 100$ fs for YBCO and < 60 fs for LSCO [65], creating a large non-equilibrium phonon population in the process. The phonons whose energy exceeds the gap $\hbar\omega_{\mathrm{ph}} > 2\Delta$ can subsequently excite QPs from the condensate, but these recombine again and so a bottleneck occurs, in which the high-frequency phonons are in temporarily in quasi-equilibrium with QPs as described by Kusar *et al*. for LaSrCuO [13].The process eventually causes the destruction of the condensate within $0.5 \sim 1$ ps [13].

The phonons with $\hbar\omega > 2\Delta$ can contribute to the breakup of the condensate, but the *low frequency* phonons with $\hbar\omega < 2\Delta$ also created in the initial avalanche do not have enough energy to excite QPs, so do not contribute to the SC destruction process. This lost energy to low-energy phonons is:

$$U_{\mathrm{lost}} = \int_0^{2\Delta} \Delta f(\omega) D(\omega) \hbar\omega d\omega, \tag{53}$$

where $D(\omega)$ is the phonon density of states and $\Delta f(\omega) = f_{NE}(\omega) - f_E(\omega)$ is the difference between the non-equilibrium and equilibrium phonon distribution functions. $\Delta f(\omega)$ is material-dependent and depends on the electron phonon coupling, more precisely on the Eliashberg coupling function $\alpha^2 F(\omega)$, but is not a very strong function of ω [65]. To estimate the dependence of U_{lost} on T_c from Eq.(53), we assume that $\Delta f(\omega)$ is constant, and approximate the experimental $D(\omega)$ by an inverted parabola $D(\omega) = \frac{\alpha}{8}\omega(2\omega_0 - \omega)$, where α is a constant. Integrating Eq.(53), we obtain:

$$U_{\mathrm{lost}} = \alpha\Delta^3 \left[\frac{2\hbar\omega_0}{3} - \frac{\Delta}{2}\right]. \tag{54}$$

Assuming a constant gap ratio $2\Delta/k_B T_c = R$, with $R = 4$, for YBCO, $\hbar\omega_0 = 40$ meV [149] and extending $D(\omega)$ to 80 meV, as shown in the insert to Fig. 58, Eq.(54) gives the curve shown in Fig. 58. For iron pnictides, $\hbar\omega_0 \simeq 20$ [150], but the predicted variation of U_{lost} on T_c is not significantly different. We see that for the superconductor series that Eq.(54) predicts the dependence of U_d on T_c very well, which is not surprising, considering the gross features of $D(\omega)$ do not vary significantly.

Table 5: Measured $\mathscr{F}_{\mathrm{T}}$, destruction U_d and condensation U_c^{exp} energy for the cuprates, iron-based pnictides and NbN conventional superconductor. The condensation energy U_c^{exp} was determined from the specific heat measurements [68] for the YBCO and [151], [144] for the $Bi_2Sr_2CaCu_2O_{8+\delta}$ and NbN, respectively.

Material	T_{c} (K)	$\mathscr{F}_{\mathrm{T}}(\mu\mathrm{J/cm}^2)$	λ_{op}(nm)	U_d	U_c^{exp}	U_d/U_c^{exp}
$La_{1.85}Sr_{0.15}CuO_4$ (opt)	38.5	5.8±2.3	150	2.6±1.0 K/Cu	0.3 K/Cu	>8.5
$YBa_2Cu_3O_{6.5}$ (ud)	60	13.1±0.5	90	8.3±0.3 K/Cu	0.38 K/Cu	22
$YBa_2Cu_3O_{6.6}$ (ud)	63	12.1±1.3	85	8.1±0.9 K/Cu	0.45 K/Cu	18
$YBa_2Cu_3O_7$ (opt)	90	10.8±0.6	66	9.3 ±0.5 K/Cu	1.9 K/Cu	5
$Y_{0.8}Ca_{0.2}Ba_2Cu_3O_{6.9}$ (od)	73	14.3±1	75	10.8±0.8 K/Cu	1.4K/Cu	7.7
$Bi_2Sr_2CaCu_2O_{8+\delta}$ (ud)	78	16±1	124	9±0.8 K/Cu	1.8	5
$SmFeAsO_{0.8}F_{0.2}$	49.5	2.6±0.2	31	1.8±0.1 K/Fe	-	-
$Ba(Fe_{0.93}Co_{0.07})_2As_2$	23	0.43±0.04	34	0.3±0.03 K/Fe	0.15±0.02	2
NbN	16	$U_{\mathrm{v}} = 23$ mJ/cm^3		0.24 K/Nb	0.14K/Nb	1.7

The total SC destruction energy is the sum of the condensation energy and the lost energy, $U_d = U_c^{\rm exp} + U_{\rm lost}$. Since for large gap systems $U_d \gg U_c^{\rm exp}$ we have $U_d \simeq U_{\rm lost}$, so $U_c^{\rm exp}$ is thus only a small contribution to U_d explaining why the anomalous doping dependence of $U_c^{\rm exp}$ in the cuprates is not displayed by U_d.

Comparing U_d for NbN measured using the same technique (Table (5)), $U_d/U_c^{\rm exp} = 1.7$ is considerably smaller than in the cuprates, which can now be understood in terms of Eq.(53) and the insert to Fig. 58: When $2\Delta << \hbar\omega_{\rm Debye}$ almost all phonons can excite QPs, so $U_{\rm lost} \rightarrow 0$, and $U_d \simeq U_c^{\rm exp}$, in agreement with the data. For small-gap superconductors, the optical method can be used to estimate the superconducting condensation energy. The data on the two iron pnictides listed in Table (5) also seem to follow the predicted behaviour in Fig. 58.

Previously, Kusar *et al.* [13] argued that the sub-1 ps destruction of the condensate (which is present in all the materials discussed here as well) can only be described in terms of a bottleneck scenario [14], where the deposited laser energy is shared between the QPs and the bosonic glue reservoir. The observed dynamics in $La_{2-x}Sr_xCuO_{4+\delta}$, was quantitatively and self-consistently analyzed using the established Rothwarf-Taylor model [57] for QP recombination, where in the strong bottleneck regime involving phonons in the pairbreaking process, a self-consistent quantitative description of the destruction dynamics was presented. The present experimental work systematically confirms the main observation of Kusar et al, namely the large specific heat of the bosonic "glue" bath.

4.3.1 Summary and conclussions

The intention of the presented experimental data has been to present systematically - and with a high degree of experimental accuracy - the dependence of U_d on doping and on T_c in cuprates and compare them with pnictides and conventional superconductor. The result, which includes a wide range of doping for LSCO, BISCO and YBCO (including overdoped $Bi_2Sr_2Ca_{0.92}Y_{0.08}Cu_2O_{8+\delta}$) reveals a square power-law relation between U_d and T_c. The significance of the systematically large $U_d/U_c^{\rm exp}$ values for the QP recombination mechanism and consequently also in the pairing interaction is clear: only the phonon bath has sufficient specific heat capacity to absorb U_d, implying also that it is the phonon "glue" which needs to be heated in order to destroy the condensate. The specific heat of the magnetic subsystems on the other hand appears to be far too small to account for the large observed values of $U_d/U_c^{\rm exp}$. We emphasize that the square power-law dependence of U_d on T_c does not imply that BCS theory is applicable to high-T_c cuprates. In fact, the data clearly show that the cuprates are set apart from conventional superconductors, such as NbN and to some extent also the pnictides in terms of the amount of energy needed to destroy the superconducting condensate. In another words, from the femtosecond laser spectroscopy point od view both cuprates and pnictides have several common properties: an appearance of the bottleneck in the relaxation, the magnitude of the temperature-independent gap (pseudogap) is decreasing with increasing doping and similar QP relaxation mechanism based on a phonon "glue" bath. Therefore, the present observations gained from the systematic femtosecond laser spectroscopy study represent a very clear and stringent requirement for any prospective theory of high-temperature superconductivity.

5 Bistable switching to a new hidden state of matter by femtosecond laser pulse in 1*T*-TaS_2 dichalcogenide

> "I learned the value of hard work by working hard."
>
> Margaret Mead

Broken symmetry plays a key role in understanding the properties and behavior of many solid-state systems. To study the symmetry breaking phase transitions (SBPT) is not so easy task, since they occur very fast or they are sometimes hard to repeat. In another words, studying SBPT in solid-state systems, such as ferromagnets and superconductors, however, is much more challenging task due to the extremely short timescales over which the individual particles and collective excitations relax during the transition [47]. First study of high-time-resolution symmetry breaking phase transition was performed on $TbTe_3$ charge-density wave system [25] was a strong motivation to extend the research to 1*T*-TaS_2 charge-density wave system.

This chapter is organized as follows. Firstly, we introduce a new write-pump-probe technique used for quenching the 1*T*-TaS_2 system into high symmetry state and monitor the temporal recovery of the system with a standard pump-probe sequence. A detailed study on bistable optical switching to a new hidden state of matter in 1*T*-TaS_2 will be presented where at the end we discuss some possible applications.

5.1 Write-pump-probe technique

With this technique, we quench the system with a powerful laser pulse named write (W) into a high-symmetry state. The temporal recovery is monitored by measuring the reflectivity $\Delta R/R$ transients with a standard pump-probe sequence (Fig. 59). The pulse train of 50 fs laser pulses was split into three components: write (W), pump (P) and probe (Pr) beam. All three components were at photon energy $\hbar\omega = 1.5$ eV. The write fluences were $\mathscr{F}_{\mathrm{W}} = 13$–$3000\ \mu\mathrm{J/cm^2}$ where the pump and probe fluences were kept constant during all measurements and estimated to be $\mathscr{F}_{\mathrm{P}} = 10\ \mu\mathrm{J/cm^2}$ and $\mathscr{F}_{\mathrm{Pr}} = 0.5\ \mu\mathrm{J/cm^2}$, respectively. The beam diameters were found to be 102 ± 2, 83 ± 1 and $40\pm1\ \mu$m for the W, P and Pr beam, respectively. In order to quench the system with a single W pulse, we employ a signal generator synchronized to the amplifier in our experimental setup. The probe polarization was orthogonal to the polarization of W and P beam, which were parallel to each other. The reflectivity signal detector was locked to the modulation of the pump at $f_{\mathrm{P}} = 2$ kHz. Optical measurements were performed on freshly cleaved 1*T*-TaS_2 single crystals at temperature of 30 K.

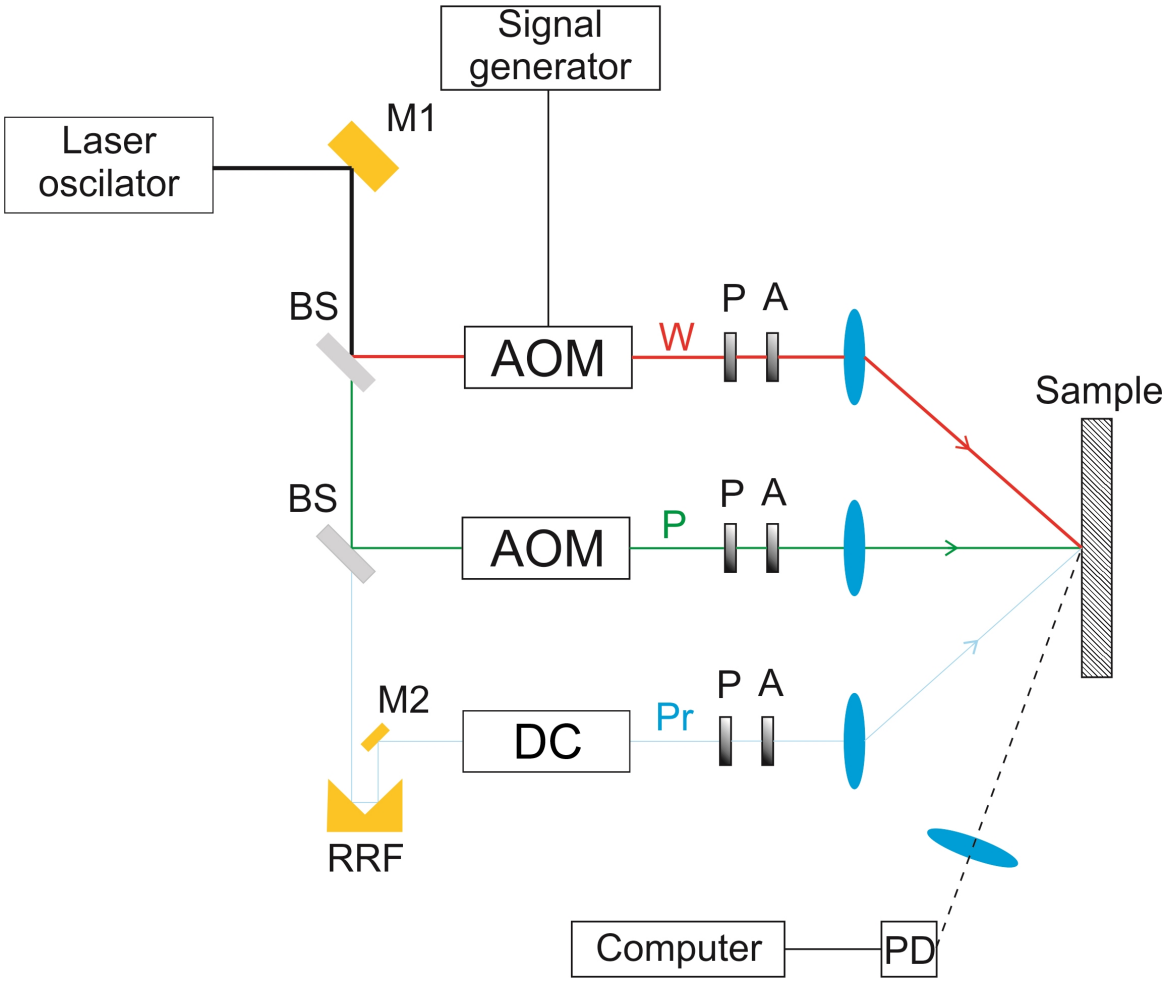


Figure 59: A schematic of a write-pump-probe technique. M1-M2:Mirrors, BS:Beamspliter, AOM:Acousto-optical modulator, P:Polarizer, A:Attenuator, PD:Photodiode, RRF:Retroreflector, DC: dispersion compensator. The red, green and blue line denotes the write, pump and probe beam, respectively.

5.2 Observation of a new state in 1T-TaS_2

In Fig. 60 (a) we present a systematic fluence dependence of the raw $\Delta R/R$ transients after quenching with a train of W pulses and recorded with a pump-probe sequence, where $\mathscr{F}_p = 10\ \mu J/cm^2$. We observe oscillations in the reflectivity due to the coherent excitation of the phonons and collective modes. The fast Fourier transformation (FFT) spectrum of the coherent phonon oscillations at low pulse energies is consistent with previous reports [27], showing amongst other phonon modes a very strong mode at 2.46 THz, corresponding to the collective amplitude mode (AM) of the commensurate phase of 1T-TaS_2 at 30 K. In addition, there are three other phonon modes at 2.1, 3.2 and 3.85 THz.

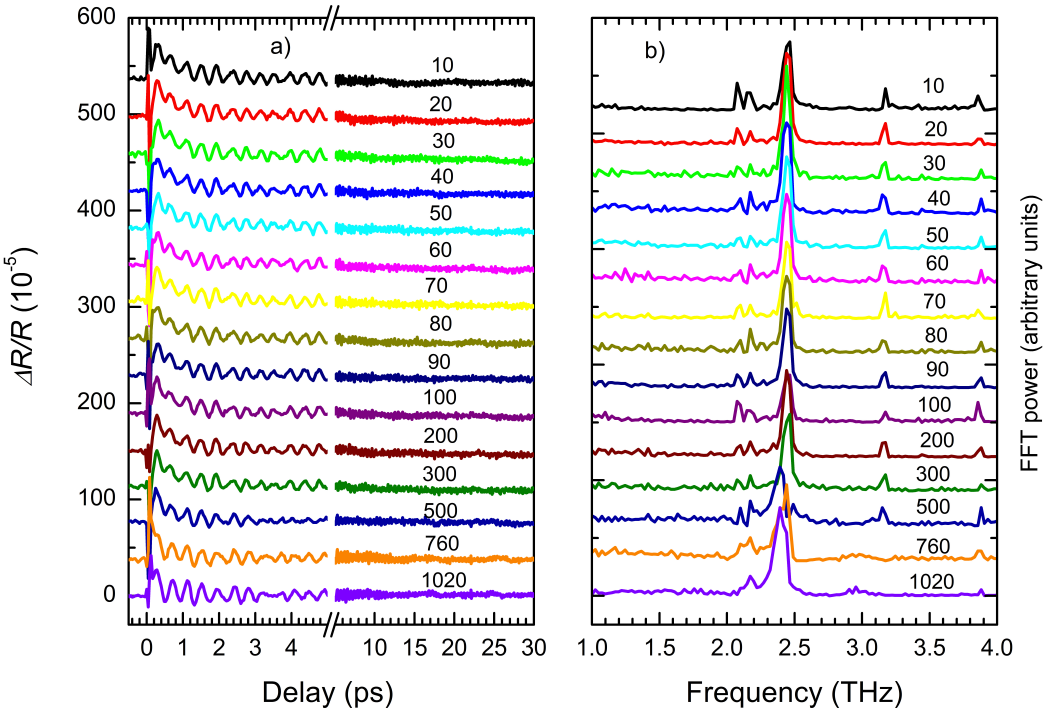


Figure 60: (a) Raw $\Delta R/R$ transients of 1T-TaS_2 in CCDW phase recorded with 10 $\mu J/cm^2$ pump-probe sequence after quenching with a train of W pulses. (b) Fast Fourier transform of the raw $\Delta R/R$ transients in (a). Spectra are vertically shifted for clarity. The W pulse fluences are expressed in $\mu J/cm^2$.

We can clearly see that after illumination with the $\mathscr{F}_W = 500\ \mu J/cm^2$ train of Write pulses there are notable changes of the spectrum (Fig. 60). The oscillations have larger amplitude, but the exponential transient is smaller. The most notable change in the spectrum is the complete disappearance of the AM at 2.46 THz and an appearance of a new mode at 2.39 THz (Fig. 61). The other phonon modes also show small changes: the intensity of modes at 3.1 THz and 3.85 THz are reduced and some additional spectral intensity appears in the region between 2 and 2.5 THz. We denote this photoexcited state as p-TaS_2 and observed shift of the AM as switching the system ON.

Similar behavior was also observed at $T = 68$ K (Fig. 62). The spectrum of the photoexcited p-TaS_2 state remains unchanged as long as the sample temperature remains below $T_p \simeq 100$ K.

In order to check whether the AM shift is possible at higher temperatures, we have performed experiments at 120 and 150 K (see Fig. 63). Unfortunately, attempts to switch the system ON into the p-TaS_2 state have failed.

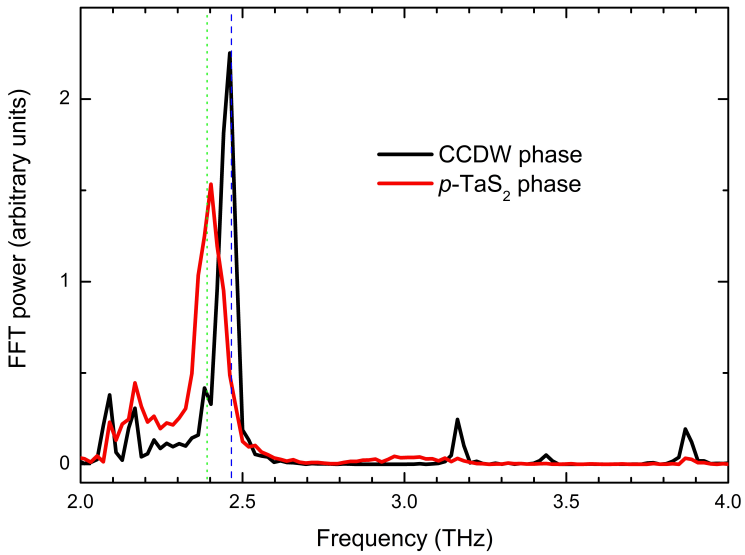


Figure 61: Fast Fourier transform of $\Delta R/R$ transients in $1\,T$-TaS_2 in CCDW phase recorded with pump-probe sequence before (black line) and after quenching (red line) with a train of W pulses, measured at $T = 30$ K. We can clearly see a complete disappearance of the AM at 2.46 THz and the appearance of a new mode at 2.39 THz. Blue dashed and green dotted lines are an eyeguide for AM at 2.46 and 2.39 THz, respectively.

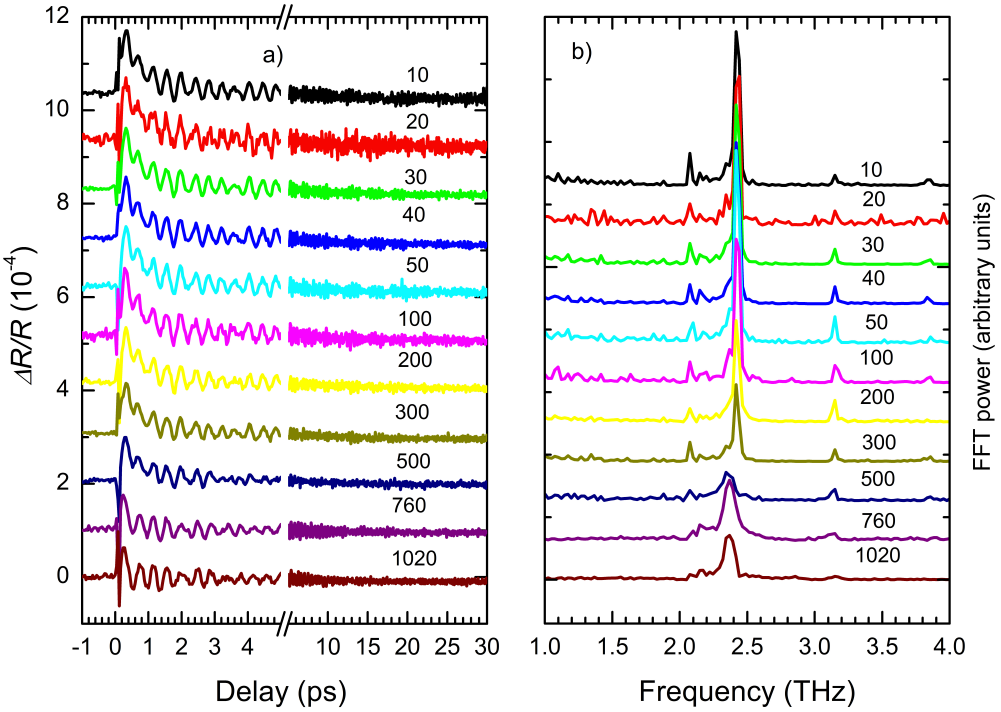


Figure 62: (a) Raw $\Delta R/R$ transients of $1\,T$-TaS_2 in CCDW phase recorded with pump-probe sequence after quenching with a train of W pulses, measured at $T = 68$ K. (b) Fast Fourier transform of the raw $\Delta R/R$ transients in (a). We can clearly see a complete disappearance of the AM at 2.46 THz and the appearance of a new mode at 2.39 THz. Spectra are vertically shifted for clarity. The W pulse fluences are expressed in μJ/cm^2.

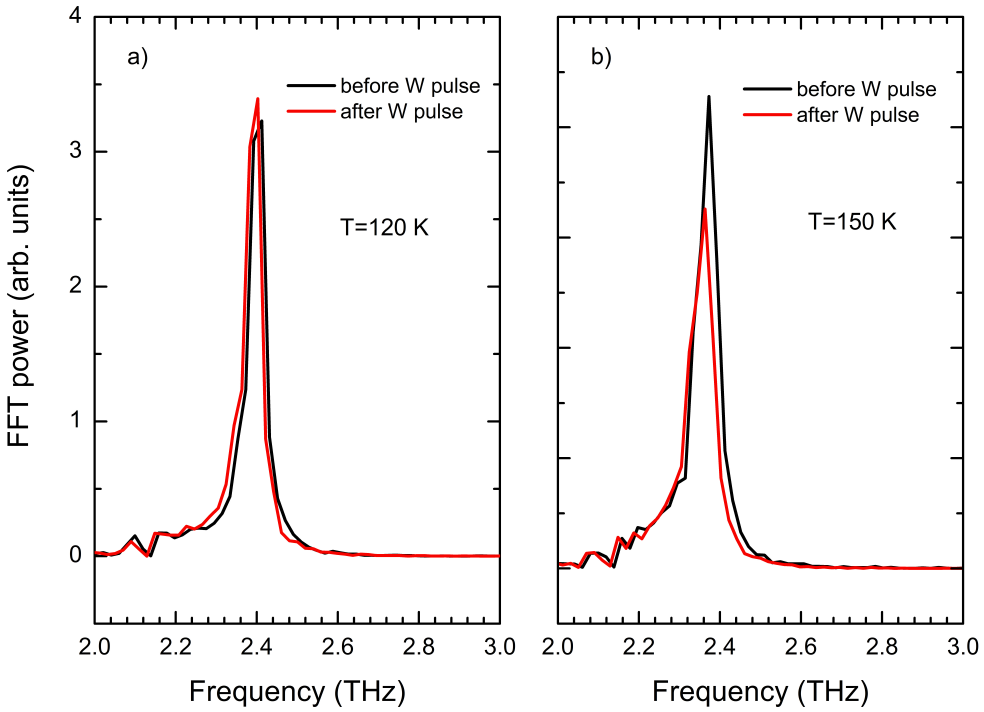


Figure 63: Coherent phonon mode spectra of 1T-TaS_2 recorded before (black line) and after (red line) a train of W pulses at $\mathscr{F}_W = 500\ \mu J/cm^2$ at (a) $T = 120$ K and (b) $T = 150$ K.

Once we know that a train of W pulses at $\mathscr{F}_W = 500\ \mu J/cm^2$ switches the system into a p-TaS_2, we wanted to check whether a single W pulse can also quench the 1T-TaS_2 system. For that purpose we have performed systematic measurements on switching to p-TaS_2 state with a single W pulse as a function of W pulse energy $\mathscr{F}_W$ and duration τ_W. The results are presented in Fig. 64 (More detailed raw data is presented in Fig. 76 in Appendix 2). With increasing the W pulse length the threshold for switching increases. It was found that a single W pulse at $\mathscr{F}_W \sim 1\ mJ/cm^2$ and $\tau_W = 50$ fs is enough to quench the 1T-TaS_2 system to a new p-TaS_2 state.

To summarize, the switching to the p-TaS_2 state is possible either by a single W pulse at $\mathscr{F}_W \sim 1\ mJ/cm^2$ or by the $\mathscr{F}_W = 500\ \mu J/cm^2$ train of W pulses[5]. Please note that in both cases the W pulse length is $\tau_W = 50$ fs.

Switching the 1T-TaS_2 system into a new p-TaS_2 state was followed by an experimental challenge: to revert back the p-TaS_2 to the CCDW state (virgin state). We denote switching back to the CCDW state as switching OFF. For this purpose we have performed series of measurements including photoillumination of p-TaS_2 state with different pulse lengths τ, number of pulses (Fig. 65), fluences $\mathscr{F}$ and base temperatures (see also Fig. 77 in Appendix 2).

We found two experimental methods which revert the p-TaS_2 system back to the CCDW phase. First, so-called "thermal" way of switching OFF into the CCDW phase is achieved with warming up of the p-TaS_2 at T_p above 100 K. From Fig. 66 it can be seen that the FFT spectrum of the coherent phonon oscillations after warming up to $T_p = 100$ K and slowly cooling down to $T = 30$ K is identical to the FFT spectrum in the CCDW phase before quenching with a W pulse (the AM at 2.46 THz appears in the spectrum).

[5]Just for the record, on a time scale this "train of W pulses" lasted for approx. 45 min., *i.e.* our sample was exposed to photoillumination by W beam for $\sim$45 min.

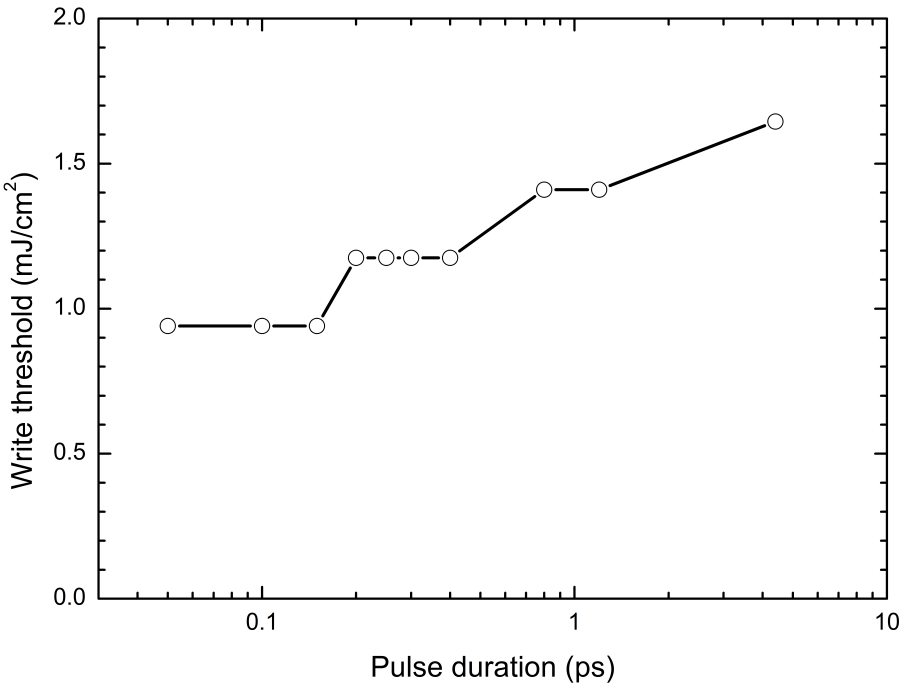


Figure 64: Systematic measurement of the W pulse fluence threshold $\mathscr{F}_W$ as a function of the pulse duration τ_W. It was found that a single W pulse at 1 mJ/cm^2 and $\tau_W = 50$ fs is enough for switching to a p-TaS_2 state.

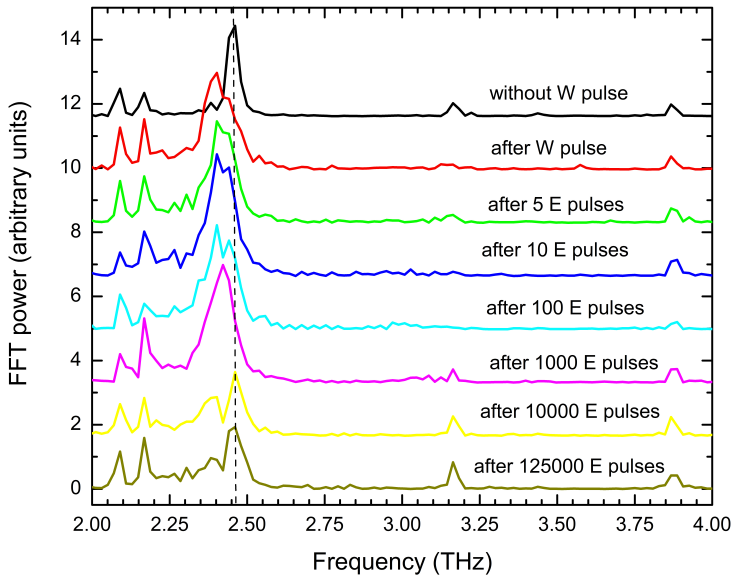


Figure 65: Switching OFF with a different number of E pulses each at $\mathscr{F}_E = 2$ mJ/cm^2. It was found that 10^4 E pulses at $\tau_E = 50$ ps and $\mathscr{F}_E = 2$ mJ/cm^2 are enough to revert back the $1T$-TaS_2 system. Dashed line refers to AM at 2.46 THz.

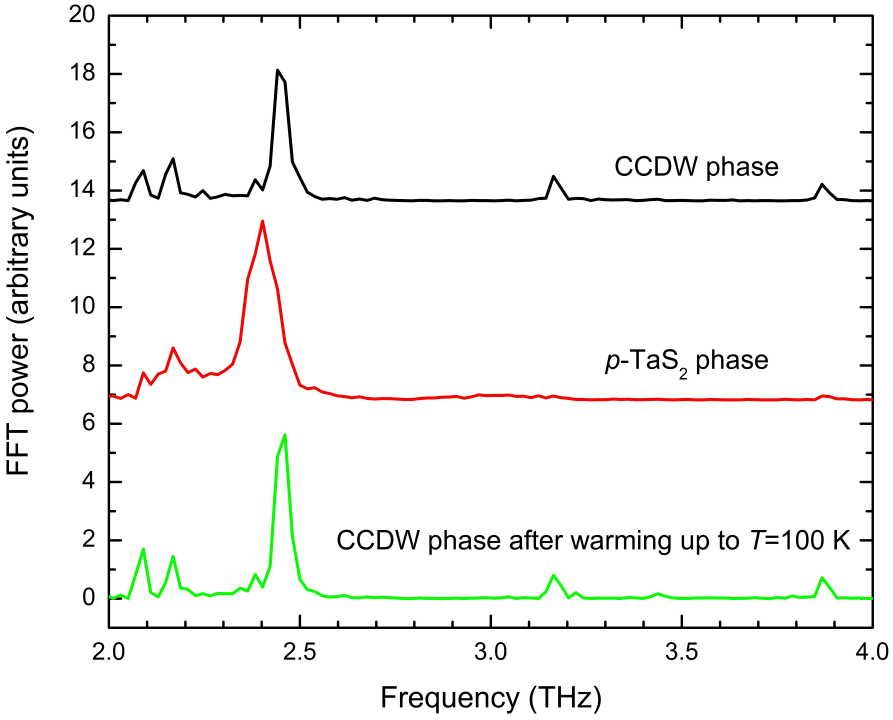


Figure 66: An example of the coherent phonon mode spectra of 1 T-TaS_2 in the CCDW (virgin state), p-photoinduced and CCDW phase after warming up at $T = 100$ K. The spectra were recorded with pump-probe sequence. We can clearly see that after warming up the AM at 2.46 THz reappears in the spectrum.

The second method is based on switching the system OFF by employing an additional "Erase" (E) beam, derived from the uncompressed amplifier output bypassing the compressor. This so-called "optical" OFF method is based on a photoillumination of p-TaS_2 system with a 40 ms pulse train of 10^4 uncompressed 50 ps pulses at $\lambda = 800$ nm where the energy of each pulse was $U_E \simeq 2$ mJ/cm^2. Switching to OFF state was not successful with a single E pulse at the highest achievable Erase energy $U_E = 4$ mJ/cm^2 (see Fig. 77 in Appendix 2). From Fig. 67 we can clearly see that a train of E pulses switches the system OFF completely: AM at 2.46 THz has completely recovered while the AM at 2.39 THz has completely disappeared. Many measurements have shown that several ON/OFF cycles can be performed this way (Fig. 68).

Appearance and disappearance of AM at 2.46 and 2.39 THz during the ON/OFF switching is accompanied with a change in the reflectivity R, monitored by measuring the reflected beam. From the plot of the raw normalized reflectivity data in ON (the red line in Fig. 69) and OFF (the green line in Fig. 69) state we can see the R difference varying between 3 and 10 %, depending on the spot on the sample (see Fig. 69).

In addition, we observe a change in the direct-current (DC) resistance in the p-TaS_2 state [152]. Two golden contacts with 10 μm gap in between were deposited by nanolithography on a thin layer 1 T-TaS_2 with thickness $d = 20$ nm. The DC resistance was measured with Keithley-6430 source measure unit at source current I in the range ± 1 μA during ON/OFF switching. There was $\sim$ 75 % decrease in resistance after quenching with a W pulse, *i.e.* switching to p-TaS_2. Subsequently, the resistance saturates with increase of number of W pulses as shown in the inset to Fig. 70.

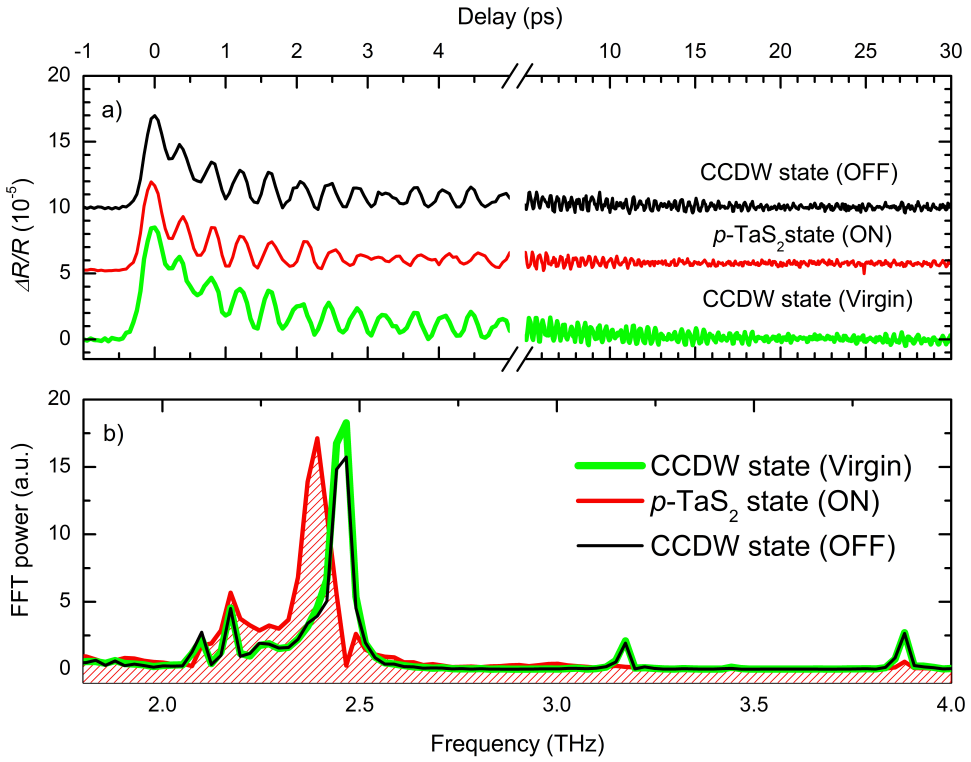


Figure 67: Transient reflectivity (a) and collective mode spectra (b) in the CCDW (virgin), p-TaS_2 (ON) and the CCDW (OFF) state. The scans in (a) were shifted vertically for clarity.

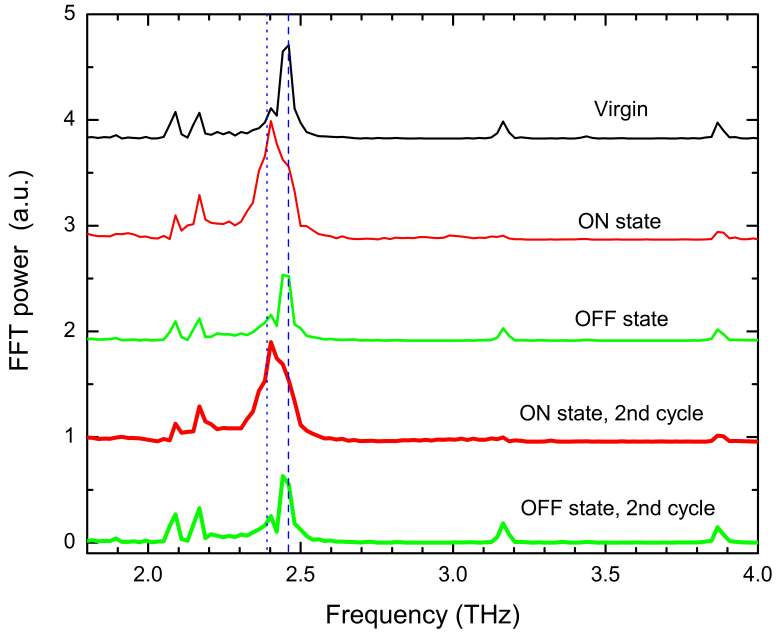


Figure 68: Collective mode spectra in the virgin, ON and OFF state during a sequence of alternating W and E pulse sequences. The spectra were shifted vertically for clarity and recorded with pump-probe sequence. Blue dashed and dotted line are an eyeguide for AM at 2.46 and 2.39 THz, respectively.

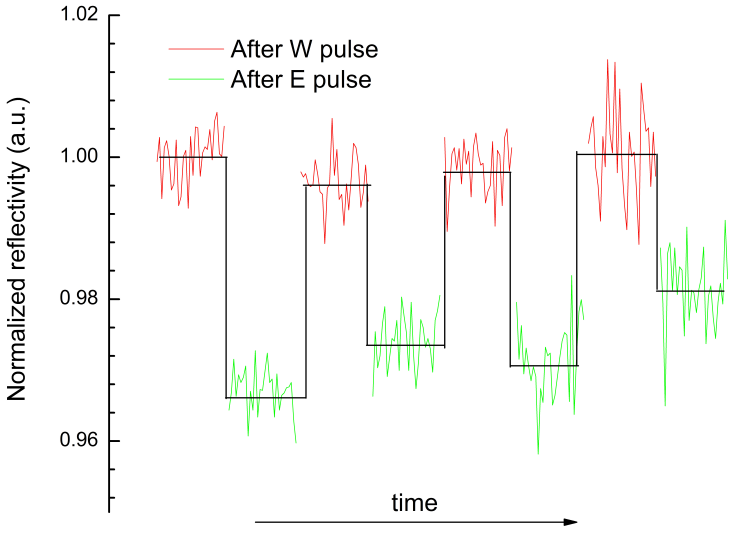


Figure 69: Normalized reflectivity at 800 nm of the sample recorded by a photodiode during a sequence of alternating W and E pulse sequences.

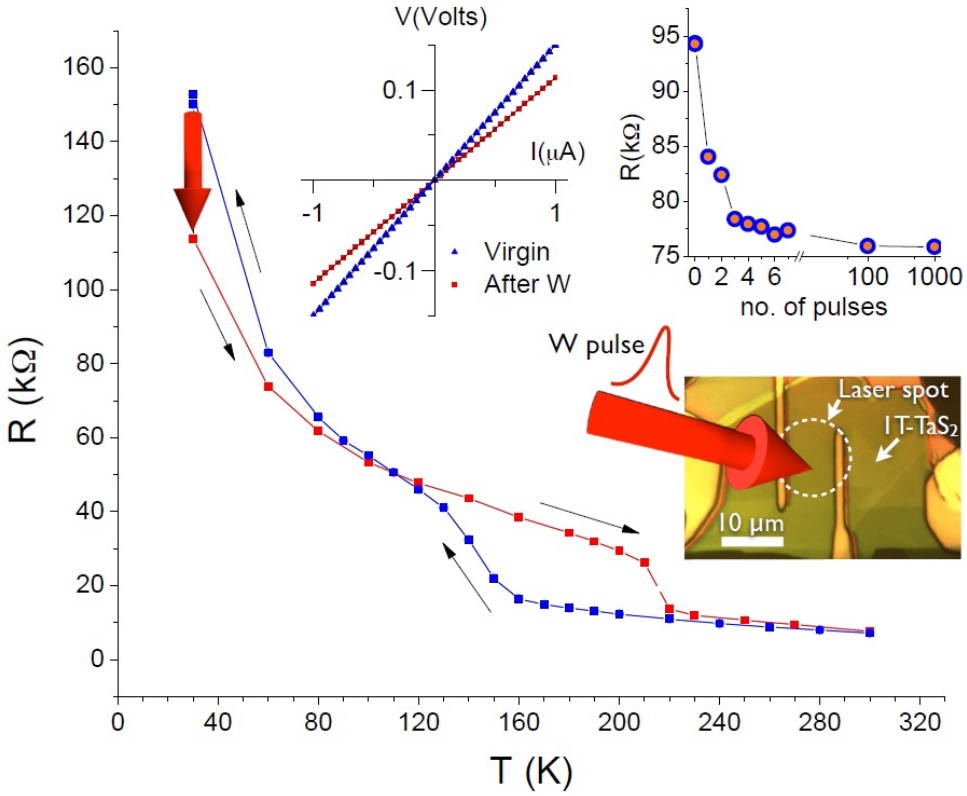


Figure 70: Resistivity switching by 50 fs pulses on a 20 nm thick 1 T-TaS_2 sample. The sample and contacts are in the insert. The T-dependence of resistance r before and after switching. The inserts show the I-V curve and the dependence of r on the number of 50 fs pulses at 30 K with 1 mJ/cm^2 W pulse. Adopted from Ref. [152].

In conclusion, let us emphasize some remarkable characteristics of the switching process:

1. After photoexcitation with a single W pulse, the p-TaS_2 state is spontaneously created as long as the systems is below $T_p = 100$ K;
2. The switching occurs with short pulses and the switching efficiency decreases with increasing τ_W;
3. The p-TaS_2 state is completely stable until erased, or heated above $T_p = 100$ K;
4. The optical erase process requires 10^4 intense 50 ps laser pulses.

5.3 Theoretical consideration for p-TaS_2 state formation

To understand the observed mechanism for switching, the time-evolution of the electronic and lattice temperatures T_e and T_L in the first 4 ps after the photoexcitation should be calculated using the standard two-temperature model [64, 66, 153]:

$$\gamma_e T_e \frac{dT_e}{dt} = -\gamma_L(T_e - T_L) + P(T)$$
$$C_L \frac{dT_L}{dt} = \gamma_L(T_e - T_L) \quad (55)$$

Here, $P(t) = (1-R)\frac{E_0}{\sqrt{2\pi}\omega}\exp\left[-\frac{(t-t_0)^2}{2\omega^2}\right]$ is normalized W pulse intensity, where $\tau_W = 2\sqrt{2\ln 2}\omega$ is W pulse width, $\gamma_L = 3\hbar_{e-p}\langle\omega^2\rangle\gamma_e/\pi k_B$ [66] and $\gamma_e = 4.2$ mJ/molK^2 is electronic specific heat coefficient [42]. $C_L(T)$ is the lattice specific heat and $R = 0.6$ is reflectivity at 1.5 eV [154]. The evolution of $T_e(T)$ and $T_L(T)$ as a function of $\frac{\mathcal{F}_W}{\lambda_{op}}$ and τ_W was obtained using a electron-phonon interaction λ_{e-p}~0.25, a Debye model fit of the experimental [155] $C_L(T)$ and the phonon frequency $\langle\omega^2_{ph}\rangle$~10 THz^2. The estimated electronic and lattice temperatures $T_e(T)$ and $T_L(T)$ after 50 fs W pulse are shown in Fig. 71. After a quench with single W pulse at energy density threshold $\mathcal{F}_W = 1$ mJ/cm^2 (labeled by black dashed line in Fig. 71 (a)) the electronic temperature $T_e(T)$ increases up to 1200 K where the lattice temperature $T_L(T)$ (indicated by lower sheet in blue) barely reaches the temperature of the NCCDW-CCDW transition (180–220 K).

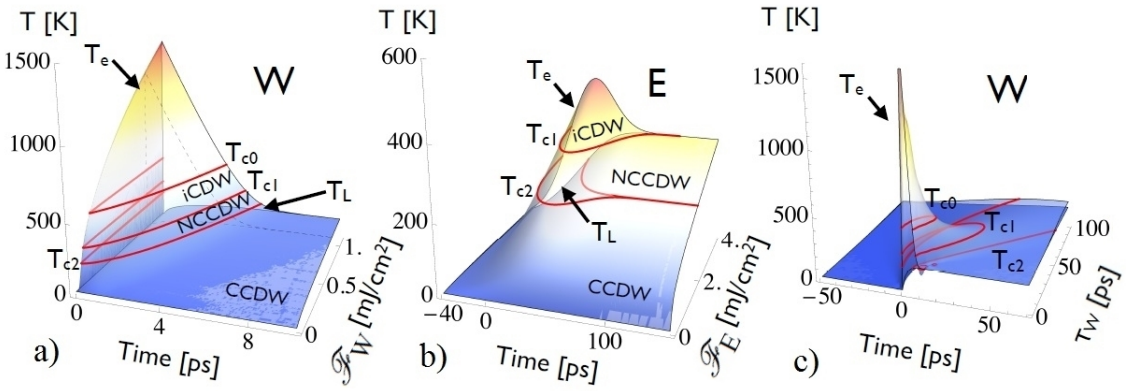


Figure 71: The calculated time evolution of T_e and T_L as a function of (a) $\mathcal{F}_W$ and (b) $\mathcal{F}_E$ energy for τ_W=50 fs using the two-temperature model. The dashed black line in (a) is the experimental threshold value of $\mathcal{F}_W$ for switching into the p-TaS_2 state. The red lines indicate the transition temperatures $T_{c0} = 500$ K, $T_{c1} = 350$ K and $T_{c2} = 180$–210 K, respectively. (c) T_e and T_L as a function of time for different pulse lengths τ_W. The red lines indicate the same three transition temperatures as in (a) and (b). Adopted from Ref. [153].

In Fig. 71 (c) we present $T_e(T)$ and $T_L(T)$ as a function of τ_W, calculated at U_W threshold. In addition, we can clearly see that a very fast quench of $T_e(T)$ through 500 K → 180–220 K is accomplished only for $\tau_W \leq 4$ ps. At longer τ_W the switching is either slower or not possible. Attempts to switch OFF with a single E pulse at ~4 mJ/cm^2 have failed (see Fig. 77 in Appendix 2).

We compare the coherent phonon spectra of p-TaS_2 with the Raman spectra of known R-TaS_2 polytypes ($R = 1T$, $2H$, $4Hb$) in Table (6) and find that there is no known R-TaS_2 polytypes below 100 K to which we can attribute the p-TaS_2 state [50, 52, 156–158].

Table 6: Frequencies of the observed modes in the low frequency region for different polytypes of TaS_2 and their different phases. Note that the laser power is significantly lower in time-resolved P-p spectroscopy than in Raman spectroscopy, which can explain the slightly higher frequencies of the coherent phonons compared to the Raman spectra. All energies are in wavenumbers (cm^{-1}). The numbers in parenthesis for the coherent phonons are in THz.

$1T$-TaS_2	p-TaS_2	$1T$-TaS_2 CCDW	$1T$-TaS_2 NCCDW, $T_c = 310$ K	$1T$-TaS_2 ICCDW, $T_c = 370$ K	$2H$-TaS_2	$4Hb$-TaS_2	$1T$-TaS_2 CCDW
coh. ph.	coh. ph.	Raman	Raman	Raman	Raman	IR	
						19	
					27		
	42 (1.27)						
					48		48
							54.5
		56					
	59 (1.79)						58.5
		62					
	63.8 (1.93)						63
———			64			64	
							66.5
		68		68			68
68.9 (2.089)	68.9 (2089)						
71.5 (2.167)	71.5 (2.167)	71.5				72	72
75.6	75.3	75			75		
		78				78	
	78.9 (2.39)						
							80
81.2 (2.46)							
		82					
		84					
		87.5				88	
		92.5					89
	96.35	95				96	
	99.7	98.5					100
		103				103	
104.4 (3.165)							
		106					106
		110					
		114					
		119					
							121
		124					
		127					
127.9 (3.875)	127.9 (3.875)						
						129	129
							134

We propose a model for switching in $1T$-TaS_2 based on Kibble-Zurek mechanism [159, 160] with a topological stabilization. According to this model it is believed that our Universe has evolved from the initial hot Big Bang followed by a series of symmetry-breaking phase transitions which had consequently led to the formation of topological defects such as monopoles, strings or domain walls [160]. In another words, Kibble-Zurek model explains how system evolves from a state of high-symmetry to broken symmetry. Therefore it is not of relevance just to cosmology but also to condensed-matter systems as it was shown in the previous reports [25].

A single W pulse excites the $1T$-TaS_2 system into a intermediate state i-TaS_2, followed by rapid decay to p-TaS_2 state instead of CCDW state (see Fig. 72). In Fig. 72 we sketch the configurational energy diagram for the switching between the CCDW and $p-TaS_2$ state. The optical excitation excites the system into an excited intermediate state i-TaS_2 (red arrow), which relaxes into the hidden state p-TaS_2 instead of the CCDW state (blue arrow). The transition back to the CCDW state proceeds after an E pulse sequence (green arrow).

One possible explanation why only one 50 fs pulse switches $1T$-TaS_2 into p-TaS_2 state, arises from the fact that the band structure of $1T$-TaS_2 has a strong $e-h$ asymmetry [161, 162], hence it is possible to produce photodoping effect on picosecond timescale. First

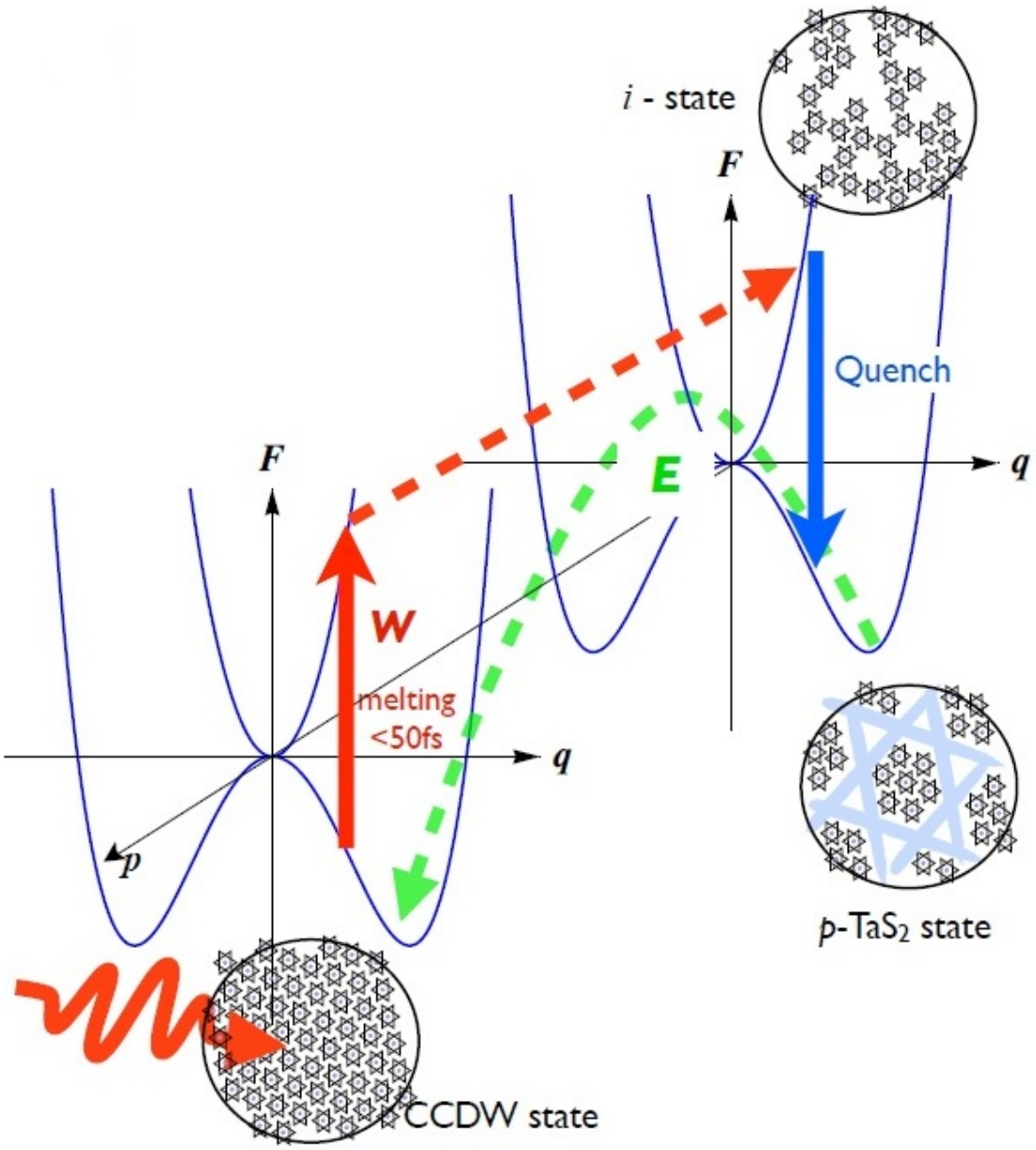


Figure 72: The configurational energy diagram for the switching between the CCDW state and the p-TaS_2. The optical excitation excites the system into an excited intermediate state i-TaS_2 (red arrow), which relaxes into the hidden state p-TaS_2 instead of the CCDW state (blue arrow). The transition back to the CCDW state proceeds after an E pulse sequence (green dashed arrow).

experiments on laser melting have shown a shift of the chemical potential $\Delta\mu \simeq 60$ meV within 50 fs. During the temporal evolution of $\mu(t)$, the Fermi surface is changing, leading to a time-dependence of the wavevector nesting conditions. As a result of a dynamically changed vacuum, the self-organized ordered stable structure (cannot be reached by adiabatic route) is formed. As we have mentioned before, a single E pulse at ~ 4 mJ/cm^2 energy cannot switch the p-TaS_2 system to OFF state, even though T_e increases up to ~ 600 K. In accordance with previously reported depolarization mechanism in current-induced depinning studies in $NbSe_3$ [163, 164], a train of pulses is required for erasing.

To gain insight into the switching process, an additional theoretical study is required. However, at the time of writing this thesis, the trajectory to p-TaS_2 and revert back to the CCDW phase is still under intensive theoretical study, consisted of simulations and modeling with a time-dependent Ginzburg-Landau theory [54].

5.4 Possible application as ultrafast memory elements

In 2008, the Hewlett Packard company presented the first phase-change memory element [165]. It is a type of non-volatile computer memory based on the memristor. The central element is chalcogenide glass, which can be switched between crystalline and amorphous state by an electric current passing through. The crystalline and amorphous states of chalcogenide glass have dramatically different electrical resistivity. The amorphous, high resistance state represents a binary 0, while the crystalline, low resistance state represents a 1. Chalcogenide is the same material used in re-writable optical media (such as CD-RW and DVD-RW). In those instances, the material's optical properties are manipulated, rather than its electrical resistivity, as chalcogenide's refractive index also changes with the state of the material.

Up to date, many new kinds of phase-change memory have been reported [9–11]. More recently, a reports on ultrafast switching of domain structures by laser pulses in different magnetic systems have been published [25, 166–168].

Described optically switching mechanism in $1\,T$-TaS_2, makes it a perfect candidate for a new phase-change memory element. Even though, the highest working base temperature is 68 K, with certain functionalization such as pinning or doping of $1\,T$-TaS_2 we might reach a higher temperature. Of course, next step is to repeat write-pump-probe experiment in different CDW materials. The materials such as $2H$-$TaSe_2$, $4Hb$-TaS_2, $2H$-TaS_2, etc. being in a form of single crystal or a thin film, might surprise us with astonishing experimental results (for example, higher working temperature close to a room temperature), thus making them suitable candidates for a new phase-change memory element.

5.5 Summary and conclusions

With the implementation of a new state-of-art write-pump-probe pulse technique, we quench the system to a new photoinduced p-TaS_2 state. The p-TaS_2 state has been reported for the first time and can be reached only with a single 50 fs laser pulse. The recovery to a CCDW state is achieved with a train of 10^4 long 50 ps pulses. The ON/OFF switch is accompanied with a change in DC resistance and reflectivity. Described bistable optical switching in $1\,T$-TaS_2 system might be a starting point for a development of a new ultrafast memory elements.

6 Conclusions

> "Try not to become a man of success. Rather become a man of value."
>
> Albert Einstein

Femtosecond laser spectroscopy was applied for the relaxation dynamics study in two different groups of high-T_c systems: iron-based pnictides and cuprates.

In undoped SmFeAsO, $SrFe_2As_2$ and $BaFe_2As_2$ pnictides, exhibiting a SDW ordering, the relaxation dynamics can be characterized with a single exponential component. From temperature dependence of $\Delta R/R$ in the low-excitation pump regime, we observed a remarkable slowing down of the relaxation at structural/SDW transition temperature. Below T_s/T_{SDW} a relaxation bottleneck appears as a consequence of the opening of a single-charge gap at T_s/T_{SDW} with a BCS-like temperature dependence. The magnitude of the gap decreases with increasing doping, which is consistent with a decrease of the stability of the orthorombic/SDW state. To determine the electron-phonon coupling constant we performed pump-probe measurements at room temperature. From the relaxation time the electron-phonon coupling constant λ was estimated. In all three studied undoped pnictides, λ has similar values in the range 0.2–0.3, indicating a moderate electron-phonon coupling.

In contrast to undoped, the superconducting pnictides showed a multicomponent relaxation dynamics. Fluence dependence measurements performed at $T = 4$ K revealed a saturation of the SC component which indicates a destruction of the SC state. Using an inhomogeneous SC-state destruction model, we estimate the destruction energy density U_d. Below T_c the $\Delta R/R$ transients were analyzed in the framework of the high-frequency limit of the Mattis-Bardeen formula. The relatively slow recovery of the SC state in Ba-122 system indicates virtually clean SC gaps. However, this is not true for Sm-1111, where the two stage relaxation has been detected.

Above T_c the $\Delta R/R$ transients indicate a bottleneck due to the relaxation the pseudogap. The magnitude of the estimated pseudogap is in a good agreement with pseudogap values obtained with tunneling experiments or T-dependence of the Knight shift. In addition, in Co-doped Ba-122 single crystals, the magnitude decreases with increasing doping.

The most striking experimental result was the observation of the twofold rotational anisotropy with respect to the probe polarization in tetragonal state of undoped and superconducting single crystals of $Ba(Fe,Co)_2As_2$. The anisotropy is absent at room temperature and in the overdoped Ba-122 sample and therefore it is intrinsic to our samples and not an experimental artifact. We associate the twofold symmetry breaking with electronic nematic fluctuations or ordering of Fe d orbitals. A similar symmetry breaking was observed in F doped Sm-1111 by high-resolution synchrothron powder diffraction, suggesting that the presence of nematic fluctuations is a general property of electron doped FeAs planes [39,148].

Fluence dependence measurements in $YBa_2Cu_3O_{7-\delta}$ single crystals have also shown a saturation of the SC component. By comparing the values of the optically determined

destruction energy U_d and condensation energy U_c^{exp}, determined from specific-heat measurements, we find a significant difference between U_d and U_c^{exp}. A systematic increase of U_d with T_c in the form of power-law dependence observed in the cuprates and pnictides was described in the framework of a model based on Rothwarf-Taylor quasiparticle bottleneck mechanism.

With introducing a new write-pump-probe technique, we were able to monitor the temporal recovery of $1\,T$-TaS_2 after a 50 fs single pulse quench. For the first time, a switching to a new photoinduced p-TaS_2 state (ON state) which has never been reported before, has been achieved. Returning back (OFF state) to the CCDW state is possible by an illumination with a train of 10^4 50 ps long pulses. Switching ON/OFF is accompanied with a change in the reflectivity and DC resistance. Up to date, the highest working base temperature is 68 K, however future experiments on doping/pinning of $1\,T$-TaS_2 or similar CDW systems might reveal the possibility that very soon we will have a new suitable CDW materials for a industrial production of ultrafast memory elements.

7 Acknowledgements

In the spirit of Alfred Painter's thought: "Saying thank you is more than good manners. It is good spirituality.", let me start with acknowledgments to all who have contributed in many different ways to the creation of my doctoral dissertation.
Firstly, I would like to thank my co-supervisor and head of our group Prof. Dr. Dragan D. Mihailović for accepting me as a part of his successful research team from the first time when I knocked on his door, and providing me with this once in a lifetime opportunity. I am thankful for all his superb ideas, comments and advices which have guided my work and vastly improved the quality of my research.
Secondly, I know that being a supervisor is not an easy job and therefore I am thankful to my supervisor Asst. Prof. Tomaž Mertelj for introducing me to experimental work and for all his careful and patient guidance, numerous useful advice and always being there: either for consultation, to answer my numerous questions or provide useful suggestions. I would also like to thank the members of the PhD committee for carefully reading my doctoral thesis and providing helpful comments and constructive criticism. I wish to acknowledge the Slovenian Research Agency and Young Researcher grant No. PR-02601 for the financial support of my PhD research.
Great thanks go to my office roommates: Jure Strle, Martin Strojnik, Jože Buh, Anna Pogrebna, Peter Topolovšek and Andrej Kovič for many different advice and suggestions and for making sure I have a nice time during my PhD studies in general. I would also like to thank my friends and colleagues: Daniela Stojanova, Violeta Mirčevska, Boštjan Berčič, Damjan Vengust, Petra Šutar, Damjan Svetin and Aljaž Drnovšek for all the beautiful moments spent at the work place and outside.
A warm thank you goes to my parents-in-law Jelena and Ljubiša Malbašić for all their love, support and beautiful moments filled with laughter during my PhD studies, especially in the moments during the creation of my doctoral dissertation.
Special mention goes to my husband Uroš, who has always stood by me, encouraged me, loved me and made sure I get a healthy daily dose of optimism that everything will fall in place eventually (as it did).
And finally, I have to give special thanks to my parents Rada and Branislav and my sister Maja for always giving me their endless support and love, especially during my darkest hours. This thesis is a small token of my appreciation and love for them and a way of saying: "Бескрајно сум ви благодарна за вашата несебична подршка!"

8 References

[1] Onnes, H. K. The resistance of pure mercury at helium temperatures. *Comm. Leiden* **28**, 1274–1276 (1911).

[2] Bardeen, J.; Cooper, L. N.; Schrieffer, J. R. Theory of superconductivity. *Phys. Rev.* **108**, 1175 (1957).

[3] Bednorz, J. G.; Mueller, K. A. Possible high T_c superconductivity in Ba-La-Cu-O system. *Zeitschrift für Physik B* **64**, 189 (1986).

[4] Wu, M. K. et al. Superconductivity at 93 K in a New Mixed-Phase Y-Ba-Cu-O Compound System at Ambient Pressure. *Phys. Rev. lett.* **58**, 908 (1987).

[5] Maeda, H.; Tanaka, Y.; Fukutumi, M.; Asano, T. A New Nigh T_c Oxide Superconductor without a Rare Earth Element. *J. Appl. Phys.* **27**, 209 (1988).

[6] Gao, L. et al. Superconductivity up to 164 K in $HgBa_2Ca_{m-1}Cu_mO_{2m+2+\delta}$ (m = 1, 2, and 3) under quasihydrostatic pressures. *Phys. Rev. B* **50**, 4260 (1994).

[7] Kamihara, Y. et al. Iron-Based Layered Superconductor: LaOFeP. *Journal of American Chemical Society* **128**, 10012 (2006).

[8] Gruener, G. The dynamics of charge-density waves. *Rev. Mod. Phys.* **60**, 1129 (1988).

[9] Sie, C. H. *Memory devices using bistable resistivity in amorphous As-Te-Ge films* (PhD Dissertation, Iowa State University, 1969).

[10] Sie, C. H. et al. Chalcogenide glass bistable resistivity memory. *IEEE* **6**, 592 (1970).

[11] Sie, C. H. Electric-field induced filament formation in As-Te-Ge semiconductor. *Journal of Non-Crystalline Solids* **2**, 358 (1970).

[12] Gadermaier, C. et al. Electron-Phonon Coupling in High-Temperature Cuprate Superconductors Determined from Electron Relaxation Rates. *Phys. Rev. Lett.* **105**, 257001 (2010).

[13] Kusar, P. et al. Controlled Vaporization of the Superconducting Condensate in Cuprate Superconductors by Femtosecond Photoexcitation. *Phys. Rev. lett.* **101**, 227001 (2008).

[14] Kabanov, V. V.; Demsar, J.; Podobnik, B.; Mihailovic, D. Quasiparticle relaxation dynamics in superconductors with different gap structures: Theory and experiments on $YBa_2Cu_3O_{7-\delta}$. *Phys. Rev. B* **59**, 1497 (1999).

[15] Mertelj, T. el al. Distinct Pseudogap and Quasiparticle Relaxation Dynamics in the Superconducting State of Nearly Optimally Doped $SmFeAsO_{0.8}F_{0.2}$ Single Crystals. *Phys. Rev. Lett.* **102**, 117002 (2009).

[16] Mertelj, T. et al. Fine Structure in the Electronic Density of States near the Fermi Energy of Al-Ni-Co Decagonal Quasicrystal from Ultrafast Time-Resolved Optical Reflectivity. *Phys. Rev. Lett.* **102**, 086405 (2009).

[17] Demsar, J. et al. Hot electron relaxation in the heavy-fermion $Yb_{1-x}Lu_xAl_3$ compound using femtosecond optical pump-probe spectroscopy. *Phys. Rev. B* **80**, 085121 (2009).

[18] Dvorsek, D. et al. Femtosecond quasiparticle relaxation dynamics and probe polarization anisotropy in $YSr_xBa_{2-x}Cu_4O_8$ ($x = 0$, 0.4). *Phys. Rev. B* **66**, 020510 (2002).

[19] Coslovich, G. et al. Inducing a superconducting-to-normal-state first-order phase transition in overdoped $Bi_2Sr_2Ca_{0.92}Y_{0.08}Cu_2O_{8+\delta}$ by ultrashort laser pulses. Unpublished data.

[20] Toda, Y. et al. Quasiparticle relaxation dynamics in underdoped $Bi_2Sr_2CaCu_2O_{8+\delta}$ by two-color pump-probe spectroscopy. *Phys. Rev. B* **84**, 174516 (2011).

[21] Cortes, R. et al. Momentum-Resolved Ultrafast Electron Dynamics in Superconducting $Bi_2Sr_2CaCu_2O_{8+\delta}$. *Phys. Rev. Lett.* **107**, 097002 (2011).

[22] Demsar, J.; Podobnik, B.; Kabanov, V. V.; Wolf, T.; Mihailovic, D. Superconducting Gap Δ_c, the Pseudogap Δ_p, and Pair Fluctuations above T_c in Overdoped $Y_{1-x}Ca_xBa_2Cu_3O_{7-\delta}$ from Femtosecond Time-Domain Spectroscopy. *Phys. Rev. Lett.* **59**, 1497 (1999).

[23] Demsar, J.; Hudej, R.; Karpinski, J.; Kabanov, V. V.; Mihailovic, D. Quasiparticle dynamics and gap structure in $HgBa_2Ca_2Cu_3O_{8+\delta}$ investigated with femtosecond spectroscopy. *Phys. Rev. B* **63**, 054519 (2001).

[24] Kummer, K. et al. Ultrafast quasiparticle dynamics in the heavy-fermion compound $YbRh_2Si_2$. *Phys. Rev. B* **86**, 085139 (2012).

[25] Yusupov, R. et al. Coherent dynamics of macroscopic electronic order through a symmetry breaking transition. *Nature Physics* **6**, 681 (2010).

[26] Tomeljak, A. et al. Dynamics of photoinduced charge-density-wave to metal phase transition in $K_{0.3}MoO_3$. *Phys. Rev. Lett.* **102**, 066404 (2009).

[27] Demsar, J.; Forro, L.; Berger, H.; Mihailovic, D. Femtosecond snapshots of gap-forming charge-density-wave correlations in quasi-two-dimensional dichalcogenides $1T$-TaS_2 and $2H$-$TaSe_2$. *Phys. Rev. B* **66**, 041101 (2002).

[28] Schmitt, F. et al. Ultrafast electron dynamics in the charge density wave material $TbTe_3$. *New J. Phys.* **13**, 063022 (2011).

[29] Warren, W. W. et al. Cu spin dynamics and superconducting precursor effects in planes above T_c in $YBa_2Cu_3O_{6.7}$. *Phys. Rev. Lett.* **62**, 1193 (1989).

[30] Batlogg, B. et al. Normal State Phase Diagram of $(La,Sr)_2CuO_2$ from Charge to Spin Dynamics. *Physica C* **235**, 130 (1994).

[31] Timusk, T.; Statt, B. The pseudogap in high-temperature superconductors: an experimental survey. *Rep. Prog. Phys.* **62**, 61 (1999).

[32] Tranquada, J. M.; Sternlieb, B. J.; Axe, J. D.; Nakamura, Y.; Uchida, S. Evidence for stripe correlations of spins and holes in copper oxide superconductors. *Nature* **373**, 561 (1995).

[33] Paglione, J.; Greene, R. L. High-temperature superconductivity in iron-based materials. *Nature Physics* **6**, 645 (2010).

[34] Mazin, I. I.; Singh, D. J.; Jonannes, M. D.; Du, M. H. Unconventional Superconductivity with a Sign Reversal in the Order Parameter of $LaFeAsO_{1-x}F_x$. *Phys. Rev. Lett.* **101**, 057003 (2008).

[35] Chubukov, A. V.; Efremov, D. V.; Eremin I. Magnetism, superconductivity, and pairing symmetry in iron-based superconductors. *Phys. Rev. B* **78**, 134512 (2008).

[36] Huang, Q. et al. Neutron-Diffraction Measurements of Magnetic Order and a Structural Transition in the Parent $BaFe_2As_2$ Compound of FeAs-Based High-Temperature Superconductors. *Phys. Rev. Lett.* **101**, 257003 (2008).

[37] de la Cruz, C. et al. Magnetic order close to superconductivity in the iron-based layered $LaO_{1-x}F_xFeAs$ systems. *Nature* **453**, 899 (2008).

[38] Stewart, G. R. Superconductivity in iron compounds. *Rev. Mod. Phys.* **83**, 1589 (2011).

[39] Martinelli, A. et al. Retention of the Tetragonal to Orthorhombic Structural Transition in F-Substituted SmFeAsO: A New Phase Diagram for $SmFeAs(O_{1-x}F_x)$. *Phys. Rev. Lett.* **106**, 227001 (2011).

[40] Sugai, S. Lattice Vibrations in the Charge-Density-Wave States of Layered Transition Metal Dichalcogenides. *Phys. Stat. Sol. B* **129**, 13 (1985).

[41] Fazekaz, P.; Tosatti, E. Electrical, structural and magnetic properties of pure and doped $1T$-TaS_2. *Philosophical Magazine B* **39**, 229 (1979).

[42] Wilson, J. A.; DiSalvo, F. J.; Mahajan, S. Charge-Density Waves and Superlattices in the Metallic Layered Transition Metal Dichalcogenides. *Adv. Phys.* **24**, 117 (1975).

[43] Hughes, H. P.; Pollak, R. A. Charge density waves in layered metals observed by X-ray photoemission. *Phil. Magazine* **34**, 1025 (1976).

[44] Eichberger, M. et al. Snapshots of cooperative atomic motions in the optical suppression of charge density waves. *Nature* **468**, 799 (2010).

[45] Sipos, B. et al. From Mott state to superconductivity in $1T$-TaS_2. *Nature Materials* **7**, 960 (2008).

[46] Lieth, R. M. A. ed. *Physics and Chemistry of Materials with Layered Structures. Vol. I: Preparation and Crystal Growth of Materials with Layered Structures.* (D. Reidel Pub. Co., Boston, 1977).

[47] Averitt, R. Dynamics of broken symmetry. *Nature Physics* **6**, 639 (2010).

[48] Ashcroft, N. W.; Mermin N. D. *Solid State Physics* (Holt, Rinehart and Winston, New York, 1979).

[49] Tanda, S.; Sambongi, T.; Tani, T.; Tanaka, S. X-ray study of charge density wave structure in $1T$-TaS_2. *Jour. of Phys. Soc. of Jpn.* **53**, 476 (1984).

[50] Duffey, J. R.; Kirby, R. D. Raman investigation of the charge-density wave mixed-crystal system $1T$-$TaS_{2-x}Se_x$. *J. Phys. Rev. B* **23**, 1534 (1981).

[51] Karecki, D. R.; Clayman, B. P. Far-infrared reflection spectra of $1T$-TaS_2 and $1T$-$TaSe_2$ in commensurate and incommensurate charge-density wave states. *Phys. Rev. B* **19**, 6367 (1979).

[52] Kennedy, R.J.; Clayman, B. P. Far-infrared studies of commensurate charge-density wave state of 1T-TaS_2. *Phys. Rev. B* **29**, 851 (1984).

[53] London, F.; London, H. The electromagnetic equations of the supraconductor. *Proc. Roy. Soc.* **71** (1935).

[54] Ginzburg, V. L.; Landau, L. D. *Zh. Eksp. Teor. Fiz.* **20**, 1064 (1950).

[55] Schmidt V. V. The physics of superconductors, Introduction to fundamentals and application. (Springer, Berlin, 1997).

[56] Fossheim K.; Sudbo A. Superconductivity: Physics and Application. (Wiley, UK, 2004).

[57] Rothwarf, A.; Taylor, B. N. Measurement of Recombination Lifetimes in Superconductors. *Phys. Rev. lett.* **19**, 27 (1967).

[58] Kabanov, V. V.; Demsar, J.; Mihailovic, D. Kinetics of a Superconductor Excited with a Femtosecond Optical Pulse. *Phys. Rev. Lett.* **95**, 147002 (2005).

[59] Dressel, M.; Gruener, G. *Electrodynamics of Solids* (Cambridge University Press, 2003).

[60] Stevens, C. J. et al. Evidence for Two-Component High-Temperature Superconductivity in the Femtosecond Optical Response of $YBa_2Cu_3O_{7-\delta}$. *Phys. Rev. Lett.* **78**, 2212 (1997).

[61] Han, S. G.; Vardeny, Z. V.; Wong, K. S.; Symko, O. G.; Koren, G. Femtosecond optical detection of quasiparticle dynamics in high-T_c $YBa_2Cu_3O_{7-\delta}$ superconducting thin films. *Phys. Rev. Lett.* **65**, 2708 (1990).

[62] Mihailovic, D.; Podobnik, B.; Demsar, J.; Wagner, G.; Evetts, J. Divergence of the Quasiparticle lifetime with doping and evidence for pre-formed pairs below T* in $YBa_2Cu_3O_{7-\delta}$:direct measurements by femtosecond time-resolved spectroscopy. *J. Phys. Chem. Solids* **59**, 1937 (1998).

[63] Groeneveld, R.; Sprik, R.; Lagendijk, A. Femtosecond spectroscopy of electron-electron and electron-phonon energy relaxation in Ag and Au. *Phys. Rev. B* **51**, 11433 (1995).

[64] Kaganov, M. I.; Lifshits, I. M.; Tanatarov, L. B. *Zh. Eksp. Teor. Fiz.* **31**, 232 (1956).

[65] Kabanov, V. V.; Alexandrov, A. S. Electron relaxation in metals: Theory and exact analytical solutions. *Phys. Rev. B* **78**, 174514 (2008).

[66] Allen, P. B. Theory of Thermal Relaxation of Electrons in Metals. *Phys. Rev. lett.* **59**, 1460 (1987).

[67] van der Marel, D.; Leggett, A. J.; Loram, J. W.; Kirtley, J. R. Condensation energy and high-T_c superconductivity. *Phys. Rev. B* **66**, 140501 (2002).

[68] Loram, J. W.; Luo, J.; Cooper, J. R.; Liang, W. Y.; Tallon, J. L. Evidence on the pseudogap and condensate from the electronic specific heat. *J. Phys. Chem. Solids* **62**, 59 (2001).

[69] Lortz, R. et al. Evolution of the specific-heat anomaly of the high-temperature superconductor $YBa_2Cu_3O_7$ under the influence of doping through application of pressure up to 10 GPa. *J. Phys. Condens. Matter* **17**, 4135 (2005).

[70] Chakravarty, S.; Kee, H. Y.; Abrahamas, E. Frustrated Kinetic Energy, the Optical Sum Rule, and the Mechanism of Superconductivity. *Phys. Rev. Lett.* **82**, 2366 (1999).

[71] Homes, C. C.; Dordevic, S. V.; Bonn, D. A.; Liang, R.; Hardy, W. N. Sum rules and energy scales in the high-temperature superconductor $YBa_2Cu_3O_{6+x}$. *Phys. Rev. B* **69**, 024514 (2004).

[72] Stojchevska, L. et al. Mechanisms of nonthermal destruction of the superconducting state and melting of the charge-density-wave state by femtosecond laser pulses. *Phys. Rev. B* **84**, 180507 (2011).

[73] Boris, A. V. et al. Signatures of Electronic Correlations in Optical Properties of $LaFeAsO_{1-x}F_x$. *Phys. Rev. Lett.* **102**, 027001 (2009).

[74] Thomas, T. N. et al. Photoexcited carrier relaxation and localization in $Bi_2Sr_2Ca_{1-y}Y_yCu_2O_8$ and $YBa_2Cu_3O_{7-\delta}$: A study by femtosecond time-resolved spectroscopy. *Phys. Rev. B* **53**, 12436 (1996).

[75] Bechtel, J. H. Heating of solid targets with laser pulses. *J. App;. Phys.* **46**, 1585 (1975).

[76] Carlslaw, H. S.; Jaeger, J. C. Conduction of heat in Solids. (Oxford University Press, Oxford, 1985).

[77] Mertelj, T. *Influence of doping on optical phonons in high temperature superconductors.* (PhD Thesis, University of Ljubljana, 1996).

[78] Demsar, J. *Photoexcited Carrier Relaxation in High Temperature Superconductors probed by Ultrafast Optical Spectroscopy.* (PhD Thesis, University of Ljubljana, 1999).

[79] Hazen, R. M. Crystal Structures of High-Temperature Superconductors. *Physical Properties of High-Temperature Superconductors* Ed. D. M. Ginsberg, Vol. II, p. 121, (World Scientific, New York, 1990).

[80] Yao X.; Mizukoshi T.; Egami M.; Shiohara Y. Superconductivity and crystal growth of YBCO grown under 1 atm oxygen pressure. *Physica C* **263**, 197 (1996).

[81] Liang, R.; Bonn, D. A.; Hargy, W. N. Evaluation of CuO_2 plane hole doping in $YBa_2Cu_3O_{6+x}$ single crystals. *Phys. Rev. B* **73**, 180505 (2006).

[82] Zhigadlo, N. et al. Single crystals of superconducting $SmFeAsO_{1-x}F_y$ grown at high pressure. *J. Phys. Cond. Matt.* **20**, 342202 (2008).

[83] Chu, J. H. et al. In-Plane Resistivity Anisotropy in an Underdoped Iron Arsenide Superconductor. *Science* **329**, 824 (2010).

[84] Dusza, A. et al. Anisotropic charge dynamics in detwinned $Ba(Fe_{1-x}Co_x)_2As_2$. *Europhys. Lett.* **93**, 37002 (2011).

[85] Chu, J. H.; Analytis, J. G.; Kucharczyk, C.; Fisher, I. R. Determination of the phase diagram of the electron-doped superconductor $Ba(Fe_{1-x}Co_x)_2As_2$. *Phys. Rev. B* **79**, 014506 (2009).

[86] Li, L. J. et al. Superconductivity induced by Ni doping in $BaFe_2As_2$ single crystals. *New J. Phys.* **11**, 025008 (2009).

[87] Zewail, A. H. Photochemistry and Photobiology. (Harwood, London, 1983).

[88] Ling, H.; Wilson, H. Laser Spectroscopy and Photochemistry on Metal Surfaces. (World Scientific, Singapore, 1995).

[89] Tearney, G. J. et al. Scanning single-mode fiber optic catheter-endoscope for optical coherence tomography. *Opt. Lett.* **21**, 1408 (1996).

[90] Gayen, S. K.; Zevallos, M. E.; Alrubaiee, M.; Evans, J. M; Alfano, R. R. Two-Dimensional Near-Infrared Transillumination Imaging of Biomedical Media with a Chromium-Doped Forsterite Laser. *Appl. Opt.* **37**, 5327 (1998).

[91] Nakashima, N.; Shimizu, S.; Yatsuhashi, T.; Sakabe, S.; Izawa, Y. J. Large molecules in high-intensity laser fields. *J. Photochem. Photobiol. C* **1**, 131 (2000).

[92] Juhasz, T. et al. Corneal refractive surgery with femtosecond lasers. *IEEE J. SEl. Top. Qunatum Electron* **5**, 902 (1999).

[93] Lenzner, M. et al. Femtosecond Optical Breakdown in Dielectrics. *Phys. Rev. Lett.* **80**, 4076 (1998).

[94] Operator's Manual Mira 900 (Coherent Inc., Santa Clara, 1997).

[95] see for example:

- Diels, J-C.; Rudolph, W. Ultrashort Laser Pulse Phenomena. (Academic Press, Inc. USA, 1996).
- French, P. M. W. The generation of ultrashort laser pulses. *Rep.Prog.Phys.* **58**, 169 (1995).
- Squier, J.; Salin, F.; Mourou, G.; Harter, D. 100-fs pulse generation and amplification in Ti:Al_2O_3. *Opt.Lett.* **16**, 324 (1991), etc.

[96] Operator's Manual RegA 9050 (Coherent Inc., Santa Clara, 1997).

[97] Singh, D. J.; Du, M. H. Density Functional Study of $LaFeAsO_{1-x}F_x$: A Low Carrier Density Superconductor Near Itinerant Magnetism. *Phys. Rev. Lett.* **100**, 237003 (2008).

[98] Coldea, A. I. et al. Fermi Surface of Superconducting LaFePO Determined from Quantum Oscillations. *Phys. Rev. Lett.* **101**, 216402 (2008).

[99] Ichida, K.; Nakai, Y.; Hosono, H. To What Extent Iron-Pnictide New Superconductors Have Been Clarified: A Progress Report. *J. Phys. Soc. Jpn.* **78**, 062001 (2009).

[100] Hu, W. Z. et al. Origin of the Spin Density Wave Instability in AFe_2As_2 (A = Ba, Sr) as Revealed by Optical Spectroscopy. *Phys. Rev. lett.* **101**, 257005 (2008).

[101] Ahilan, K. et al. ^{19}F NMR investigation of the iron pnictide superconductor $LaFeAsO_{0.89}F_{0.11}$. *Phys. Rev. B* **78**, 100501 (2008).

[102] Nakai, Y. et al. An NMR study on the F-doping evolution of the iron oxypnictide $LaFeAs(O_{1-x}F_x)$. *New J. Phys.* **11**, 045004 (2009).

[103] Gonnelli, R. et al. Point-contact Andreev-reflection spectroscopy in $ReFeAsO_{1-x}F_x$ (Re = La, Sm): Possible evidence for two nodeless gaps. *Physica C* **469**, 512 (2009).

[104] Hadjiev, V. G.; Iliev, M. N.; Sasmal, K.; Sun, Y. Y.; Chu, C. W. Raman spectroscopy of RFeAsO (R = Sm, La). *Phys. Rev. B* **77**, 220505 (2008).

[105] Klauss, H. H. et al. Commensurate Spin Density Wave in LaFeAsO: A Local Probe Study. *Phys. Rev. Lett.* **101**, 077005 (2008).

[106] Drew, A. et al. Coexistence of static magnetism and superconductivity in $SmFeAsO_{1-x}F_x$ as revealed by muon spin rotation. *Nature Materials* **8**, 310 (2009).

[107] Margadonna, S. et al. Crystal structure and phase transitions across the metal-superconductor boundary in the $SmFeAsO_{1-x}F_x$ ($0 \leq x \leq 0.20$) family. *Phys. Rev. B* **79**, 014503 (2009).

[108] Sanna, S. et al. Magnetic-superconducting phase boundary of $SmFeAsO_{1-x}F_x$ studied via muon spin rotation: Unified behavior in a pnictide family. *Phys. Rev. B* **80**, 052503 (2009).

[109] Chia, E. E. M. et al. Quasiparticle relaxation across the spin-density-wave gap in the itinerant antiferromagnet $UNiGa_5$. *Phys. Rev. B* **74**, 140409 (2006).

[110] Chen, Z.; Yuan, R.; Dong, T.; Wang, N. Optical spectroscopy of single-crystalline LaFeAsO. *Phys. Rev. Lett.* **101**, 257005 (2008).

[111] Luo, H. et al. Growth and characterization of $A_{1-x}K_xFe_2As_2$ (A = Ba, Sr) single crystals with x = 0–0.4. *Supercond. Sci. Technol.* **21**, 125014 (2008).

[112] Osborn, R.; Rosenkranz, S.; Goremychkin, E.; Christianson, A. Inelastic neutron scattering studies of the spin and lattice dynamics in iron arsenide compounds. *Physica C* **469** 498 (2009).

[113] Mertelj, T. et al. Photoinduced Quasiparticle Relaxation Dynamics in Near-optimally Doped $SmFeAsO_{0.8}F_{0.2}$ Single Crystals. *J. Supercond. Novel Magn.* **22**, 575 (2009).

[114] Mihailovic, D.; Demsar, J. *Spectroscopy of Superconducting Materials* ACS Symposium Series **730**, 230–244 (American Chemical Society, Washington, DC, 1999).

[115] Mattis, D. C.; Bardeen, J. Theory of the Anomalous Skin Effect in Normal and Superconducting Metals. *Phys. Rev.* **111**, 412 (1985).

[116] Karpinski, J. et al. Single crystals of $LnFeAsO_{1-x}F_x$ (Ln = La, Pr, Nd, Sm, Gd) and $Ba_{1-x}Rb_xFe_2As_2$: Growth, structure and superconducting properties. *Physica C* **469**, 370 (2009).

[117] Tropeano, M. et al. Thermal properties of $SmFeAsO_{1-x}F_x$ as a probe of the interplay between electrons and phonons. *Phys. Rev. B* **78**, 094518 (2008).

[118] Ding, L. et al. Specific heat of the iron-based high-T_c superconductor $SmO_{1-x}F_xFeAs$. *Phys. Rev. B* **77**, 180510 (2008).

[119] Gorkov, L. *J. Supercond.* **14**, 365 (2001).

[120] Park, J. T. et al. Electronic Phase Separation in the Slightly Underdoped Iron Pnictide Superconductor $Ba_{1-x}K_xFe_2As_2$. *Phys. Rev. Lett.* **102**, 117006 (2009).

[121] Laplace, Y.; Bobroff, J.; Ruller-Albenque, F.; Colson, D.; Forget, A. Atomic coexistence of superconductivity and incommensurate magnetic order in the pnictide $Ba(Fe_{1-x}Co_x)_2As_2$. *Phys. Rev. B* **80**, 140501 (2009).

[122] Cimberle, M. R. et al. Magnetic characterization of undoped and 15 % F-doped LaFeAsO and SmFeAsO compounds. *J. Magn. Magn. Mater.* **321**, 3024 (2009).

[123] Baker, P. et al. Heat capacity measurements on FeAs-based compounds: a thermodynamic probe of electronic and magnetic states *New J. Phys.* **11**, 025010 (2009).

[124] Mertelj, T. et al. Quasiparticle relaxation dynamics in spin-density-wave and superconducting $SmFeAsO_{1-x}F_x$ single crystals. *Phys. Rev. B* **81**, 224504 (2010).

[125] Mittal, R. et al. Phonon dynamics in $SrFe_2As_2$ and SrFeAsF parent pnictide compounds: How different/similar when compared to Ca- and Ba-compounds. Unpublished data.

[126] Boeri, L.; Dolgov, O. V.; Golubov, A. A. Is $LaFeAsO_{1-x}F_x$ an Electron-Phonon Superconductor? *Phys. Rev. Lett.* **101** 026403 (2008).

[127] Chen, G. F. et al. Transport and anisotropy in single-crystalline $SrFe_2As_2$ and $A_{0.6}K_{0.4}Fe_2As_2$ (A = Sr, Ba) superconductors. *Phys. Rev. B* **78**, 224512 (2008).

[128] Retting, L. et al. Ultrafast Momentum-Dependent Response of Electrons in Antiferromagnetic $EuFe_2As_2$ Driven by Optical Excitation. *Phys. Rev. Lett.* **108**, 097002 (2012).

[129] Avigo, I. et al. Coherent excitations and electron-phonon coupling in $Ba/EuFe_2As_2$ compounds investigated by femtosecond time- and angle-resolved photoemission spectroscopy. *J. Phys.: Condens. Matter* **25**, 094003 (2013).

[130] Tanatar, M. A. et al. Pseudogap and its critical point in the heavily doped $Ba(Fe_{1-x}Co_x)_2As_2$ from c-axis resistivity measurements. *Phys. Rev. B* **82**, 134528 (2010).

[131] Yi, M. et al. Symmetry-breaking orbital anisotropy observed for detwinned $Ba(Fe_{1-x}Co_x)_2As_2$ above the spin density wave transition. *Proc. Natl. Acad. Sci USA* **108**, 6878 (2011).

[132] Stojchevska, L. et al. Electron-phonon coupling and the charge gap of spin-density wave iron-pnictide materials from quasiparticle relaxation dynamics. *Phys. Rev. B* **82**, 012505 (2010).

[133] Dong, T. et al. Formation of partial energy gap below the structural phase transition and the rare-earth element-substitution effect on infrared phonons in *Re*FeAsO (*Re* = La, Nd, and Sm) *Phys. Rev. B* **82**, 054522 (2010).

[134] Barisic, N. et al. Electrodynamics of electron-doped iron pnictide superconductors: Normal-state properties. *Phys. Rev. B* **82**, 054518 (2010).

[135] Ning, F. et al. Spin Susceptibility, Phase Diagram, and Quantum Criticality in the Electron-Doped High T_c Superconductor $Ba(Fe_{1-x}Co_x)_2As_2$ *J. Phys. Soc. Jpn.* **78**, 013711 (2009).

[136] Chuang, T. M. et al. Nematic Electronic Structure in the "Parent" State of the Iron-Based Superconductor $Ca(Fe_{1-x}Co_x)_2As_2$. *Science* **327**, 181 (2010).

[137] Chia, E. E. M. et al. Ultrafast Pump-Probe Study of Phase Separation and Competing Orders in the Underdoped $(Ba,K)Fe_2As_2$ Superconductor. *Phys. Rev. Lett.* **104**, 027003 (2010).

[138] Fradkin, E.; Kivelson, S. A.; Lawler, M. J.; Eisenstein, J. P.; Mackenzie, A. P. Nematic Fermi Fluids in Condensed Matter Physics. *Annual Review of Condensed Matter Physics* **1**, 153 (2010).

[139] Lucarelli, A. et al. Charge dynamics of Co-doped $BaFe_2As_2$. *New J. Phys.* **12**, 073036 (2010).

[140] Gadermaier, C. et al. High superconducting critical temperatures depend systematically on the electron-phonon interaction strength. Unpublished data.

[141] Kityk, I. V.; Kolinko, M. I. Photostimulated Phase Transitions in High-T_c Superconductors and the Origin of the Superconductivity. *Physica Status Solidi (b)* **185**, 429 (1994).

[142] Iwai, S. et al. Photoinduced Melting of a Stripe-Type Charge-Order and Metallic Domain Formation in a Layered BEDT-TTF-Based Organic Salt. *Phys. Rev. Lett.* **98**, 097402 (2007).

[143] Yu, G.; Heeger A. J. Photoinduced Charge Carriers in Insulating Cuprates: Fermi Glass Insulator, Metal-Insulator Transition and, Superconductivity. *Int. J. Mod. Phys. B* **7**, 3751 (1993).

[144] Geibel, C.; Rietschel, H.; Junod, A.; Pelizzone, M.; Mueller, J. Electronic properties, phonon densities of states and superconductivity in $Nb_{1-x}V_xN$. *J. Phys. F* **15**, 405 (1985).

[145] Kusar, P.; Demsar, J.; Mihailovic, D.; Sugai, S. A systematic study of femtosecond quasiparticle relaxation processes in $La_{2-x}Sr_xCuO_4$. *Phys. Rev. B* **72**, 014544 (2005).

[146] Pashkin, A. et al. Femtosecond Response of Quasiparticles and Phonons in Superconducting $YBa_2Cu_3O_{7-\delta}$ Studied by Wideband Terahertz Spectroscopy. *Phys. Rev. Lett.* **105**, 067001 (2010).

[147] Beyer, M. et al. Photoinduced melting of superconductivity in the high-T_c superconductor $La_{2-x}Sr_xCuO_4$ probed by time-resolved optical and terahertz techniques. *Phys. Rev. B* **83**, 214515 (2011).

[148] Stojchevska, L.; Mertelj, T.; Chu, J. H.; Fisher, I. R.; Mihailovic, D. Doping dependence of femtosecond quasiparticle relaxation dynamics in $Ba(Fe,Co)_2As_2$ single crystals: Evidence for normal-state nematic fluctuations. *Phys. Rev. B* **86**, 024519 (2012).

[149] Renker, B.; Gompf F.; Adelmann P.; Ewert D.; Mutka H. Phonon spectra of HTC superconductors: a comparative inelastic neutron scattering study of the system $(Y_{1-x}Ca_x)(Ba_{2-y}La_y)Cu_3O_{7-\delta}$. *Physica B: Condensed Matter* **165**, 1237 (1990).

[150] Tacon, M.; Krisch, M.; Bosak, A.; Bos, J. W. G.; Margadonna, S. Phonon density of states in $NdFeAsO_{1-x}F_x$. *Phys. Rev. B* **78**, 140505 (2008).

[151] Segre, G. P. et al. Photoinduced Changes of Reflectivity in Single Crystals of $YBa_2Cu_3O_{6.5}$ (Ortho II). *Phys. Rev. lett.* **88**, 137001 (2002).

[152] Vaskivskyi, I. and Svetin, D. Unpublished data.

[153] Stojchevska, L.; Mertelj, T.; Kusar, P.; Vaskivskyi, I.; Svetin, D.; Brazovskii, S.; Mihailovic, D. Ultrafast switching to a hidden topologically protected quantum state in an electronic crystal. Unpublished data.

[154] Beal, A. R.; Hughes, H. P.; Liang, W. Y. The reflectivity spectra of some group VA transition metal dichalcogenides. *J. Phys. C:Solid State Phys.* **8**, 4236 (1975).

[155] Suzuki, A.; Koizumi, M.; Doyama, M. Thermal evidences for successive CDW phase transitions in $1T$-TaS_2. *Solid State Comm.* **53**, 201 (1985).

[156] Uchida, S.; Sugai, S. Infrared and Raman studies on commensurate CDW states in transition metal dichalcogenides. *Physica B+C*, 393 (1981).

[157] Sugai, S.; Murase, K.; Uchida, S.; Tanaka, S. Studies of lattice-dynamics in $2H$-TaS_2 by Raman-Scattering. *Solid State Comm.* **40**, 399 (1981).

[158] Nakashizu, T.; Sekine, T.; Uchinokura, K.; Matsuura, E. Raman study of charge-density-wave phase transitions in $4Hb$-TaS_2. *J. Phys. Soc. Jpn.* **55**, 672 (1986).

[159] Kibble, T. W. Topology of cosmic domains and strings. *J. Phys. A* **9**, 1387 (1976).

[160] Zurek, W. H. Cosmological experiments in superfluid helium? *Nature*, **317**, 505 (1985).

[161] Isa, T. et al. Mid-gap state formed inside Mott gap of $1T$-TaS_2 single crystals and metal-insulator transition. *J. Low Temp. Phys.* **127**, 63 (2002).

[162] Rossnagel, K.; Smith, N. Spin-orbit coupling in the band structure of reconstrutured $1T$-TaS_2. *Phys. Rev. B* **73**, 073106 (2006).

[163] Requardt, H. et al. Direct Observation of Charge Density Wave Current Conversion by Spatially Resolved Synchrotron X-Ray Studies in $NbSe_3$. *Phys. Rev. lett.* **80**, 5613 (1998).

[164] Brazowskii, S. et al. Plastic sliding of charge density waves: X-ray space resolved-studies versus theory of current conversion. *Phys. Rev. B* **61**, 10640 (2000).

[165] Mellor, C. HP and Hynix to produce the memristor goods by 2013. *PCs and Chips*, (The Register, UK, 2011).

[166] de Jong, J. A. et al. Coherent Control of the Route of an Ultrafast Magnetic Phase Transition via Low-Amplitude Spin Precession. *Phys. Rev. Lett.* **108**, 157601 (2012).

[167] Kirilyuk, A.; Kimel, A. V.; Rasing, T. Ultrafast optical manipulation of magnetic order. *Rev. Mod. Phys.* **82**, 2713 (2010).

[168] Rini, M. et al. Photoinduced phase transition in VO_2 nanocrystals: ultrafast control of surface-plasmon resonance. *Optics Lett.* **30**, 558 (2005).

Index of Figures

Figure 1: Schematic structure of $YBa_2Cu_3O_{7-\delta}$ unit cell. 3
Figure 2: Phase diagram for the cuprates. 4
Figure 3: Crystallographic structures of iron-based pnictides. 5
Figure 4: Phase diagram for the iron-based pnictides. 6
Figure 5: Crystal structure of 1 T-TaS_2. 7
Figure 6: Phase transitions of 1 T-TaS_2. 7
Figure 7: A sketch for a periodic charge-density wave ordering. 8
Figure 8: Electron-electron interaction proposed by BCS theory. 12
Figure 9: Elementary excitation spectrum of the superconductor. 12
Figure 10: Energy spectrum of the quasiparticles in the superconductor. 13
Figure 11: Schematic representation of the Rothwarf-Taylor model. 14
Figure 12: Two-temperature model sketch. 17

Figure 13: Susceptibility measurements on annealed YBCO samples. 24
Figure 14: Optical microscope picture of cleaved surface of YBCO. 24
Figure 15: Resistivity and optical measurements on 1 T-TaS_2 single crystals, synthesized by P. Šutar. 25
Figure 16: A schematic of Ti:Sapphire laser oscillator. 26
Figure 17: A schematic of RegA amplifier. 27
Figure 18: A schematic of the pump-probe technique. 28
Figure 19: Determination of the pump and probe beam diameters. 30

Figure 20: Temperature dependence of $\Delta R/R$ transients in undoped SmFeAsO. . . 32
Figure 21: Raw $\Delta R/R$ transients in undoped SmFeAsO taken at selected temperatures. 33
Figure 22: Temperature dependence of the relaxation time and $\Delta R/R$ amplitude in undoped SmFeAsO. 33
Figure 23: Fluence dependence of the relaxation time and $\Delta R/R$ amplitude in undoped SmFeAsO. 34
Figure 24: Temperature dependence of $\Delta R/R$ transients in superconducting $SmFeAsO_{0.8}F_{0.2}$. 36
Figure 25: Fluence dependence of normalized $\Delta R/R$ transients at selected temperatures in the superconducting $SmFeAsO_{0.8}F_{0.2}$ sample. 37
Figure 26: $\Delta R/R$ transients in the superconducting $SmFeAsO_{0.8}F_{0.2}$ taken at selected temperatures. 38
Figure 27: Multicomponent relaxation dynamics in the superconducting $SmFeAsO_{0.8}F_{0.2}$ 38
Figure 28: Temperature dependence of $\Delta R/R$ transients in superconducting $SmFeAsO_{0.8}F_{0.2}$ sample with component A subtracted. 39
Figure 29: Temperature dependence of the superconducting component in $SmFeAsO_{0.8}F_{0.2}$ sample. 40

Figure 30: Temperature dependence of the rise time and relaxation time of the superconducting component in superconducting $SmFeAsO_{0.8}F_{0.2}$. 40
Figure 31: Fluence dependence of the superconducting component in $SmFeAsO_{0.8}F_{0.2}$ sample. 41
Figure 32: Estimation of the magnitude of the superconducting gap. 41
Figure 33: Temperature dependence of the component B relaxation time and $\Delta R/R$ amplitudes in superconducting $SmFeAsO_{0.8}F_{0.2}$. 42
Figure 34: Temperature dependence of the $\Delta R/R$ transients in undoped $SrFe_2As_2$. 44
Figure 35: $\Delta R/R$ reflectivity transients in undoped $SrFe_2As_2$ at selected temperatures. 44
Figure 36: Temperature dependence of the relaxation time and $\Delta R/R$ amplitudes in undoped $SrFe_2As_2$. 45
Figure 37: Optical conductivity spectra on $SrFe_2As_2$. 45
Figure 38: Fluence dependence of the relaxation time and $\Delta R/R$ amplitudes in $SrFe_2As_2$. 46
Figure 39: Fluence dependence of normalized $\Delta R/R$ transients in undoped $SrFe_2As_2$. 46
Figure 40: A schematic of interband scattering in $SrFe_2As_2$. 47
Figure 41: Temperature dependence of $\Delta R/R$ transients in underdoped $Ba(Fe_{1-x}Co_x)_2As_2$. 48
Figure 42: Cleaved surface of Co-5.1% sample analyzed with atomic force microscope. 49
Figure 43: Raw $\Delta R/R$ data for undoped and underdoped $Ba(Fe_{1-x}Co_x)_2As_2$ samples. 49
Figure 44: Temperature dependence of $\Delta R/R$ transients in Co-5 % doped sample. . 50
Figure 45: Multicomponent $\Delta R/R$ relaxation transients in Co-5.1 % doped sample. 50
Figure 46: Multiexponential fits of the relaxation time and corresponding amplitudes in $Ba(Fe_{1-x}Co_x)_2As_2$ samples. 51
Figure 47: Temperature dependence of $\Delta R/R$ amplitudes in undoped and underdoped $Ba(Fe_{1-x}Co_x)_2As_2$ samples. 52
Figure 48: Temperature dependence of $\Delta R/R$ transients in Co-7 % and 11 % doped samples. 53
Figure 49: Saturation of the superconducting component in Co-7 % doped $Ba(Fe_{1-x}Co_x)_2As_2$ sample. 54
Figure 50: Temperature dependence of the superconducting component in Co-5.1 %, 7 % and 11 % doped samples. 55
Figure 51: Response in the normal state in Co-5.1 % sample. 56
Figure 52: Temperature dependence of $\Delta R/R$ amplitudes for Co-5.1 %, 7 % and 11 % doped samples. 57
Figure 53: $\Delta R/R$ transients of Ba-122 samples measured at $T = 300$ K. 58
Figure 54: Reflectivity $\Delta R/R$ transients at $T = 300$ K and the second moment of the Eliashberg function as a function of Co doping 60

Figure 55: Comparison of the $\Delta R/R$ signal at $T < T_c$ and at $T > T_c$ in underdoped $YBa_2Cu_3O_{6.5}$. 64
Figure 56: Fluence dependence of $\Delta R/R$ transients in $YBa_2Cu_3O_{6.5}$. 65
Figure 57: ΔR_{SC} as a function of normalized $\mathscr{F}/\mathscr{F}_T$ for different high-T_c superconductors. 66
Figure 58: Destruction energy U_d as a function of T_c^2 for different high-T_c superconductors. 66

Figure 59: A schematic of a write-pump-probe setup. 72
Figure 60: Raw $\Delta R/R$ transients and coherent phonon mode spectra after quench with W pulses at $T = 30$ K 73
Figure 61: Switching to a new p-TaS_2 state. 74

Figure 62: Raw $\Delta R/R$ transients and coherent phonon mode spectra after quench with a train of W pulses at $T = 68$ K. 74
Figure 63: Coherent phonon mode spectra after quench with a train of W pulses at T =120 and 150 K. 75
Figure 64: Switching fluence threshold as a function of W pulse duration. 76
Figure 65: Switching OFF with a different number of E pulses. 76
Figure 66: $1\,T$-TaS_2 system switching OFF by warming up at $T = 100$ K. 77
Figure 67: $\Delta R/R$ transients and collective mode spectra of $1\,T$-TaS_2 in the ON and OFF state. 78
Figure 68: Collective mode spectra of $1\,T$-TaS_2 in the ON and OFF state after two cycles of photoillumination. 78
Figure 69: The reflectivity of $1\,T$-TaS_2 in the ON and OFF state during a sequence of alternating W and E pulse sequences. 79
Figure 70: Resistivity switching by 50 fs pulses on a 20 nm thick $1\,T$-TaS_2 sample. 79
Figure 71: The electronic and lattice temperature estimated with the two-temperature model. 81
Figure 72: A schematic of the energy diagram for ON-OFF switching into the p-TaS_2 state. 83

Figure 73: Fluence dependence of $\Delta R/R$ transients in $YBa_2Cu_3O_{6.6}$. 109
Figure 74: Fluence dependence of $\Delta R/R$ transients in $YBa_2Cu_3O_{6.8}$. 110
Figure 75: Fluence dependence of $\Delta R/R$ transients in $YBa_2Cu_3O_7$. 111
Figure 76: Raw data on switching fluence threshold as a function of W pulse duration. 112
Figure 77: Fluence dependence data on switching OFF with a single E pulse. . . . 113

Index of Tables

Table 1: Charge gap magnitudes in the Ba-122 samples, exhibiting SDW ordering. 52
Table 2: Characteristic pseudogap magnitudes for SC $Ba(Fe_{1-x}Co_x)_2As_2$ samples. 57
Table 3: Electron-phonon coupling parameters in Ba-122 iron-based superconductors. 60
Table 4: Estimated SDW and PG gap magnitudes and electron-phonon coupling parameters in iron-based superconductors. 62
Table 5: Calculated $U_d/U_c^{\exp}$ ratio for different high-T_c superconductors. 68
Table 6: Raman spectra of R-TaS_2 polytypes ($R = 1T$, $2H$, $4Hb$). 82

Appendix

A Appendix 1

A.1 Original Scientific Articles

1. Mertelj, T.; Stojčevska, L.; Zhigadlo, N. D.; Karpinski, J.; Mihailović, D. Normal state bottleneck and nematic fluctuations from femtosecond quasiparticle relaxation dynamics in Sm(Fe,Co)AsO. *Phys. rev. B* **87**, 174525 (2013).

2. Stojčevska, L.; Mertelj, T.; Chu, J-H.; Fisher, I. R.; Mihailović, D. Dynamics of Photoexcited Carriers in $Ba(Fe_{1-x}Co_x)_2As_2$ Single Crystals with Spin-Density-Wave Ordering. *J. supercond. nov. magn.* [in press]. (2013).

3. Stojčevska, L.; Mertelj, T.; Chu, J-H.; Fisher, I. R.; Mihailović, D. Doping dependence of femtosecond quasiparticle relaxation dynamics in $Ba(Fe,Co)_2As_2$ single crystals: evidence for normal-state nematic fluctuations. *Phys. rev. B* **86**, 024519 (2012).

4. Mertelj, T.; Kušar, P; Stojčevska, L.; Kabanov, V. V.; Zhigadlo, N. D.; Katrych, S.; Karpinski, J.; Mihailović, D. Doping dependent quasiparticle relaxation dynamics in $SmFeAsO_{1-x}F_x$ single crystals : Comparison of spin-density wave and superconducting states. *J. supercond. nov. magn.* **24**, 489 (2011).

5. Stojčevska, L.; Kušar, P.; Mertelj, T.; Kabanov, V. V.; Toda, Y.; Yao, X.; Mihailović, D. Mechanisms of nonthermal destruction of the superconducting state and melting of the charge-density-wave state by femtosecond laser pulses. *Phys. rev. B* **84**, 180507 (2011).

6. Mertelj, T.; Kušar, P.; Kabanov, V. V.; Stojčevska, L.; Zhigadlo, N. D.; Katrych, S.; Bukowski, Z.; Karpinski, J.; Weyeneth, S.; Mihailović, D. Quasiparticle relaxation dynamics in spin-density-wave and superconducting $SmFeAsO_{1-x}F_x$ single crystals. *Phys. rev. B* **81**, 224504 (2010).

7. Stojčevska, L.; Kušar, P.; Mertelj, T.; Kabanov, V. V.; Lin, X.; Cao, G.; Xu, Z. A.; Mihailović, D. Electron-phonon coupling and the charge gap of spin-density wave iron-pnictide materials from quasiparticle relaxation dynamics. *Phys. rev. B* **82**, 012505 (2010).

A.2 Published Scientific Conference Contributions (Invited lecture)

1. Mihailović, D.; Yusupov, R.; Mertelj, T.; Stojčevska, L.; Vaskivskyi, I.; Brazovskii, S. Coherent trajectories through phase transitions in complex system : detection of coherent and incoherent topological defect dynamics. In: *Abstract and Program Book of SMEC 2013 conference*, 34 (SMEC 2013, Miami, Eastern Caribbean, 2013).

2. Kušar, P.; Madan, I.; Stojěvska, L.; Mertelj, T.; Lu-dac, M.; Kabanov, V. V.; Mihailović, D. Metastability and transient vortices in the femtosecond trajectory of the normal -to- superconducting state transition in cuprate superconductors. In: *Abstract and Program Book of ICSM 2012, 3rd International Conference on Superconductivity and Magnetism*, 1121 (ICSM, Istanbul, Turkey, 2012).

3. Stojčevska, L.; Mertelj, T.; Šutar, P.; Svetin, D.; Mihailović, D. Switching to a hidden many-body state of matter by femtosecond laser pulses. In: *Abstract and Program Book of IMPACT 2012 : electronic states and phases induced by electric or optical impacts*, 58 (IMPACT 2012, Orsay, France, 2012).

4. Stojčevska, L.; Mertelj, T.; Chu, J-H.; Fisher, I. R.; Mihailović, D. Systematic doping dependence study of femtosecond relaxation dynamics in $Ba(Co,Fe)_2As_2$ single crystals. In: *Abstract and Program Book of 55th Course: Phase Separation and Superstripes in High Temperature Superconductors and Related Phenomena*, 136 (Ettore Majorana Foundation and Centre for Scientific Culture, Erice, Italy, 2012).

5. Gadermaier, C.; Kabanov, V. V.; Alexandrov, A. S.; Stojčevska, L.; Mertelj, T.; Mihailović, D. Systematic depencence of the superconducting critical temperature on the electron energy relaxation rate. In: *Abstract and Program Book of 55th Course: Phase Separation and Superstripes in High Temperature Superconductors and Related Phenomena*, 137 (Ettore Majorana Foundation and Centre for Scientific Culture, Erice, Italy, 2012).

A.3 Published Scientific Conference Contributions

1. Vaskivskyi, I.; Mihailović, D.; Mertelj, T.; Stojčevska, L. Light induced resistive switching to a hidden state in $1\,T$-TaS_2. In: *Timetable and book of abstracts : workshop on "Short-time Dynamics in Strongly Correlated Systems and Novel Superconductors"*, 58 (Technische Universität, Dortmund, 2013).

2. Stojčevska, L.; Mertelj, T.; Chu, J-H.; Fisher, I. R.; Mihailović, D. Doping dependence of femtosecond quasi-particle relaxation dynamics in $Ba(Fe,Co)_2As_2$ single : evidence for normal state orthorombic fluctuations. In: *Abstract and Program Book of ICSM 2012, 3rd International Conference on Superconductivity and Magnetism*, 740 (ICSM, Istanbul, Turkey, 2012).

3. Svetin, D.; Mihailović, D.; Stojčevska, L.; Buh, J.; Strojnik, M.; Podobnik, B.; Kavčič, B. Quick fabrication of custom shaped electrodes on insulating substrated nanocrystals and their positioning with ProtolaserD device for laser lithography. In: *Book of Abstracts of SLONANO 2012*, 103 (Jozef Stefan Institute, Ljubljana, 2012).

4. Gadermaier, C.; Kabanov, V. V.; Alexandrov, A. S.; Stojčevska, L.; Mertelj, T.; Manzoni, C.; Cerullo, G.; Mihailović, D. High superconducting critical temperatures depend systematically on the electron-phonon relaxation rate. In: *Book of Abstracts of Nonequilibrium phenomena in complex matter: new observations and new theories*, 18 (Jozef Stefan Institute, Ljubljana, 2012).

5. Stojčevska, L.; Mertelj, T.; Zhigadlo, N. D.; Karpinski, J.; Chu, J-H.; Fisher, I. R.; Mihailović, D. Real time observations of quasi-particle relaxation dynamics in undoped iron-based pnictides by means of femtosecond laser spectroscopy. In: *Book of Abstracts of Nonequilibrium phenomena in complex matter: new observations and new theories*, 38 (Jozef Stefan Institute, Ljubljana, 2012).

6. Vaskivskyi, I.; Mihailović, D.; Mertelj, T.; Stojčevska, L. Light induced switching to a hidden state in thin-film $1\,T$-TaS_2. In: *Book of Abstracts of Nonequilibrium*

phenomena in complex matter: new observations and new theories, 46 (Jozef Stefan Institute, Ljubljana, 2012).

7. Mertelj, T.; Stojčevska, L.; Chu, J-H.; Fisher, I. R.; Mihailović, D. Doping dependence of femtosecond quasi-particle relaxation dynamics in $Ba(Fe,Co)_2As_2$ single crystals : possible evidence for normal state nematic fluctuations. In: *Abstract and Program Book of Physics of Low-dimensional conductors: problems and perspectives: International Conference*, 47 (Institute of Physics, Zagreb, 2012).

8. Mertelj, T.; Stojčevska, L.; Kušar, P.; Gadermaier, C.; Kabanov, V. V.; Mihailović, D.; Chu, J-H.; Fisher, I. R.; Zhigadlo, N. D.; Katrych, S.; Bukowski, Z.; Weyeneth, S.; Karpinski, J. Time resolved femtosecond optical spectroscopy of electron doped 1111 and 122 iron-pnictide superconductors. In: *Abstract Book of the 8th International Conference of the series on Stripes and High T_c Superconductivity, STRIPES 11*, 107 (Superstripes press science series, no. 1, Rome, 2011).

9. Stojčevska, L.; Kušar, P.; Mertelj, T.; Kabanov, V. V.; Lin, X.; Cao, G.; Xu, Z. A.; Mihailović, D. Study of quasiparticle relaxation dynamics in $SrFe_2As_2$ spin-density wave iron-pnictide single crystals. In: *Abstract Book of the 8th International Conference of the series on Stripes and High T_c Superconductivity, STRIPES 11*, 110 (Superstripes press science series, no. 1, Rome, 2011).

10. Stojčevska, L.; Mertelj, T.; Chu, J-H.; Fisher, I. R.; Mihailović, D. Systematic doping dependence study of quasiparticle relaxation dynamics in $Ba(Fe,Co)_2As_2$ single crystals. In: *Book of Abstracts of SLONANO 2011*, 88 (Jozef Stefan Institute, Ljubljana, 2011).

11. Kušar, P.; Mertelj, T.; Stojčevska, L.; Mihailović, D. Light induced evaporation and subsequent condensation of superconducting condensate in cuprates. In: *Abstract and Program Book of ICSM 2010, International Conference on Superconductivity and Magnetism*, 124 (ICSM, Antalya, Turkey, 2010).

12. Mertelj, T.; Kabanov, V. V.; Stojčevska, L.; Zhigadlo, N. D.; Katrych, S.; Karpinski, J.; Mihailović, D. Quasiparticle relaxation dynamics in undoped and near-optimally doped SmFeAsOF single crystals. In: *Abstract and Program Book of ICSM 2010, International Conference on Superconductivity and Magnetism*, 152 (ICSM, Antalya, Turkey, 2010).

13. Stojčevska, L.; Kušar, P.; Mertelj, T.; Kabanov, V. V.; Mihailović, D. Comparison of the optically measured vaporization energy by ultrafast laser spectroscopy and the condensation energy determined from specific heat measurements. In: *Abstract and Program Book of ICSM 2010, International Conference on Superconductivity and Magnetism*, 201 (ICSM, Antalya, Turkey, 2010).

14. Stojčevska, L.; Kušar, P.; Mertelj, T.; Kabanov, V. V.; Zhigadlo, N. D.; Katrych, S.; Karpinski, J.; Mihailović, D. Study of quasiparticle relaxation dynamics in $SmFeAsO_{1-x}F_x$ single crystals. In: *Book of Abstracts of SLONANO 2010*, 89 (Jozef Stefan Institute, Ljubljana, 2010).

15. Stojčevska, L.; Kušar, P.; Mertelj, T.; Kabanov, V. V.; Zhigadlo, N. D.; Katrych, S.; Karpinski, J.; Mihailović, D. Raziskava dinamike kvazidelčne relaksacije v monokristalih $SmFeAsO_{1-x}F_x$. In: *Zbornik povzetkov of 7. konferenca fizikov v osnovnih raziskavah*, 70 (DMFA, Portorož, 2010).

16. Stojčevska, L.; Kušar, P.; Mertelj, T.; Kabanov, V. V.; Mihailović, D. Comparison of the optically measured vaporization energy by ultrafast laser spectroscopy and the

condensation energy determined from specific heat measurements in superconducting cuprates. In: *Zbornik prispekov of 2nd Jozef Stefan International Postgraduate School Students Conference*, 70 (Mednarodna podiplomska šola Jožefa Stefana, Ljubljana, 2010).

17. Stojčevska, L.; Kušar, P.; Mertelj, T.; Mihailović, D. Quasiparticle relaxation dynamics in $YBa_2Cu_3O_{7-d}$ studied by ultrafast time-resolved spectroscopy. In: *Book of Abstracts of SLONANO 2009*, 99 (National Institute of Chemistry, Ljubljana, 2009).

A.4 Monographs

A.4.1 Patent application

1. Stojčevska, L.; Mertelj, T.; Vaskivskyi, I.; Mihailović, D. Ultrafast memory by laser quench : patent application P-201200364. Ljubljana: Urad RS za intelektualno lastnino, (30. dec. 2012).

B Appendix 2

B.1 Destruction of the superconducting state in $YBa_2Cu_3O_{7-\delta}$ superconductor

Here, we present $\mathscr{F}$-dependence measurements for three different $YBa_2Cu_3O_{7-\delta}$ compounds with $T_c s$ =63, 85 and 93 K, respectively.

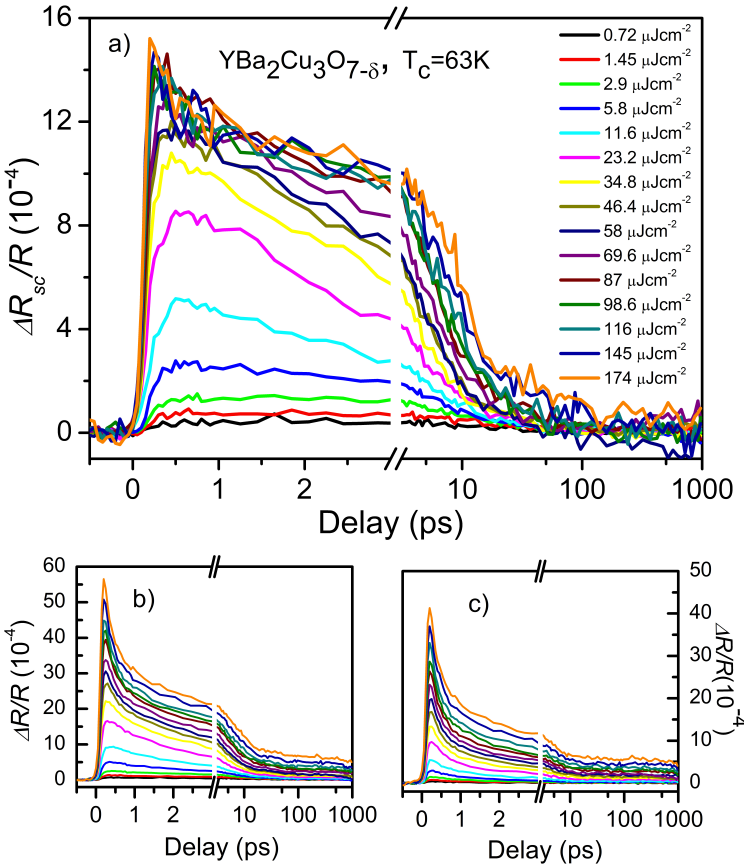


Figure 73: (a) $\Delta R_{sc}/R$ for $YBa_2Cu_3O_{6.6}$ as a function of time delay for different $\mathscr{F}$. The reflectivity $\Delta R/R$ transients at $T = 4$ and 68 K are shown in (b) and (c), respectively.

Reflectivity $\Delta R/R$ transients at $T = 4$ K in $YBa_2Cu_3O_{6.8}$ and $YBa_2Cu_3O_7$ (see Figs. 74 (b) and 75 (b)) show an emergence of a negative picosecond component. With increasing $\mathscr{F}$, the superconducting component quickly saturates while an increasing contribution of the normal state components starts to prevail at shorter timescales resulting in a shift of the saturated superconducting component $\Delta R_{sc}/R$ towards longer delays.

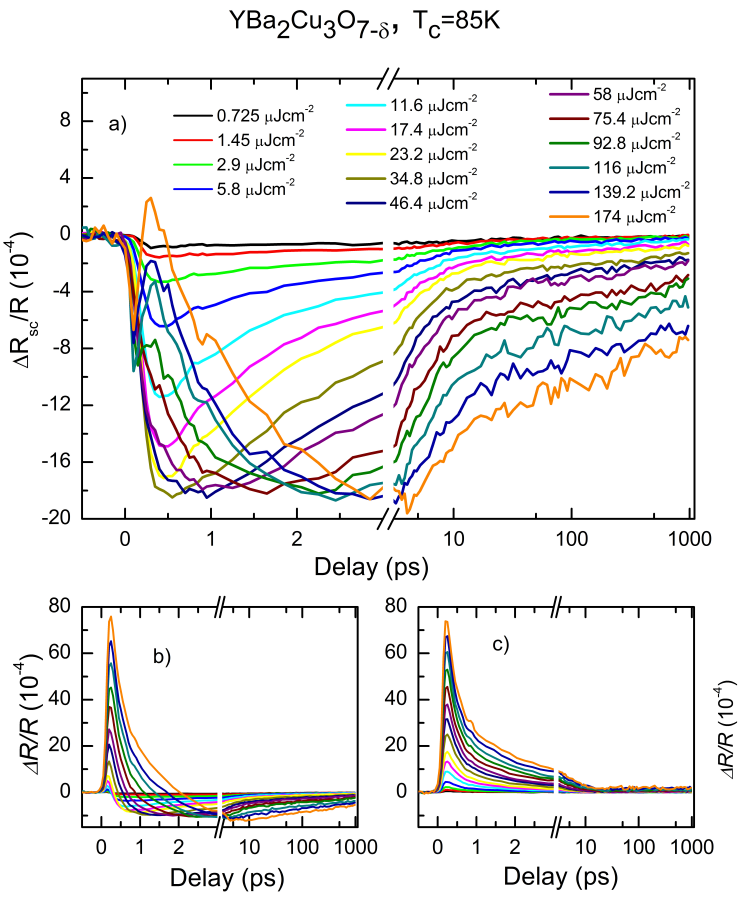


Figure 74: (a) $\Delta R_{sc}/R$ for $YBa_2Cu_3O_{6.8}$ as a function of time delay for different $\mathscr{F}$. The reflectivity $\Delta R/R$ transients at $T = 4$ and 90 K are shown in (b) and (c), respectively.

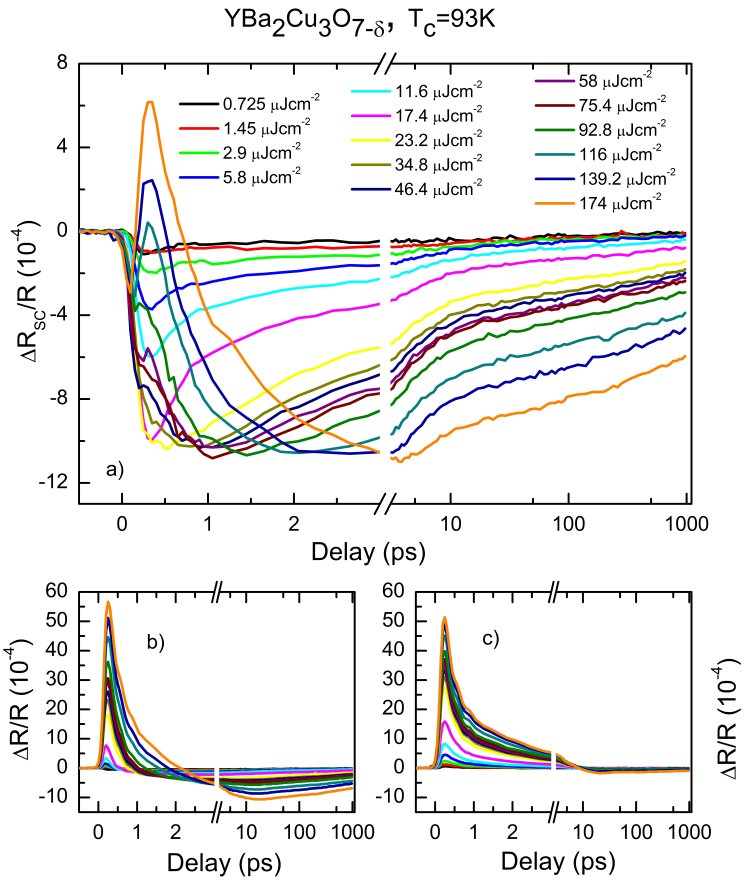


Figure 75: (a) $\Delta R_{sc}/R$ for $YBa_2Cu_3O_7$ as a function of time delay for different $\mathscr{F}$. The reflectivity $\Delta R/R$ transients at $T = 4$ and 100 K are shown in (b) and (c), respectively.

B.2 Switching to a new hidden state in 1*T*-TaS_2

Firstly we present a systematic measurement of the $\mathscr{F}_T$ of the W pulse as a function of the τ_W pulse duration (Fig. 76).

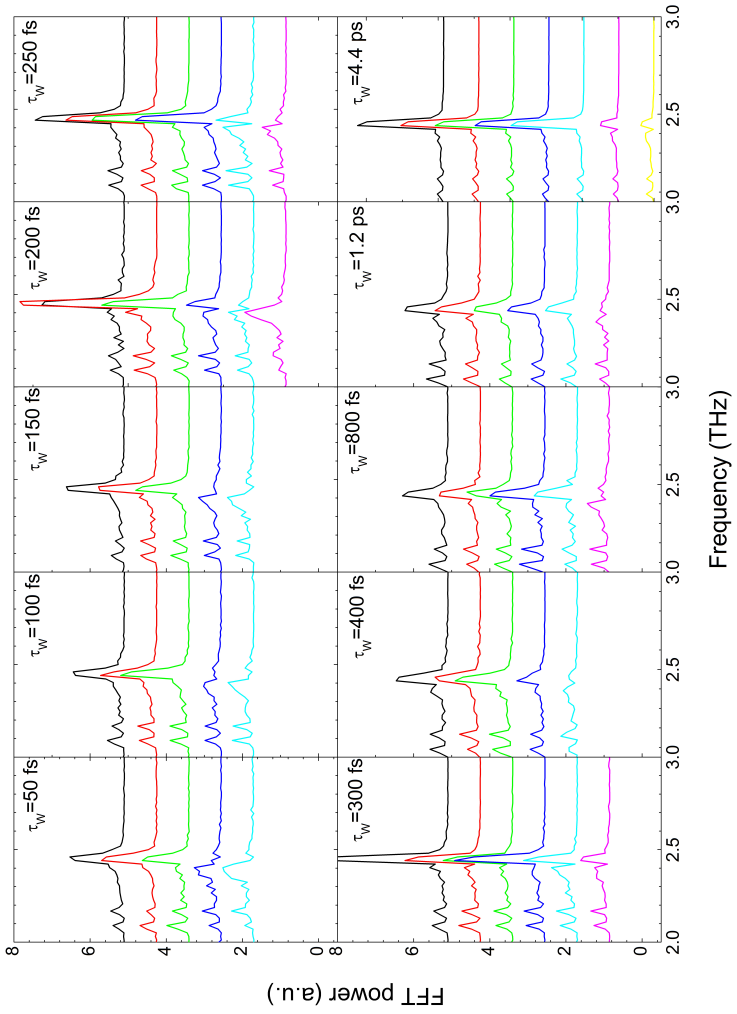


Figure 76: Systematic measurement of the W pulse fluence threshold $\mathscr{F}_W$ (black solid line) as a function of the pulse duration τ_W: 50, 100, 150, 200, 250, 300, 400, 800 ps and 1.2 and 4.4 ps. Colour of the spectra refers to FFT without D pulse (black) and after $\mathscr{F}_W = 470$(red), 705(green), 940(blue), 1175(cyan) and 1410(pink) μJ/cm^2. It was found that a single W pulse at 1 mJ/cm^2 and $\tau_W = 50$ fs is sufficient for switching to the p-TaS_2 state.

Secondly, in Fig. 77 and we show measurements of E pulse threshold to switch OFF as function of fluence $\mathscr{F}_E$.

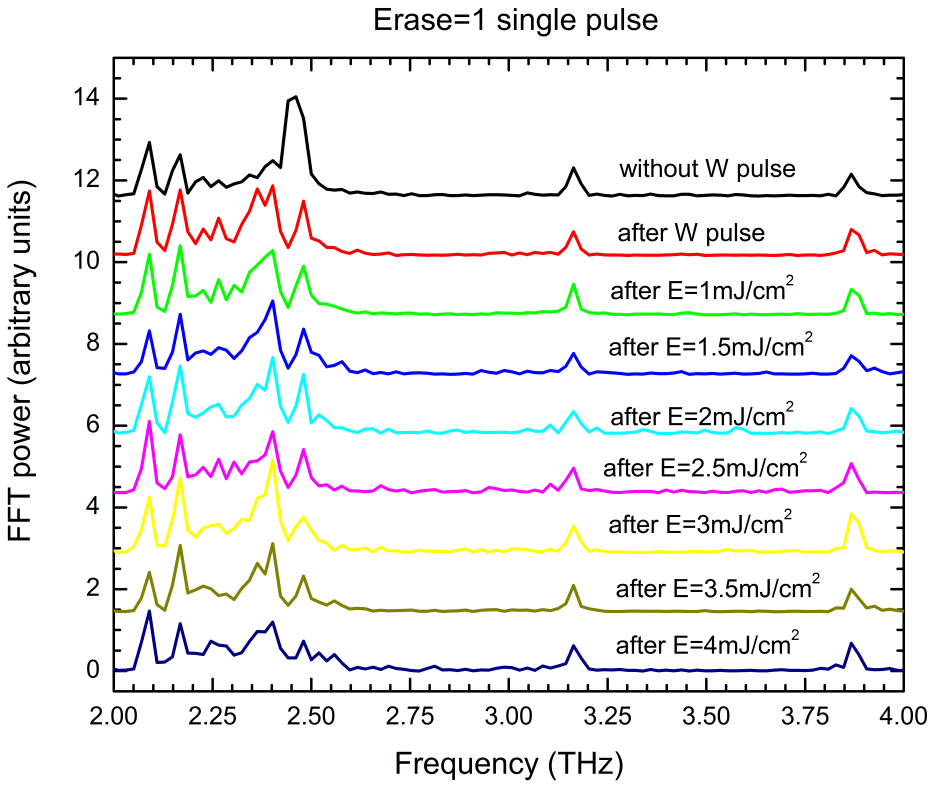


Figure 77: Systematic measurement of the single E pulse fluence threshold $\mathscr{F}_{\mathrm{E}}$ for switching OFF, after photoillumination with a single W pulse (red line). It was found that even at the highest achievable $\mathscr{F}_{\mathrm{E}}$, switching OFF with only one E pulse was not successful.

C Appendix 3

C.1 Maxwell's equations in a vacuum

The interaction of electromagnetic radiation with matter is fully described by Maxwell's equations [59]. In the case of a vacuum the four relevant equations are:

- in SI units:

$$\nabla \cdot \vec{E}(\vec{r},t) = \frac{\rho(\vec{r},t)}{\varepsilon_0} \tag{56}$$

also known as Gauss's law;

$$\nabla \cdot \vec{B}(\vec{r},t) = 0 \tag{57}$$

also known as Gauss's law for magnetism;

$$\nabla \times \vec{E}(\vec{r},t) + \frac{\partial \vec{B}(\vec{r},t)}{\partial t} = 0 \tag{58}$$

also known as Faraday's law of induction;

$$\nabla \times \vec{B}(\vec{r},t) - \mu_0 \varepsilon_0 \frac{\partial \vec{E}(\vec{r},t)}{\partial t} = \mu_0 \vec{J}(\vec{r},t) \tag{59}$$

also known as Ampere's circuital law (with Maxwell's correction).

- in CGS units:

$$\nabla \cdot \vec{E}(\vec{r},t) = 4\pi\rho(\vec{r},t) \tag{60}$$

$$\nabla \cdot \vec{B}(\vec{r},t) = 0 \tag{61}$$

$$\nabla \times \vec{E}(\vec{r},t) + \frac{1}{c}\frac{\partial \vec{B}(\vec{r},t)}{\partial t} = 0 \tag{62}$$

$$\nabla \times \vec{B}(\vec{r},t) - \frac{1}{c}\frac{\partial \vec{E}(\vec{r},t)}{\partial t} = \frac{4\pi}{c}\vec{J}(\vec{r},t) \tag{63}$$

Here $\vec{E}$ and $\vec{B}$ are the electric field strength and the magnetic induction, respectively; c is the velocity of the light in free space; $\vec{J}$ and ρ are the current density and charge density, respectively; μ_0 and ε_0 are magnetic and electric permeability of free space, respectively.

C.2 Maxwell's equations in the presence of matter

- in SI units:

$$\nabla \cdot \vec{D}(\vec{r},t) = \frac{\rho_{ext}(\vec{r},t)}{\varepsilon_0} \tag{64}$$

$$\nabla \cdot \vec{B}(\vec{r},t) = 0 \tag{65}$$

$$\nabla \times \vec{E}(\vec{r},t) + \frac{\partial \vec{B}(\vec{r},t)}{\partial t} = 0 \tag{66}$$

$$\nabla \times \vec{H}(\vec{r},t) - \mu_0 \varepsilon_0 \frac{\partial \vec{D}(\vec{r},t)}{\partial t} = \mu_0 \overrightarrow{J_{cond}}(\vec{r},t) \tag{67}$$

- in CGS units:

$$\nabla \cdot \vec{D}(\vec{r},t) = 4\pi\rho_{ext}(\vec{r},t) \tag{68}$$

$$\nabla \cdot \vec{B}(\vec{r},t) = 0 \tag{69}$$

$$\nabla \times \vec{E}(\vec{r},t) + \frac{1}{c}\frac{\partial \vec{B}(\vec{r},t)}{\partial t} = 0 \tag{70}$$

$$\nabla \times \vec{H}(\vec{r},t) - \frac{1}{c}\frac{\partial \vec{D}(\vec{r},t)}{\partial t} = \frac{4\pi}{c}\overrightarrow{J_{cond}}(\vec{r},t) \tag{71}$$

Here $\overrightarrow{J_{cond}}$ defined with $\overrightarrow{J_{cond}} = \sigma_1 \overrightarrow{E}$ where σ_1 represents the conductivity of the material, arises from the motion of electrons in the presence of an electric field. With ρ_{exp} we denote the external charge added from the outside and $\overrightarrow{H}$ is the magnetic field strength. $\overrightarrow{D}$ is the dielectric displacement defined with $\overrightarrow{D} = \varepsilon_1 \overrightarrow{E}$, where ε_1 is the dielectric constant.